Feasibility of magnetic resonance imaging-based radiation therapy for brain tumour treatment

Tomáš Pavel

School of Science

Thesis submitted for examination for the degree of Master of Science in Technology.

Espoo 31.7.2017

Thesis supervisor:

Prof. Risto Ilmoniemi

Thesis advisor:

Max Köhler PhD

Aalto University
School of Science

AALTO UNIVERSITY
SCHOOL OF SCIENCE

ABSTRACT OF THE
MASTER'S THESIS

Author: Tomáš Pavel

Title: Feasibility of magnetic resonance imaging-based radiation therapy for brain tumour treatment

Date: 31.7.2017 Language: English Number of pages: 8+79

Department of Neuroscience and Biomedical Engineering

Professorship: Biomedical Engineering

Supervisor: Prof. Risto Ilmoniemi

Advisor: Max Köhler PhD

Purpose: The increasing use of MRI alongside CT images has brought about growing interest in trying to determine radiation attenuation information based on MR images only. The primary aim of this thesis is, therefore, to determine what head tissue compartments need to have separate HU values in order to obtain sufficient RT planning accuracy. This can serve as input for an MR-based classification thus enabling pseudo-CT generation in an MR-only RT workflow.
Methods: To achieve this target, flattened (stratified) CT images (fCT) were generated and compared to the original CT images. Mean (ME) and mean absolute (MAE) errors were used for the fCT quality assessment, as was dose comparisons. 70 CT-based RT plans were generated and the dose distributions compared to those obtained when using the different fCT versions in place of the original CT images. The dose agreement was assessed using DVH and 1%/1 mm gamma analysis.
Results: The lowest MAE of 59.63 HU was calculated for an fCT8 version. DVH analysis showed low differences in the range between 3% (water-filled fCT) and 0.05% depending on the tissue stratification of the fCT version. 1%/1 mm gamma analysis correctly identified plans where insufficiently fine-grained tissue classification was the main reason for dose discrepancy. The best RT planning accuracy was obtained for the fCT5 with segmented air cavities, fat, water-rich tissue, spongy, and compact bone, and for the fCT8 where also the brain tissue was stratified.
Conclusions: The small differences in dose accuracy between CT and fCT images shows the feasibility of using MR-only RT planning for the brain. Nonetheless, other aspects of the MR-only workflow, such as patient positioning, as well as the impact of e.g. the surgical incisions in the skull should be subject to further research.

Keywords: radiotherapy, MR-only, brain tumour, CT, MRI, tissue stratification, image segmentation, pseudo-CT, dose comparisons, gamma analysis, DVH analysis, RT planning

Preface

First I wish to thank my advisor Max Köhler for highly appreciated guidance, support, corrections of this thesis and for valuable feedback that was always delivered in empathetic and encouraging form. I am very grateful to Max and all my colleagues at Philips for accepting me as a team member and for giving me an opportunity to follow and work on research and development projects in highly interesting fields such as medical image analysis and radiation therapy. In particular, I would like to thank Matti Lindström for patience and continuous help with making use of the treatment planning system and dose analysis tools that were crucial for performing dose analyses presented in this thesis. I wish to thank Julius Koskela and Aleksi Halkola for providing their valued comments on both, the content and the writing style of this thesis.

I would like to thank sincerely my supervisor Prof. Risto Ilmoniemi for support and always the constructive and fast feedback that helped me to complete this project.

My deepest gratitude goes to my parents Věra and Tomáš for their endless love, encouragement, and support throughout my life and for making my studies in Finland and all other dreams possible.

I am also thankful to my friends here in Finland for support and patience during my studies and in particular during the time when I was working on this project, reminding me that life is not only about the work, research, and thesis writing.

Otaniemi, 31.7.2017

Tomáš Pavel

Contents

Symbols and abbreviations

Symbols

$\mathbf{B_0}$	Main magnetic field
CI	Conformity index
D	Dose
DTA	Distance-to-agreement
HU	Hounsfield unit (CT number)
MAE	Mean absolute error
ME	Mean error
MU	Monitor unit
$\mathbf{T_1}$	Longitudinal relaxation time
$\mathbf{T_2}$	Transverse relaxation time
TE	Echo time
TR	Repetition time
β	Potential in MRF-ICM algorithm
γ	Gamma index
ρ	Proton density

Abbreviations

2D	Two dimensional
3D	Three dimensional
A	Anterior direction or PTV position
CBCT	Cone beam computed tomography
CSF	Cerebrospinal fluid
CNS	Central nervous system
CR	Cerebral PTV position
CT	Computed tomography
CTV	Clinical target volume
DRR	Digitally reconstructed radiograph
DICOM	Format for storing of medical images
DOF	Degree of freedom
fCT	Flattened CT
FDA	Food and drug administration
FOV	Field of view
FID	Free induction decay
FLAIR	Fluid attenuation inversion recovery
GBM	Glioblastoma multiforme
GE	Gradient echo
GM	Grey matter
GMM	Gaussian mixture model
GTV	Gross tumour volume
HD	High-definition
HW	Hardware
ICM	Iterated conditional mode
ICRU	International Commission on Radiation Units
IMRT	Intensity-modulated radiation therapy
L	Left direction or PTV position
LINAC	Linear accelerator
MLC	Multi-leaf collimator
MR	Magnetic resonance
MRCAT	Magnetic resonance for calculating attenuation
MRF	Markov random field
MRI	Magnetic resonance imaging
OAR	Organ at risk
OS	Operating system
P	Posterior direction or PTV position
pCT	Pseudo-CT
PTV	Primary target volume
R	Right direction or PTV position
ROI	Region of interest
RT	Radiation therapy
RTOG	Radiation Therapy Oncology Group

SC	Superior-central PTV position
SE	Spin-echo
SIB	Simultaneously integrated boost
SRS	Stereotactic radiosurgery
SRT	Stereotactic radiotherapy
SNR	Signal-to-noise ratio
TPS	Treatment planning system
TM	Thermoplastic mask
TYKS	Turku University Hospital
UTE	Ultra-short echo time
VOI	Volume of interest
VMAT	Volumetric arc therapy
WBRT	Whole brain radiotherapy
WHO	World Health Organisation
WM	White matter

1 Introduction

CT imaging on its own has been used for decades in the radiotherapy (RT) planning process. Lately, MR imaging has grown in importance due to the superior soft-tissue contrast which allows better contouring of the tumour and organs at risk (OARs) to be avoided [1, 2]. The recent introduction of MRI has resulted in growing interest in trying to determine radiation attenuation information based on MR images only. Since the MRI signal rather correlates with proton density, it does not contain information about electron density of tissue compartments. The electron density is an important parameter in intensity modulated radiotherapy (IMRT) as it represents the ability of the tissue to attenuate X-rays in the form of external radiation beams generated by a linear accelerator (LINAC) [3]. Hence, the use of a computed tomography (CT) is still required in current clinical practice due to the linear relation, and therefore, easy conversion of Hounsfield units (HU) to information about the electron density of tissue. A so-called CT-density or -calibration tables are usually employed in this conversion process [4].

Acquisition of additional CT scan, however, negatively influences the patients (increased radiation burden) as well as clinical facilities, where every single additional step introduced into the RT treatment workflow increases workload. This in turn results in longer RT treatment-planning times and higher financial costs [1, 3, 4, 5]. Furthermore, a rigid MR-CT image registration, which introduces additional spatial uncertainties, is required for transferring the MRI-based organ and tumour delineations to the CT image. The mean cranial registration error was estimated as approximately 2 mm with similar values for other body sites. The acquisition of multiple image sets also introduces errors stemming from patient repositioning and anatomical changes as the time between scanning sessions may be counted in several days or even weeks [1]. All these issues related to increased workload and CT-MRI registration errors resulted in raised focus on research into simplified RT planning workflow using only the MR images that are in this workflow further utilised for the generation of so-called pseudo-CT (pCT) images [6]. These synthetic CTs entirely substitute the need for acquisition of additional CT scans, and therefore it allows decreasing both the workload and patient burden [5].

Multiple algorithms for pCT generation exist, with varying prediction accuracy as well as computational costs. The computational time is an important parameter especially in clinical practice where is usually required the availability of the accurate pCT within short reconstruction time [2] in order to allow the potential MRI reacquisition during a single imaging session. Each of algorithms for pCT prediction has its shortcomings originating mostly from the MR characteristics. MR imaging is not a convenient method for compact bone visualisation, and therefore, also for their segmentation as both, compact bones and air possess very low T2 constants causing the magnetic spins to dephase quickly. Short T2 relaxation times result in low-intensity in MR image voxels, and it is, therefore, not possible to easily distinguish bones from air cavities. The low contrast between voxels is a particular issue when one needs to separate air cavities from surrounding bones [1]

The MR-only RT workflow for prostate cancer treatment has been already granted

FDA approval [7] which is the essential step for its introduction to clinical practice. This MR-only solution known as the Magnetic Resonance for Calculating Attenuation (MRCAT) has been developed by Philips Healthcare. The MRCAT is based on a model-based classification method using mDixon MR imaging data. Here, the output is the pCT image encompassing five tissue segments that are the background air, fat, water-rich tissue, spongy bone, and compact bone. These compartments are filled by corresponding bulk HU values [8]. This technique of average HU value assignment to the segmented tissue labels is one of the characteristics of so-called voxel-based methods for pCT image generation.

The goal of this study is to investigate the feasibility of MR-only radiotherapy using the pCT images generated through similar voxel-based approach as it is currently done in the case of MRCAT. The primary aim of this thesis is, therefore, to find out what tissues need to be segmented based on the MR image in order to get a sufficient dose accuracy. Several studies were published proposing that MR-only bulk density based photon RT should be feasible for tumours located in the brain with dosimetric accuracy in a range of up to 2% [5, 9, 10]. Nonetheless, these studies mostly used pCT images with dual or triple bulk HU assignment for water, bone and air cavities respectively. This observation has further encouraged the research presented in this study where multiple versions of pCT images encompassing up to eight segmented compartments (bulk HU values) are used in order to find the stratification expressing the best dosimetric agreement with CT-based RT plans.

The first stage of this work is focused on generating of flattened CT through CT and MR image segmentation. These fCT images served as the substitution for the real MR-only based pCT images. The next steps are devoted to the generation of radiotherapy plans that were calculated on real CT images with varying tumour positions and recalculated on multiple versions of fCT images. The geometrical agreement and dose accuracy were assessed for all fCTs in comparison with real CT as the reference. The summary of results is shown and discussed in corresponding sections, and the fCT with the best dose accuracy is identified. This will allow an optimal design of the MR scan sequence that best visualises the tissues to be classified for the pCT brain image. Moreover, the classification methods used may serve as a starting point for the pCT generation. The work presented in this study will thereby enable further research into the introduction of MR-only radiation therapy for treatment of brain tumours into the clinical practice.

2 Background

2.1 Brain cancer overview

Cancer is one of the leading causes of death worldwide [11]. It is the group of diseases characterised by abnormal cell growth forming neoplasms that can potentially spread or invade to other body sites. Neoplasms occurring in intracranial tissues are collectively termed as brain tumours. Even though the incidence of cancer in central nervous system (CNS) is relatively low (less than 1% in Europe in 2012) [12], more than 120 brain tumour types have been identified according to the classification of the World Health Organisation (WHO) [13].

2.1.1 Brain tumours

There are two dominant groups of brain tumours. One group consists of benign tumours that do not invade surrounding and distant tissues. The second group constitutes cancerous or malignant neoplasms which can be further classified into primary and secondary tumours. Secondary tumours are represented by metastases that have expanded from primary cancers located in other parts of the body. The incidence of brain metastases is higher in comparison with primary malignant tumours. Secondary tumours arise mostly from lung, breast, melanoma, renal, or colon cancer and represent 40% of neoplasms diagnosed in the cranium [14]. Primary cranial tumours, on the other hand, originate directly from cranial cells and benign neoplasms and are therefore included in this category as well [15]. The WHO classification of CNS tumours is based on their histology as neoplasia usually arises from particular cell types (e.g. astrocytes, glial cells). The categorization of brain tumours is in addition to the cellular parameters further extended based on molecular parameters of particular tumour types [13]. The most common primary brain tumours include (in order of frequency) gliomas (50.4%), meningiomas (20.8%), pituitary adenomas (15%) and nerve sheath tumours (8%) [16].

Brain tumours are further classified by grades (I-IV). The purpose of using tumour grades is to simplify the search for the most appropriate treatment strategy and method as the grading identifies the structure and aggressivity level of the tumour. For instance, the vast majority of benign tumours belong to the grade I category. Tumours for which already exists the high risk of malignancy and can, therefore, possibly invade and destroy surrounding cells and tissues are classified by grade II. Neoplasms graded with III or IV are already malignant, and their prognosis is not widely defined as it highly depends on tumour location and accordingly by treatment and removing possibilities [17].

Exact causes of neoplasia in the brain are unknown. There have been identified risk factors such as ionising radiation, immune function, inherited susceptibility, metals and neurocarcinogens [18]. Reported inconsistency and sparsity of root causes for brain cancer are due to small patient cohorts and the variation in objectives of clinical trials. The small sample sizes can be explained by in general low survival rates, relative rareness of brain tumours and low participation of patients in individual studies [18, 19]. An overall five-year survival rate of 25.3% was reported for primary

brain tumours. However, this outlook varies significantly according to diagnosis and patient age. For instance, a five-year survival rate of only 3.3% was reported for the most aggressive and at the same time the most common malignant primary brain tumour, glioblastoma multiforme (GBM). In the case of lower grade gliomas, such as astrocytoma, lymphoma or malignant glioma five-year survival rates are lower than 40%, whereas more optimistic rates exceeding 70% were reported for oligodendrogliomas, ependymomas and pilocytic astrocytomas. In general, five-year survival rates tend to decrease with higher age of the patient [18]. The initial diagnosis of brain tumours is usually accomplished by medical imaging such as MRI. The appearance of selected brain tumour on MR images is shown in figure 2.1.

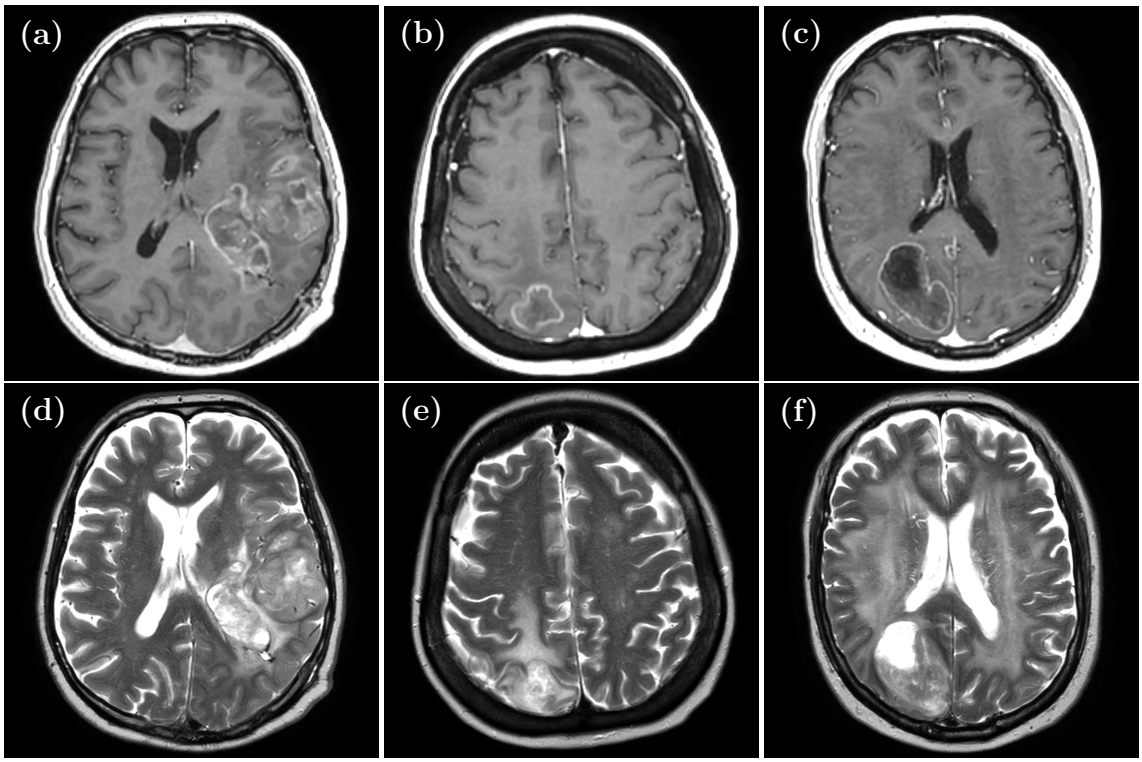

Figure 2.1: Examples of primary and secondary brain tumours and comparison of their appearance in T1 (a-c) and T2 (d-f) MR images. Primary glioblastoma after surgery (a, d) and secondary tumours (metastases) originating from renal (b, e) and lung (c, f) carcinomas without prior surgery.

2.1.2 Radiotherapy and other treatment options

Treatment of brain tumours may comprise a combination of radiotherapy, surgery, and chemotherapy. Nevertheless, the use of chemotherapy in brain cancer treatment is not a straightforward option as the hematoencephalic barrier prevents some drugs entering the brain [20]. Besides surgery, radiation therapy is considered to be the most effective treatment for brain tumours [21]. The primary aim in radiotherapy is to deliver the prescribed dose to the tumour while minimising the dose delivered to the adjacent tissues [15]. The advancement of intensity-modulated radiotherapy

(IMRT) using external beam delivery has substantially reduced the limitations of conventional RT methods [22]. This thesis is, therefore, primarily focused on the MR-only RT solution utilising IMRT delivery technique that is increasingly being used at the expense of conventional RT methods.

The fractionation and prescribed doses in RT rely heavily on the diagnosis as well as on the location and volume of the targeted lesion. Fractionated treatments are used in the event of cancerous tumours, whereas benign neoplasms are usually treated with a single RT session [23]. One of the issues relevant to primary malignant tumours is that invasive surgery is not curative even in grade II tumours, due to their infiltrative character. Nevertheless, the extent of tumour resection is of particular importance for disease prognosis. Consequently, postoperative or standalone radiotherapy remains an essential part of the majority brain tumour treatments [19]. In the case of metastatic lesions, a whole brain radiotherapy (WBRT) with the possibility of local dose boost can be applied after surgery [14]. However, standalone or postoperative stereotactic radiotherapy without WBRT can be employed in the secondary brain tumour treatment as well [24].

2.2 Radiotherapy simulation

Radiotherapy simulation process consists of multiple phases. The first phase comprises determining the diagnosis and selection of treatment strategy. The RT simulation continues with patient positioning and fixation for image acquisition which are to be unchanged throughout entire RT process. The patient is placed into comfortable and reproducible position (usually supine). However, another positioning is possible as well [14]. There are currently two basic types of fixation devices. The first and the most commonly used fixation device is a so-called thermoplastic mask. Another possibility is to use a fixation frame which is rigidly mounted to the patient head or skull using special bolts. The fixation frame provides higher positioning accuracy and further eliminates the risk of inter- and intra-fractional patient movements [25]. However, the use of thermoplastic masks (frameless SRT/SRS) is increasingly favoured even in the case of highly focused SRS and SRT treatments as novel frameless solutions provide sufficient positioning accuracy, superior patient comfort and is convenient for RT workflow in general [24].

The next stage of RT simulation is the collection of medical images. The acquisition of both, CT and MR images is the fundamental step in standard RT workflow, while only the MR scans are collected when the MR-only workflow is used. All the images should be acquired with the patient placed in the treatment position including all the positioning and fixation devices. These images are then registered and used as a basis for target and OAR delineation as well as RT planning in TPS [25]. MR and CT scanners with a wide bore and flat patient couches allowing better positioning can be employed in the RT simulation process [14].

2.2.1 Target volumes and organs at risk

Target volumes There exist three essential target volumes (TV) that are taken into consideration upon the radiotherapy planning. These volumes are the gross tumour volume (GTV), the clinical target volume (CTV) and the primary target volume (PTV) [14]. The concept of these volumes is shown in figure 2.2.

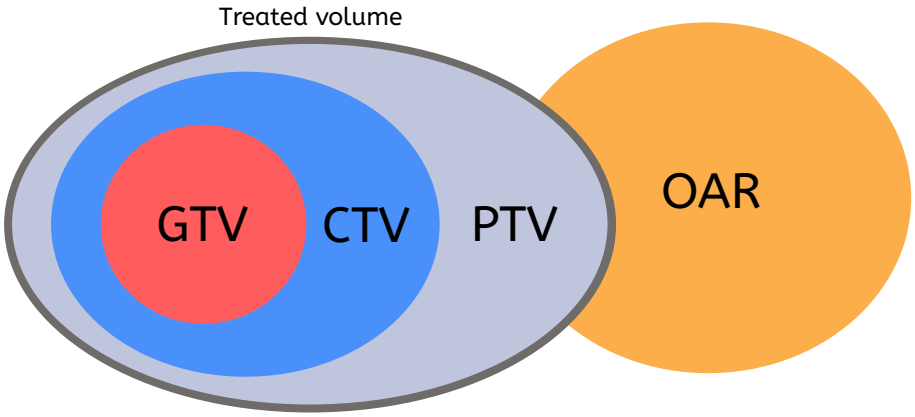

Figure 2.2: Schematic of a treated volume and organ at risk (OAR) located in the irradiated/patient volume. TV covers a primary target volume (PTV), a clinical target volume (CTV) and a gross tumour volume (GTV).

Gross tumour volume (GTV) represents the tumour mass observed upon clinical examination under anaesthesia or noninvasively by imaging. GTV always delineates the tissue mass having the highest density of tumour cells [14, 21]. Tumour shape, size and site may slightly differ depending on the employed imaging method, and the oncologist, therefore, delineates the final GTV after detailed examination [26]. The GTV is usually entirely removed by the surgery if possible [14].

Clinical target volume (CTV) covers in addition to GTV the area of subclinical microscopic disease or regional lymph node spread that are together with primary tumour part to be removed [26]. Since these affected areas are not detectable by imaging methods, the CTV is usually defined based on histological examination. Moreover, the selection of margin added to GTV is influenced by biological properties of the tumour [21, 14]. The standalone CTV contour would in an ideal case be sufficient for the focusing and modulation of radiation beams upon the RT planning in TPS. Nevertheless, changes in shape and size of internal organs, patient movements (inter- and intra-fractional) and other uncertainties inherent in RT setup must be taken into account in order to ensure full irradiation of the CTV [14, 26]. Consequently, another margin is added to the CTV forming the primary or planning target volume (PTV).

The PTV is then used for addressing dose prescriptions and beam targeting in TPS in order to assure a delivery of prescribed dose to the entire CTV [14, 21]. The treated volume (TV) also shown in figure 2.2 represents the tissue fraction that is aimed to receive a specified dose and is enclosed by a particular isodose surface. This may typically be the volume surrounded by the 95% isodose surface [14, 26]. The

aim of modern conformal RT delivery techniques in connection with 3D treatment planning is to optimise the RT plan in a way that TV precisely covers the PTV with as low excess as possible. This assures a precise coverage of PTV while neighbouring OARs are exposed to minimal irradiation [26]. The ratio between TV (95% isodose) and PTV, which is also known as conformity index (CI), is commonly used in the quality evaluation of RT plans.

Organs at risk Organs at risk (OARs) are critical normal tissue located in the proximity or directly adjoining the PTV. These bodies do not contain malignant cells and, consequently, they are not considered being treatment targets. Moreover, such structures may often be susceptible to the ionising radiation. The goal of RT plan optimisation ought, therefore, be to mitigate the risk of substantial morbidity by minimising irradiation of OARs. The structures to be taken into account for RT planning considerably vary in accordance with the treated anatomical site and the location, shape and size of the PTV [26]. The accurate delineation of OARs is of particular importance in the case of the brain where the irradiation may lead to hormonal impairment, neurocognitive and neurological alterations as well as to deficits in hearing and vision. Furthermore, precise delineation of OARs is indispensable for the IMRT and inverse planning process [27].

The following structures were repetitively reported in literature to be OARs for brain RT: lenses, eyes, cochleas, brainstem, pituitary gland, optic chiasm, nerves and tracts [15, 27, 28, 29]. Moreover, the sparing of the hippocampus and other structures has been studied as well in order to preclude the neurocognitive deficits [5, 27, 30]. The recommended dose constraints to avoid adverse effects for OARs in the brain are shown in table 2.1. However, these limits are further decreased in the event of treatments including single dose delivery fraction.

Table 2.1: Dose constraints for OARs in brain (RTOG, QUANTEC, [27])

	Eyes	**Lenses**	**Optical paths**	**Brain stem**	**Pituitary Gland**	**Cochleas**	**Brain**
D_{max}	<54 Gy	<5 - 10 Gy	<54 - 55 Gy	<54 Gy	<50 - 60 Gy	-	<60 - 72 Gy
D_{mean}	<35 Gy	-	-	-	-	<45 - 50 Gy	-

2.2.2 External beam radiation delivery

Linear accelerator (LINAC) machines are commonly used for a delivery of modern external beam radiation therapy. The treatment head mounted on a rotatable gantry is the core component of every LINAC. This head is equipped with X-ray target, scattering foil, flattening filter, ion chamber, and secondary collimator. Photons of a megavoltage (MV) range are produced upon a collision of accelerated electrons with the X-ray target. This photon beam is firstly formed by the primary collimator and then pass through the flattening filter which makes the X-ray intensity uniform across the entire beam field. The role of the ion chamber is to monitor the field symmetry, integrated dose and dose rate in monitor units (MU). The radiation beam

is further shaped by the secondary collimator after passing through the ion chamber. This dynamically movable collimator incorporates two pairs of jaws and the multileaf collimator (MLC) which is the key component for the IMRT treatment delivery [25]. Figure 2.3 shows an example of the LINAC machine and the schematic image of how the radiation beam comes out from the LINAC and is then formed by the different treatment head layers and focused towards the target.

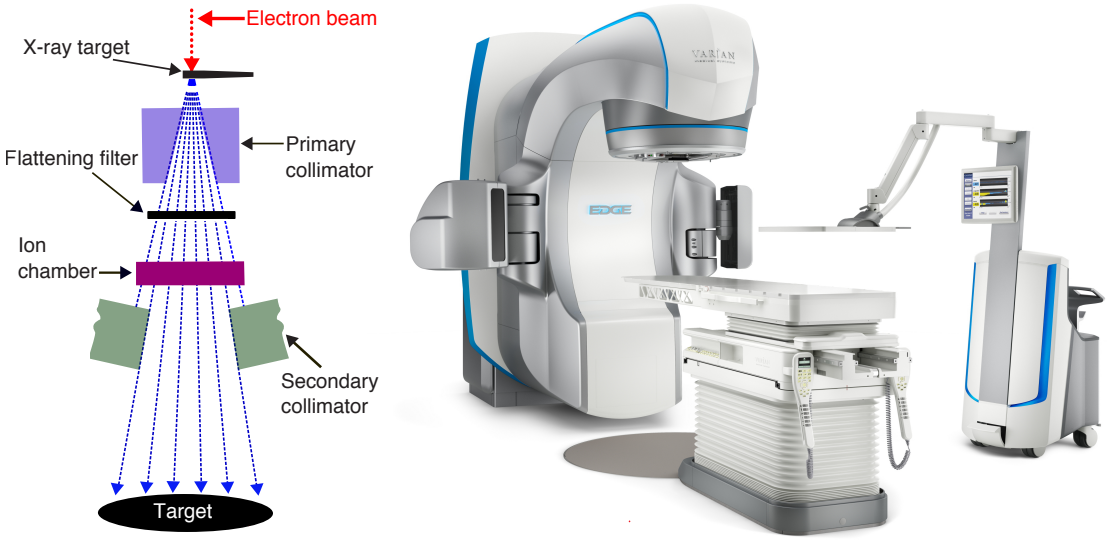

Figure 2.3: Components of the LINAC treatment head and beam penumbra for photon (X-ray) radiotherapy setup (left). An example of LINAC machine (right) - courtesy of Varian Medical Systems (source: [31]).

2.2.3 Intensity-modulated radiotherapy

Intensity modulation Modern LINAC machines are equipped with a dynamically controlled multi-leaf collimator (MLC) enabling dynamic modulation of the beam radiation field. One of the fundamental MLC parameters is the number of leaf-pairs where each pair is composed of two opposing leaves [32]. Every single pair of leaves forms a sliding window. The width of such window changes as leaf-pair moves and so that individual points in the patient volume are irradiated for different time periods. These points, therefore, receive varying doses [26]. This is a fundamental principle of the intensity modulation upon the RT treatment delivery. The MLC scheme and principle of intensity modulation is shown in figure 2.4.

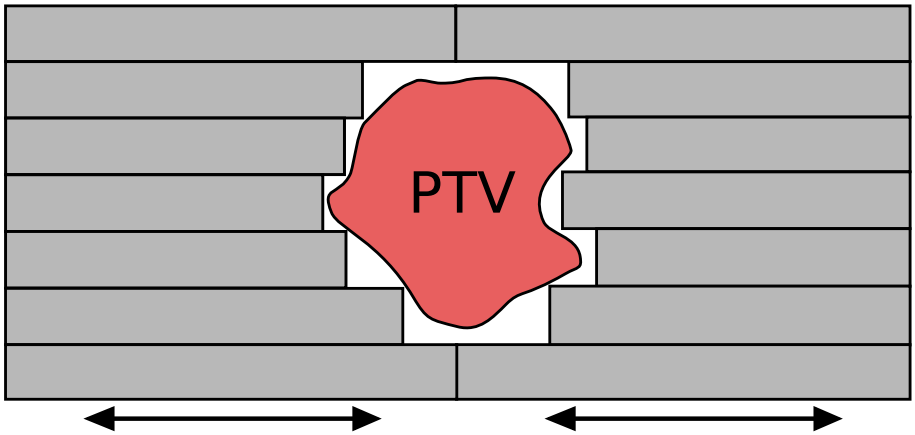

Figure 2.4: Intensity modulation by use of multi-leaf collimator (MLC)

Inverse planning A forward planning in 3D conformal RT provides a simple tissue sparing with MLC shaped to cover only the PTV volume from multiple gantry angles in order to achieve a uniform target coverage [14]. An inverse planning is, however, way more sophisticated and computationally demanding process exploiting the entire potential of RT delivery methods carried out with MLC-based LINAC. Several inverse planning techniques exist, nevertheless, all of them employ certain a priori known fixed parameters and specific free parameters to be optimised by the TPS. The fixed parameters are usually the MV energy, a number of beams or arcs and their directions while the remaining free parameters are the varying intensities delivered from each of selected gantry angles [26]. The optimisation in inverse planning begins with the specification of initial objective functions that constitute the starting points of the optimisation process [33].

The set of initial objective functions consolidates information about desired sparing of OARs and desired PTV coverage. The TPS then strives to achieve these goals through optimisation which is based on minimising a cost function. A choice of the cost function is crucial as its alternation while using the same inverse planning method would result in a different result. The optimisation results can be further modified by employing so-called biologically-based cost functions [26]. Apart from high computational costs, the other drawback of inverse planning is that the

impact of selected beam positions on the resulting dose distribution is unknown until the plan optimisation has been accomplished. This usually results in a need for several optimisation trials with different objective functions in order to obtain a well-optimised plan [34]. Consequently, RT plan quality assessment strategies must be used in order to determine whether the optimised solution is acceptable or not [35].

Treatment delivery methods RT delivery methods taking advantage of the intensity modulation are considered to be the state of the art of current RT. There are two basic types of such techniques. The first method is an Intensity Modulated Radiotherapy (IMRT) using a so-called step-and-shoot radiation delivery approach. The step-and-shoot stands for the principle where the LINAC gantry stops in predefined angle (beam direction), and the intensity modulation (shooting step) is carried out by movement of MLC leaves in time. In IMRT treatment planning, the physicist usually defines a number of beams and their directions based on intuition and experience. Intensity profiles are then calculated by the use of the inverse planning [34].

The second and more recent method using intensity modulation and inverse planning is a Volumetric Modulated Arc Therapy (VMAT) also known as SmartArc (Philips) or RapidArc (Varian) [36]. VMAT is a novel RT delivery technique providing highly conformal dose distribution and coverage within the PTV while sparing surrounding OARs at the same time. It is possible to achieve a high degree of normal tissues sparing due to the very steep dose gradients around the target volume. The principle of VMAT lies in dynamic radiation delivery while both LINAC gantry and MLC leaves are moving simultaneously during the treatment session [37]. Key limiting factors in VMAT treatment delivery are machine parameters such as the gantry rotation speed, the velocity of MLC leaves and a number of monitor units (MU) per minute. Hence, the LINAC gantry has to move slowly when one wants to achieve high-intensity modulation quality in all of the arc angles. The low speed of gantry movement is crucial especially in the case of hypofractionated treatments where high doses requiring high MU counts are delivered in a single fraction [32].

The VMAT technique is usually employed in SRT/SRS, and palliative treatments of metastases or in cases, where the invasive surgery would pose a high risk of permanent disability. The major advantage of VMAT is a reduction in treatment delivery time while PTV coverage is comparable or superior to the IMRT [38], with enhanced sparing of OARs. However, the optimisation of VMAT plan is a computationally demanding process with high requirements on the computational HW and the computation time is, therefore, longer in comparison with IMRT [39].

2.2.4 Beam and arc arrangement

A basic coplanar arrangement where beams or arcs are allocated within a single plane is the most commonly used RT setup in clinical practice [37]. Examples of IMRT and VMAT plans with coplanar arrangements of beam or arcs are shown in figure 2.5.

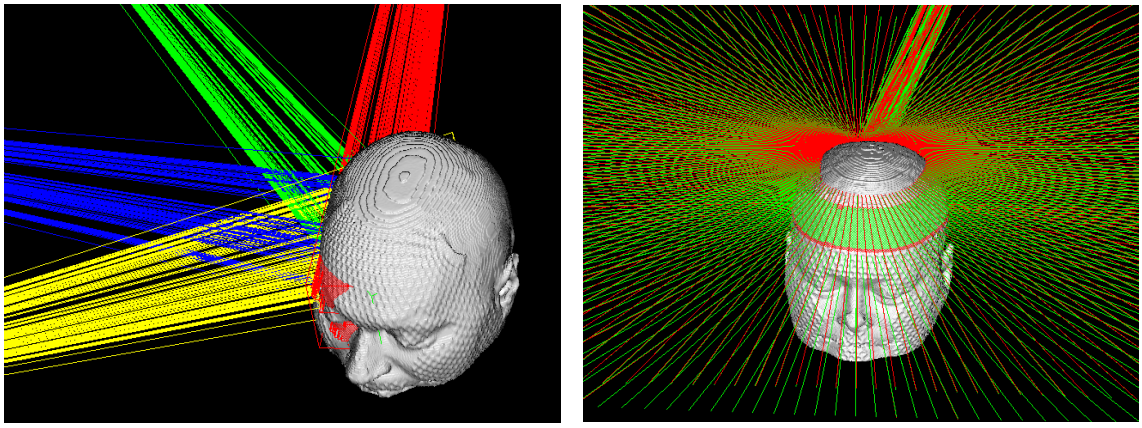

Figure 2.5: Examples of a coplanar arrangement of IMRT beams (left) and VMAT full arcs (right). Here all beams or arcs are allocated in the single plane, and therefore, the rotation of patient couch is not required.

However, novel LINAC machines are equipped with couches capable of dynamic rotation during treatment delivery enabling non-coplanar beam directions or arc trajectories that take advantage of the 4π space [40]. It has been observed that techniques using co-planar arc/beam setup irradiate contralateral OARs, such as the optic nerves, in order to sufficiently cover the PTV if it is located in the proximity of those sensitive structures. This observation has brought forward the hypothesis that techniques involving a non-coplanar beam setup might help to decrease doses delivered into such OARs [41, 42]. For example, superior sparing of contralateral optic paths has been reported while using the IMRT plans with non-coplanar beam arrangement [39].

Moreover, a future use of 4π non-coplanar radiotherapy could potentially improve the outcome of glioblastoma-multiforme (GBM) treatment through extreme dose escalation with very steep dose gradients surrounding the PTV [40]. This phenomenon can be explained by the fact that non-coplanar arcs/beams supply an additional degree of freedom for IMRT or VMAT planning and may allow for noticeable quality enhancement in some cases of advanced RT plans [34]. The use of non-coplanar beam/arc geometry, therefore, empowers further improvement in the OAR sparing and the target coverage [34, 25]. Examples of IMRT and VMAT plans with non-coplanar arrangements of beam or arcs are shown in figure 2.6.

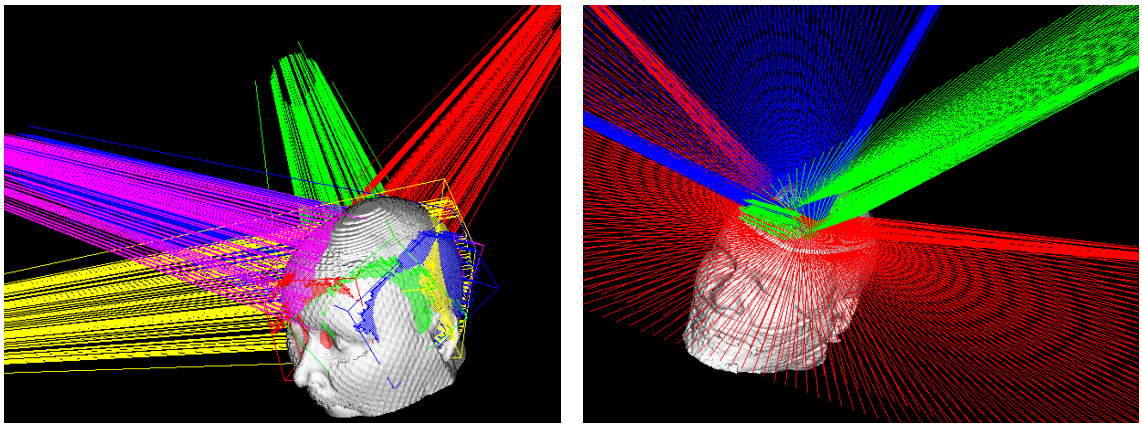

Figure 2.6: An example of a non-coplanar (left) arrangement of IMRT beams. Here, the purple beam (forehead) is non-coplanar to the others. An example of use of multiple non-copanar arcs in VMAT (right).

2.3 MR-only radiotherapy

The entire potential of modern RT delivery methods such as IMRT and VMAT can be fully utilised only when the precise TV and OAR delineations are available. MR imaging provides superior soft tissue contrast allowing for highly precise delineation as compared to CT. Nonetheless, acquisition of CT image is still a key part of conventional RT simulation workflow as it provides information about electron density needed for dose calculations [43]. The patient positioning at treatment further takes advantage from the superior bone contrast of CT image. This positioning is carried out by registration of CT image with cone-beam computed tomography (CBCT) or by digitally reconstructed radiograph (DRR) with the kV or MV image. MV images are acquired directly by LINAC (portal imaging) or by an additional imaging device installed on the LINAC or in the treatment room (kV imaging) upon the treatment session with the patient positioned on the table [44].

2.3.1 MR-only radiotherapy workflow

Conventional RT simulation workflow consists of five stages that are CT and MRI acquisition, image registration, structure contouring, and RT planning at the TPS [1]. However, the patient repositioning and anatomical changes pose a risk of a lower RT simulation accuracy as the time between imaging sessions can be counted in days or weeks. Moreover, the registration error introduces a systematic spatial uncertainty into the RT simulation process when transferring delineated structures from MRI to the CT [43]. The dosimetric impact is increased when small structures are irradiated or when the tumour is located in the proximity of sensitive organs. This could be of particular importance in the case of small tumours found in the brain [45].

The MR-only approach allows reducing the entire RT simulation process into three stages as there is no need for CT acquisition and CT-MRI registration step. The comparison of the standard and MR-only workflow is shown by the diagram in figure 2.7. MRI-only RT simulation would eliminate the systematic registration error

which has been reported to be in the range between 2 mm and 5 mm depending on the treated anatomy [43, 46]. Moreover, it would reduce the treatment-related financial costs, and decrease the patient discomfort related to the acquisition of additional CT scan. Adaptive RT treatment, where inter-fractional anatomical changes are taken into account, is frequently discussed as a part of MRI-only RT workflow for the future [1, 3, 4, 5].

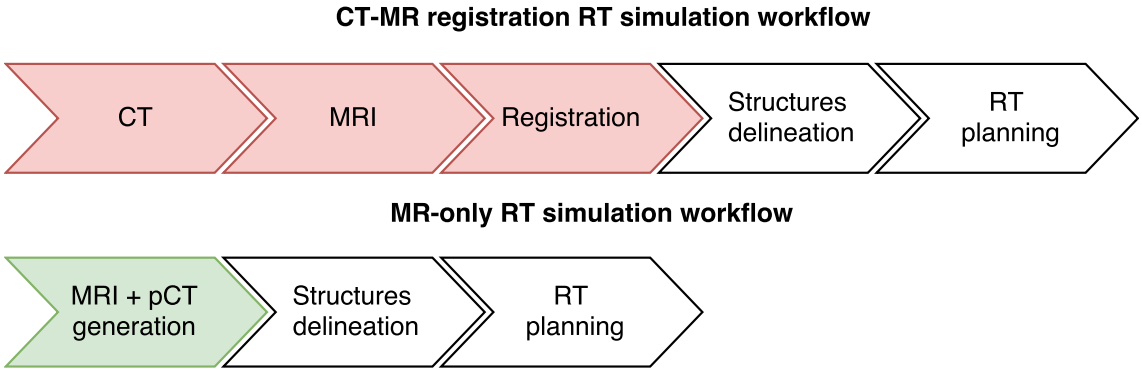

Figure 2.7: Comparison of conventional and MR-only workflow in RT simulation.

Nevertheless, there are several concerns associated with MRI-only RT. The main issue is that MRI intensities correlate with the magnetic relaxation and proton density rather than electron density and radiation attenuation properties of tissue. Consequently, the voxel intensity of MRI image does not reflect radiation attenuation characteristics of the tissue as it is in the case of CT image. This results in contrast ambiguity in the case of tissue types like air and bone which both appear dark on the MRI despite having distinctive electron densities. The lack of correspondence between the voxel intensity and the associated electron density presents a challenge for performing dose calculations using MR images as a basis [43].

Further challenges are posed by geometrical distortions originating from magnet inhomogeneities, gradient non-linearity and artefacts induced by the patient [46]. Spatial variance in the MRI signal of tissue (such as subcutaneous fat most notably) convolutes its conversion into Hounsfield unit (HU). Normalisation of signal intensities and inhomogeneity corrections may need to be applied on the MR images. The final HU or electron density map is called synthetic or pseudo-CT (pCT) [43].

2.3.2 Pseudo-CT generation methods

Several methods of pCT image generation using one or more MRI contrasts have been reported in literature. These methods can be classified into two basic groups. The first group is represented by voxel- or data-based approaches, and so-called atlas-based methods belong to the second category. Patch-based methods can be included in this second category as well. Moreover, the use of hybrid or mixed approach of pCT generation taking advantage of both atlas- and voxel-based approaches has been reported as well.

Voxel-based methods In the voxel-based approach, individual voxel intensities of the MRI scan are used for prediction of pCT voxel HU values, either by employing a regression model to generate a continuous-valued image or by segmentation and consecutive bulk HU value assignment [1, 47, 48]. However, the generation of continuous-valued pCT is challenging due to the degeneracy of the fitted relationship between image intensities in MRI and CT images [47]. Since the MR contrast is utilised independently of the spatial location of the voxel, relatively low computational demands constitute a potential advantage of voxel-based methods for the use in clinical practice [43].

Besides the reliability and the prediction accuracy, the pCT recon time is a critical factor for the successful implementation of MR-only workflow in the clinical practice. However, the very short T2 relaxation time of cortical bone represents a difficulty for accurate voxel-based pCT prediction. Neither air nor bone provides any signal when standard clinical MR imaging sequences are used. Consequently, a dedicated MR sequence together with post-processing steps such as air-mask generation must be utilised for obtaining a correct classification of bones and air cavities when employing voxel-based methods for pCT generation [48, 49].

Atlas-based methods In the atlas-based approach, an atlas consisting of co-registered CT and MR image pairs is employed in pCT generation. The target MR image is firstly non-rigidly registered with all the MR images that form the atlas. The number of registration steps depends on the extent of this atlas. A single registration step is needed in the case when the atlas includes only one CT-MR pair of template (average) patient [43]. Nonetheless, the use a so-called multi-atlas approach is more common due to its higher pCT prediction accuracy. This approach requires the execution of multiple target-atlas MRI registration steps, and therefore, is less computationally attractive. Secondly, the displacement fields obtained from the registration process are applied to all of the CT scans paired with MR images in the atlas [48]. And finally, a single pCT image is obtained by fusion of these deformed CT images. In this fusion process, pure intensity averaging, majority voting, or other more sophisticated methods are employed in the determining of final voxel HU values in pCT image [43].

Atlas-based methods provide the solution for separation of air and bone even in the case when standard MRI sequences are employed. However, the atlas-based approach suffers from uncertainty in the registration of the atlas [50] and poorly able to cope with high variability in electron density and/or anatomy between patients [47]. Especially the anatomy of an atypical shape such as surgical implants or missing tissues poses a particular problem for atlas-based pCT generation [2]. Consequently, post-processing steps may play a crucial role in increasing the pCT prediction accuracy of such atlas-based approaches [50].

Other methods Since both atlas- and voxel-based methods each have favourable and unfavourable factors so-called hybrid methods aiming to utilise advantage of both categories have been reported in literature as well [43]. Such hybrid method could, for instance, be based on the estimation of two probability density functions

for each voxel, one based on Bayesian statistics and the other based on deformable registration. These two probabilities would be then merged into single probability density function determining the final HU value assigned to the voxel [51].

A different hybrid approach could, for instance, be built on classical atlas-based methods whereas voxel-based methods would be employed in the image post-processing. These processing steps would aim to improve the prediction accuracy in regions with individual anatomies [48]. The last category is formed by the hybrid atlas methods combining several approaches within the atlas-based methods. This could be a method integrating patch-based methods using pattern recognition together with a classic deformable registration approach [1, 43].

2.3.3 MR imaging parameters

Generation of pCT poses some special requirements for the MR imaging parameters. Multiple strategies for selection of MR imaging parameters have been reported in literature. The preferred image contrast is highly influenced by the method of pCT generation.

Atlas-based methods In atlas-based methods clinical MRI sequences are usually employed. MR images obtained with standard clinical sequences [1] are preferred simply because of their general availability, which is of crucial importance when multiple CT-MR co-registered image pairs are needed to build an atlas. These clinical sequences are T2 (long TR, long TE) and T1 (short TR, short TE) weighted depending either on the transverse (T2) or longitudinal (T1) tissue relaxation. The choice of TR and TE are then the main factors influencing the final image contrast. The acquisition of MR images is the most commonly carried out using either of a gradient echo (GE) or spin echo (SE) sequences [43].

Voxel-based methods Voxel-based methods for pCT generation usually require the use of special MR sequences. These sequences typically produce images of multiple contrasts mostly specialised on bone visualisation, which is a very challenging task in the case of MR imaging. The acquisition of such MR images is usually accomplished by the use either of Dixon or dual ultrashort echo time (dUTE) sequences [52]. Lately, though zero TE MR imaging has shown even more promise than dUTE [53].

Dixon is a family of water-fat splitting sequences and relies on the chemical shift between the resonance frequencies of water and fat. Dixon images can be weighted in the direction of T2, T1 or ρ as the separation of fat/water is not based on TE or TR.

MRI sequences based on dUTE are specialised on visualisation of cortical bones and have an ultra short T2 relaxation time [43]. The use of this sequence type, therefore, allows separating bone from air voxels [52]. The initial signal is in dUTE sequence collected immediately after the excitation, and the second signal is acquired later with a longer echo-time. The initial image is T1 or ρ weighted depending on the flip-angle. The second image has a T2 or T1 weighted contrast depending on the flip-angle and the echo-time [43]. However, utilisation of dUTE sequence

introduces prediction errors into pCT images, particularly at tissue interfaces located in the proximity of nasal cavities and ears. This has been associated with low SNR, susceptibility effects as well as partial volume effects in dUTE images [54, 55].

2.4 Quality assurance in MR-only RT

2.4.1 Dose-volume histogram

The output provided by TPS usually encompasses an enormous amount of information about the dose distribution. The interpretation and evaluation of such data would be difficult without the availability of a method that would condense data from the 3D dose distribution in the form of simple 2D graph [26, 25].

Such a graph is called a dose-volume histogram (DVH) which is a plot of dose on the x-axis versus the volume of the particular structure on the y-axis. There exists two versions of this graph differing in the way of how the absorbed dose is interpreted [56]. The first version is a differential DVH, which directly shows the absolute or relative dose value assigned to a particular bin in the histogram [25]. The second and more frequently used is the cumulative version of DVH. Here each histogram point captures dose that has been accumulated from previous bins starting with the bin containing the highest dose moving in the direction towards to the one with zero dose. In other words, such a DVH displays the dose absorbed in a particular volumetric fraction of the target volume or OAR [26, 25]. The example of cumulative DVH is shown in figure 2.8.

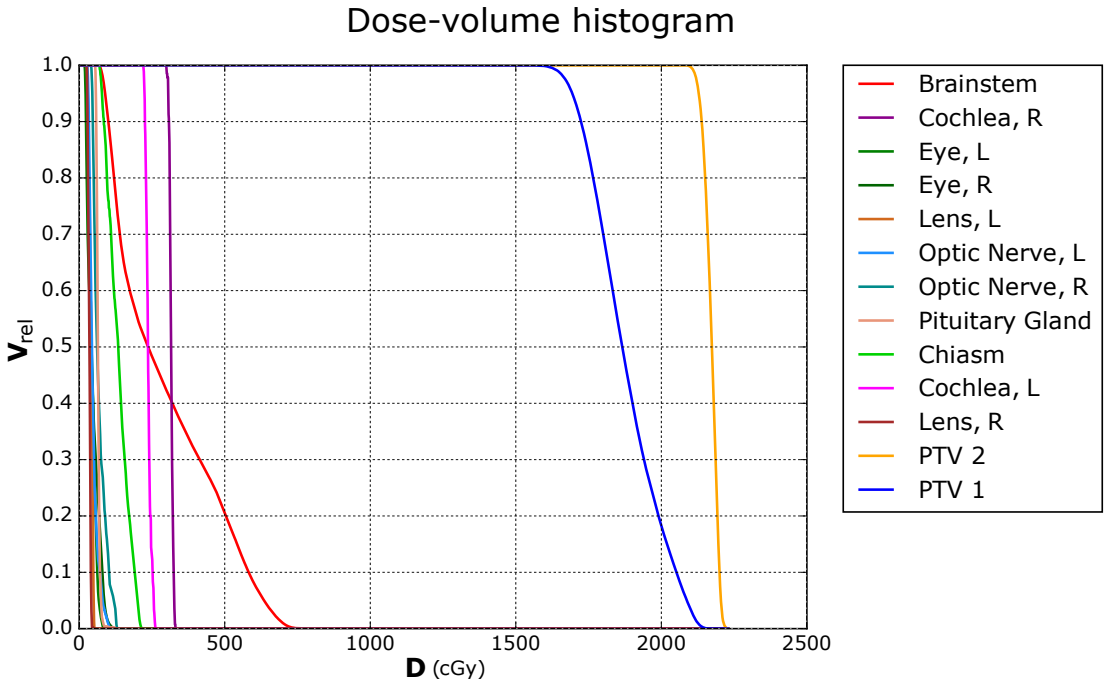

Figure 2.8: An example of cumulative DVH showing two PTVs and selected OARs in the brain. The blue line indicates that all of the PTV 1 receives a dose of 1600 cGy, whereas roughly 20% receives a dose higher than 2000 cGy.

The shape and area of the DVH curve provide information whether the target volume is adequately covered with a prescribed dose and whether the dose delivered to OARs is within the acceptable limits [14]. In the ideal case, the DVH would show the target at 100% and then drop immediately to zero indicating that the prescribed dose conformally covers the entire target volume. The OARs lines would, on the other hand, fall quickly to zero, implying that no notable dose has been accumulated in their volumes [56].

The DVH is very powerful tool for dose comparisons, especially if one needs to compare dose results of two or more RT plans [25]. Consequently, this method of dose comparison is included in the vast majority of studies on MR-only radiotherapy where the CT-based plans and dose distributions are usually compared with dose distributions recalculated on pCT [14]. Nonetheless, there are some aspects that should be taken into account in the planning and evaluation using DVH analysis. The first aspect is that the dose sampling resolution that can have an impact on the outcomes of the DVH analysis, particularly in regions with steep dose gradients. Moreover, the main limitation of DVH lies in the lack of spatial information. The DVHs simply show that e.g. cold and hot spots exist within the dose distribution, but their position is not indicated, nor whether there are multiple small low- or high-dose regions or a just a large one [26]. The use of other methods capturing the spatial information is therefore employed in dose evaluations as complementary to DVH analysis.

2.4.2 Gamma analysis

Gamma analysis was initially developed for comparison of measured and calculated dose distributions as part of the TPS commissioning process [57]. This quality assurance (QA) method takes into account both the dose and distance criteria. The gamma analysis execution starts with computation of $\gamma(\vec{r_t}, \vec{r_c})$ series, which is defined as

$$\gamma(\vec{r_t}, \vec{r_c}) \quad = \quad \sqrt{\frac{|\vec{r_t}, \vec{r_c}|^2}{DTA^2} + \frac{|D(\vec{r_c}) - D(\vec{r_t}))|^2}{D_{max}^2}}, \tag{2.1}$$

where $\vec{r_t}$ is the reference and $\vec{r_c}$ is the comparison point in the dose distributions to be compared. The distance between evaluated points and dose difference are termed as $|\vec{r_t}, \vec{r_c}|$ and $|D(\vec{r_c}) - D(\vec{r_t}))|$, respectively. The resulting gamma index is defined as $\gamma(\vec{r_c}) = min\,\gamma(\vec{r_t}, \vec{r_c})$, and serves as a quality measurement. The gamma index indicates the level of failure in the areas that do not meet the acceptance criteria and determines quality in regions that pass the analysis. Since this index is determined for each voxel in dose grid separately, it can be easily presented as a so-called gamma distribution that is overlaid on the CT or pCT image [57, 58].

The essential input parameter for gamma analysis is a pass–fail criterion which is determined by the user for both the distance-to-agreement (DTA) and maximum dose difference (D_{max}), e.g. 2% and 2 mm. These criteria can be identified as scaling factors in equation (2.1), and have equivalent significance in the evaluation of the

gamma analysis. Dose distribution points failing one or both criteria are pinpointed on a composite distribution [58]. The normalisation for dose difference can be either local (ΔD between voxels) or global where ΔD is defined as e.g. percentage of maximum dose point of the reference dose distribution [59].

The other parameters that need to be determined by a user are the passing rate and dose cutoff. The passing rate is threshold used for decision of whether the entire dose distribution passes or fails the gamma analysis. This threshold is defined as a percentile of dose grid points needed for passing the test. The dose cutoff is an optional parameter reducing region within which is the gamma analysis calculated. This region of dose grid is determined by isodose in percents [57]. The point of adding the cutoff parameter is that gamma index gives a relative difference in dose. For instance, if the absolute dose is small, a large relative difference then does not have any clinical impact. The fundamental principle of the gamma analysis is shown in figure 2.9.

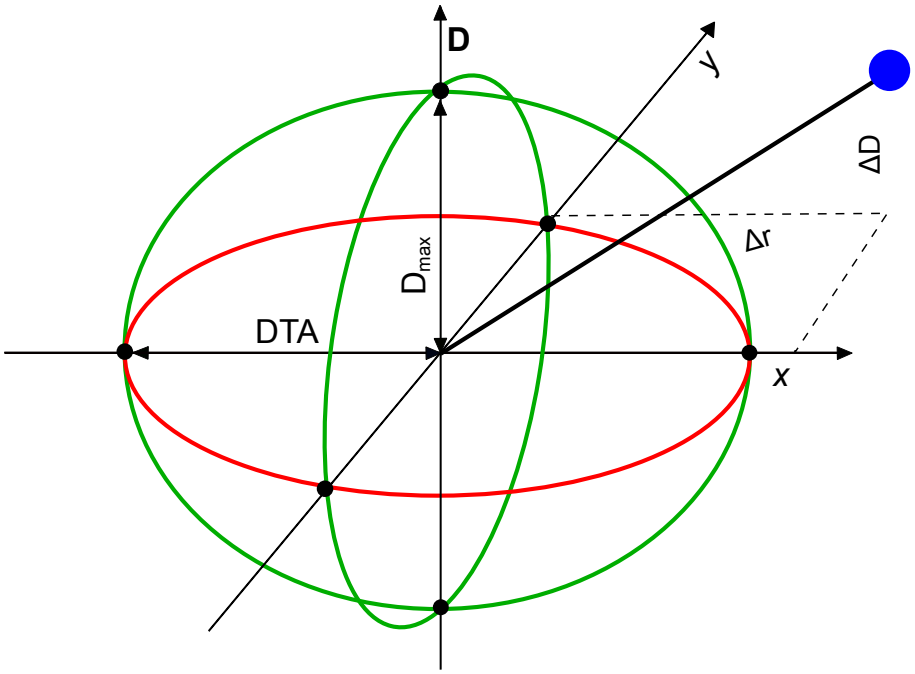

Figure 2.9: The simplified concept of gamma analysis for 2D dose distribution. x, y, D are spatial and dose dimensions. D_{max} is maximum acceptable dose difference. DTA criterion is determined by the radius of the red horizontal circle (sphere for 3D distribution). Δr, ΔD are spatial and dose difference of the blue point. The blue point, in this case, fails both criteria (D_{max}, DTA) of the analysis [58].

2.4.3 Spatial accuracy requirements

The CT-MR fusion introduces a registration error into the standard RT simulation workflow. This mean systematic error has been reported to be approximately $1.8 \pm 2.2\,\text{mm}$ (average displacement and one standard deviation) in the case of brain RT [60, 61]. This value is comparable to other body sites such as the prostate [46].

The MR-only workflow could, therefore, reduce these registration errors between MR and CT scans [10, 47]. However, MR imaging is known to be susceptible to distortions that alter both the relative intensity (spatial variation) and spatial representation of displayed anatomical structures. These distortions originate either from the MRI system itself or may also be induced by the patient.

The source of the object related distortions are variations in chemical shift and susceptibility of the sample, while the system-induced distortions are caused by gradient nonlinearities and inhomogeneities in the main magnetic field B_0. Consequently, the MR images intended for MR-only RT simulation have to be corrected to a level that would be acceptable for radiation therapy planning. The overall spatial error should be lower than 2 mm [10] in order to not exceed the registration error of standard workflow when both CT and MR images are used in RT planning process. Regarding geometrical and image intensity accuracy, a distance to the agreement of $\Delta r = 2\,\text{mm}$ and a deviation of $\Delta H = 100\,\text{HU}$ have been claimed to be acceptance levels for pCT image [48].

Even with the use of the stereotactic frame, an average CT-MRI fusion error of around 2 mm was stated for SRT [60]. Cranial SRT and SRS are both increasingly carried out by use of frameless fixation devices [62] as the similar error of 2 mm was reported to be feasible for frameless workflow. However, there is a 5% risk of outliers of up to 5 mm [63]. Since small margins are usually used in modern IMRT and VMAT brain plans ($< 5\,\text{mm}$), such registration inaccuracies could potentially cause a critical overdose in OARs or target miss [64]. MR-only RT could possibly reduce these registration errors.

2.4.4 Dose accuracy requirements

Establishing dose accuracy requirements is a key step in the comparison of the MR-only brain RT workflow to the standard workflow. MR only RT workflow was reported to be acceptable when the PTV mean dose deviates less than 2% from the original CT-based calculation in 95% of patients [5]. Nevertheless, limits for clinically acceptable deviations in other DVH statistics have not been yet established for the brain. Consequently, a proposal has been made of initiating a population-based study comparing CT-based dose calculations with those carried out on the pCT [5].

Regarding the gamma analysis, the 1%/1 mm, 2%/2 mm and 3%/3 mm criteria were previously used for comparisons of dose distributions calculated on pCT and CT images of head [65, 59]. However, the specific clinically acceptable gamma passing rates for brain have not been reported in any of the available literature sources. The overall impression from the literature is that a gamma criteria of 1%/1 mm, 2%/2 mm or their combination could be used as an indication of clinically acceptable dose comparison.

3 Materials and Methods

3.1 Clinical data

Radiotherapy planning datasets were obtained from Turku University Hospital in Finland (TYKS), from where two patient cohorts were selected for analyses presented in this thesis. This data included patients with various diagnoses and treatment strategies. The first cohort of 10 cases was aimed for the bulk HU estimation and subsequent PTV position dose analysis. The second sample of 10 cases (see table 3.2), partially overlapping with the first cohort, was used for a technical approximation of clinical plans.

3.1.1 Data characteristics

The majority of treatment strategies encompassed the combination of surgery followed by radiotherapy. Nonetheless, few patient cases with the standalone use of the radiotherapy were observed as well. RT-only treatments were typically either palliative treatments, treatments of tumours located in the proximity of brainstem, or treatments of the small benign lesions where the surgery would not be reasonable or would pose a very high risk of permanent disability.

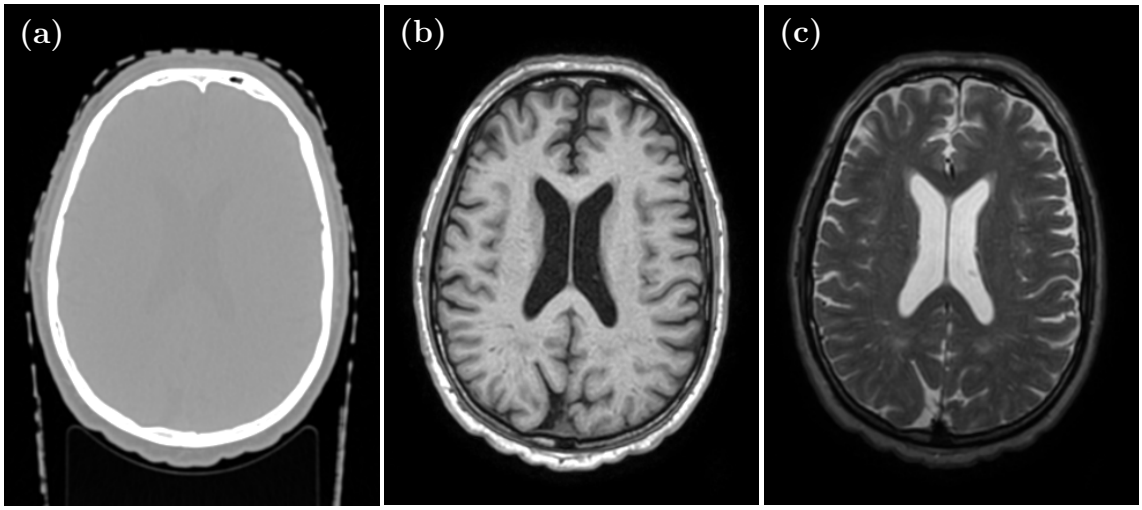

Figure 3.1: Example of the patient image set. CT (a), T1 weighted (b) and T2 weighted MR image (c).

CT and MRI datasets including FLAIR, T1 and T2 weighted images were available for the majority of the patient cases. The information about the spatial registration between these CT and MR images was attached as well. The radiotherapy planning data comprised RT structures, RT dose, and RT plan exported from Eclipse (Varian Medical Systems, USA) treatment planning system (TPS) in the form of DICOM files. The RT structure file contained delineations of both, the anatomy of OARs, and target volumes (TVs) in the form of 2D contour in axial slices. The RT dose file included a 3D dose distribution, which was the outcome of RT plan optimisation

algorithm implemented in TPS. The RT plan DICOM file contained parameters, such as beam type and directions, positions of MLC leaves at all the control points, dose prescriptions, and other physical parameters that are usually estimated by medical physicist upon the RT planning process.

3.1.2 Image parameters

The image sets showed a high variation in parameters such as voxel size, the field of view (FOV) in the case of CT, and contrast in the case of MR images. Even though a resolution was roughly consistent in axial slices among all CT images (512×512 voxels), the problem was a variation in slice thickness ($1 - 2.5\,\mathrm{mm}$) having an impact on the overall spatial resolution. The low spatial resolution increases the incidence of partial volume effects that play a crucial role in a specificity of tissue segmentation [66, 67] and consequently in bulk HU estimations as well. In the case of MRI, the small voxel size causes a decrease of SNR and increase in image acquisition time. The variation in contrast and voxel intensity was in our case a particular issue in the MR image segmentation, which was needed for the brain tissue stratification.

3.1.3 Pathologies and artefacts

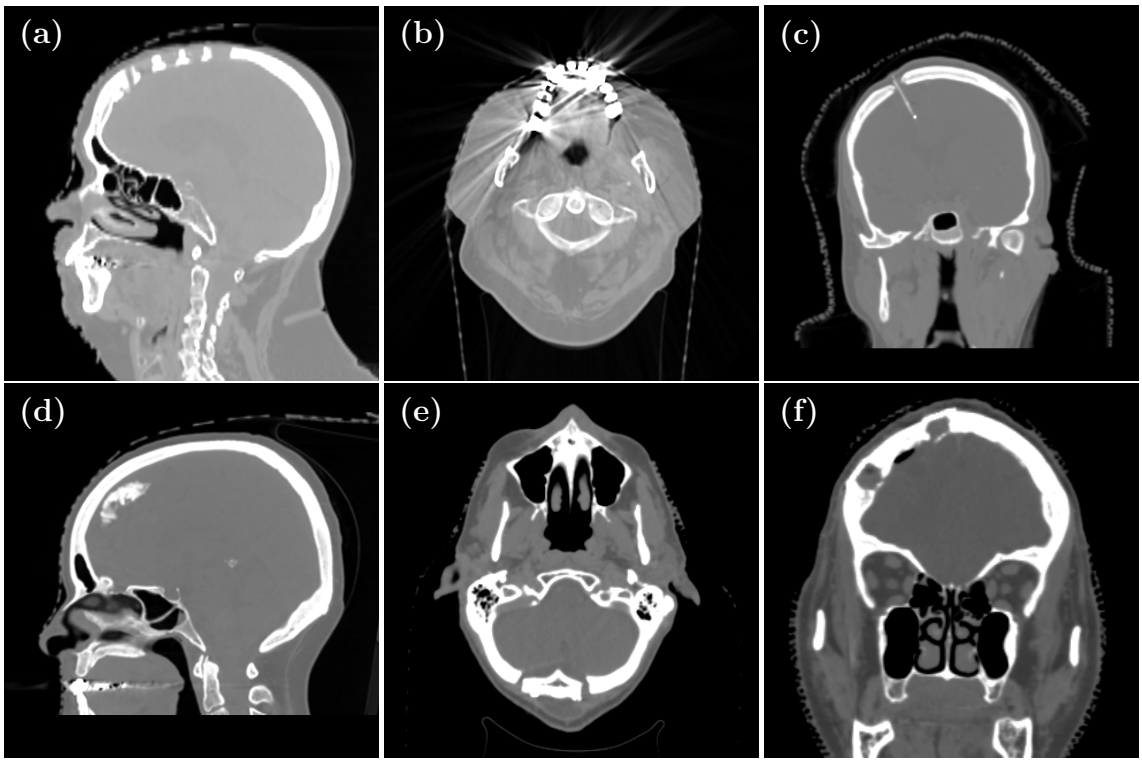

Figure 3.2: Artefacts and pathologies observed in multiple head CT images. Multiple drilling sites (a), metallic artefacts (b), metal probe (c), extensive calcifications (d), occipital craniotomy (e), and skull clips (f).

The majority of obtained images showed pathologies including skull drills and resections. Moreover, calcifications and artefacts from dental implants were abundant as well, as patients with the brain cancer usually belong to the upper age group (40-65 year in the case of gliomas) [68]. Metallic implants are responsible for artefacts or distortions in both CT and MR images. The combination of mechanisms such as scattering, beam hardening, Poisson noise and edge effects are the cause of these artefacts in the CT image [69]. Figure 3.2 shows six selected patients with apparent pathologies that were visible in their CT images.

3.1.4 Data preprocessing

Several preprocessing steps were undertaken to mitigate the impact of image parameters variation, artefacts and individual pathologies on estimates of bulk tissue HU that were issued for the fCT generation.

Firstly, all the CT and T1 weighted MR images were inspected visually in order to select 10 suitable patients cases for the estimation of bulk tissue HU values. These cases should include images free from metallic artefacts, craniotomy and low brain tissue contrast in T1 images. Selected CT images were further cropped using an annotation ROI tool in the 3D Slicer (BWH, USA) [70] in order to unify the FOV among all the selected cases. The C2 vertebrae in the sagittal plane were used as the anatomical landmark for the cropping.

Secondly, the T1 MR images were rigidly registered to the CT images. The transformation matrices used for the rigid registration were in the majority of cases available as part of raw TYKS data. Cases without the availability of the spatial registration file were rigidly registered using the constraint of six degrees of freedom (DOF) when performing the image registration in the 3D Slicer. MR images were resampled into the voxel resolution grid of corresponding CT images. This step was needed for the unification of the spatial resolution between CT and MR images for the further processing and segmentation using the Python programming language. Consequently, the low spatial resolution of the CT resulted in a quality decrease of the resampled MR image.

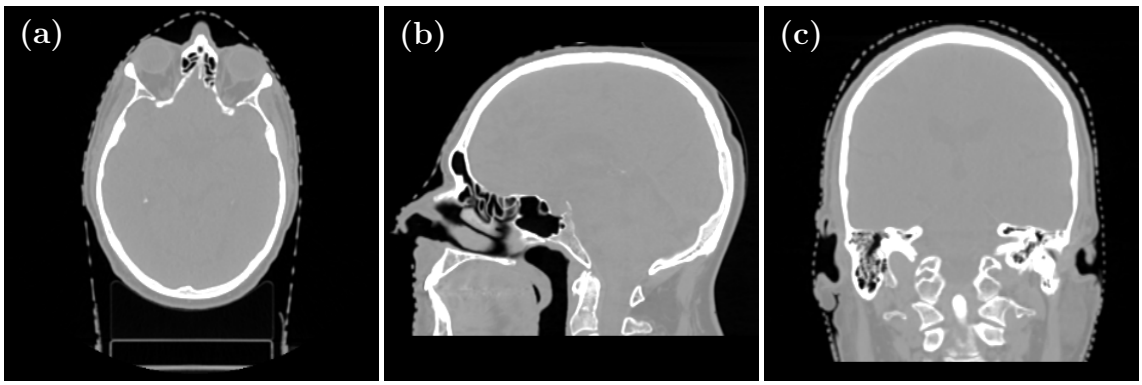

Figure 3.3: Cropped CT image where C2 served as the anatomical landmark. Axial (a), sagittal (b) and coronal view (c).

Finally, the other set of image pairs (CT and T1), with further reduced VOI, was generated for the purpose of bulk tissue HU calculation. The most distal part of the skull was used as the anatomical landmark for image cropping in the axial direction. This landmark was either the base of the occipital bone or the mastoid process depending on the patient positioning. The reason for this step was to reduce the impact of voxels not likely to be within the beam path on the bulk tissue HU estimations. The second reason was to reduce the impact of large metallic artefacts from dental implants shown in figure 3.2b.

3.2 Generation of head volume mask

Generation of a binary mask, covering entire head volume including inner air cavities, was an important step for several reasons. Firstly, the binary mask was used for classification and distinguishing of the inner air within the head volume from the background air. The mask was also used as the template for the further segmentation into single tissue classes. Secondly, the modification of this mask, where inner voxels were replaced by corresponding HU of water and the air HU was assigned to the background served as the reference water-filled fCT (fCTw) in dose comparisons. And finally, the binary head volume determined the VOI from which were calculated all metrics that were used for the evaluation of the segmentation accuracy.

3.2.1 Morphological operations and connected-component labelling

The morphological binary image processing was repeatedly used in several stages of medical image processing employed in this thesis. Binary morphological operations were used for e.g. the thermoplastic mask removal, generation of the head binary mask and calcification detection as well as for automated skull-stripping which was necessary for the brain tissue segmentation. Especially the opening operation, which is simply the erosion followed by dilatation, has frequently been used. The purpose of this section is, therefore, to preclude the repetitiveness in method description in following chapters. It should be noted, that all the presented methods and operations are well applicable in the 3D image processing, however, for simplicity and better understanding are the basic principles demonstrated on simple 2D binary images.

The elementary principle behind the binary morphology is to probe the image with a kernel that has a pre-defined shape. This binary kernel is called the structuring element represented as B in equations (3.2) - (3.4). This structuring element B is primarily drawing conclusions on how this shape misses or fits the shapes in the binary image [71, 72].

Morphological dilatation and erosion In the morphological image processing the binary image is represented as a collection of non-zero points of the plane P. The transformation $X_z = \{y \mid y = x + z, x \in X\}$ defines the translation of the set $X \subset P$ by the vector $z \in P$. The equation (3.1) shows Minkowski addition $X, B \subset P$ which is also known as dilatation [72]. The process of dilatation is shown by figure 3.4.

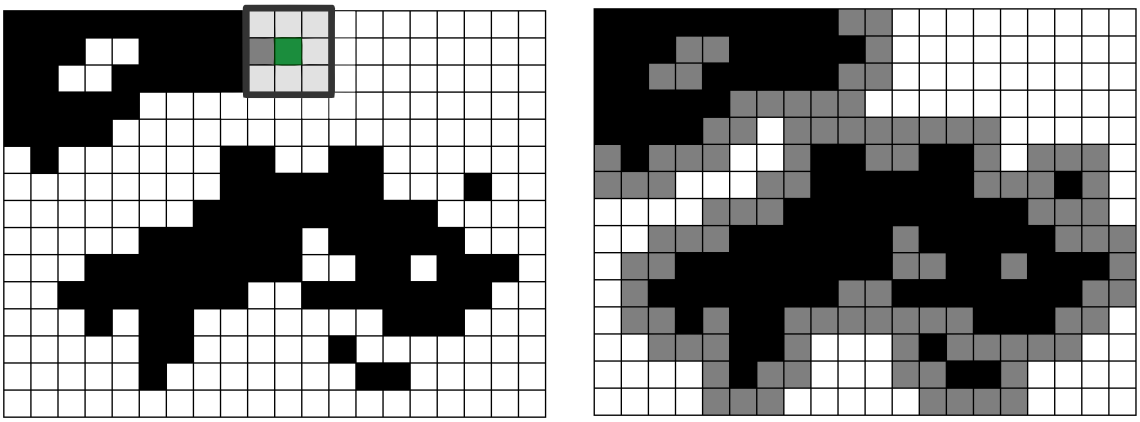

Figure 3.4: Dilatation of 2D binary image with 8-neighbourhood structuring B (left) and eroded image (right) (source: [73]).

$$X \oplus B \quad = \quad \{x + b \mid x \in X, b \in B\} \tag{3.1}$$

figure 3.5 displays the process of morphological erosion, also called the Minkowski subtraction, which is described by equation (3.2) [72].

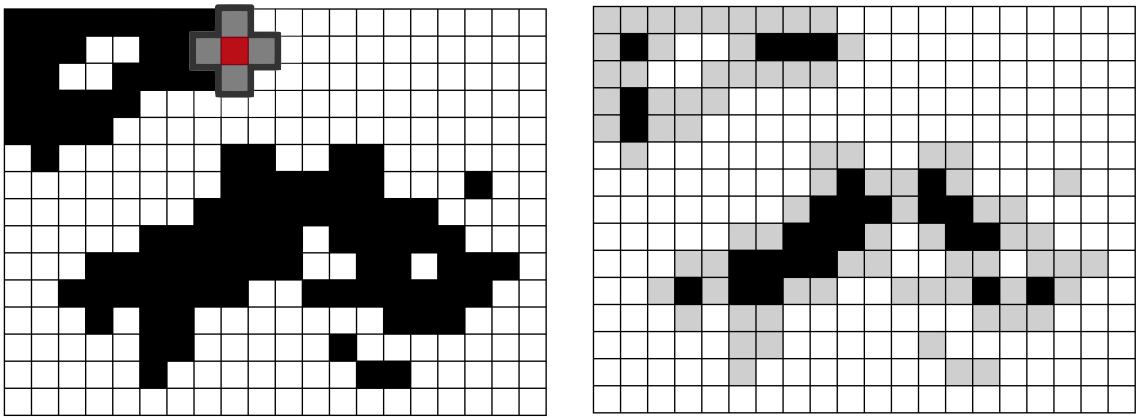

Figure 3.5: Erosion of 2D binary image with 4-neighbourhood structuring B (left) and dilated image (right) (source: [74]).

$$X \ominus B \quad = \quad \{z \in P \mid B_z \subseteq X\} \tag{3.2}$$

Morphological opening and closing Besides the dilatation and the erosion, there are two secondary commonly used morphological operations that are termed as opening and closing. Especially, the opening is handy for an elimination of small image components [71]. The opening is described by equation (3.3) as the erosion followed by dilatation.

$$X \circ B \quad = \quad (X \ominus B) \oplus B \tag{3.3}$$

The closing of the binary image can be written as the erosion that follows after the dilatation in the way as is shown in equation (3.4).

$$X \bullet B \quad = \quad (X \oplus B) \ominus B \tag{3.4}$$

Connected-component labeling The connected-component labelling can be used for the partitioning of the binary image into the disjoint sets (components). This method was used e.g. for the automatic skull stripping, where the brain volume was detected as the largest component of the eroded soft tissue label. The connected filter works in the way of merging the connected components and assigning them new label numbers, colours or different grey levels [72]. The process of the connected-component analysis is displayed by figure 3.6.

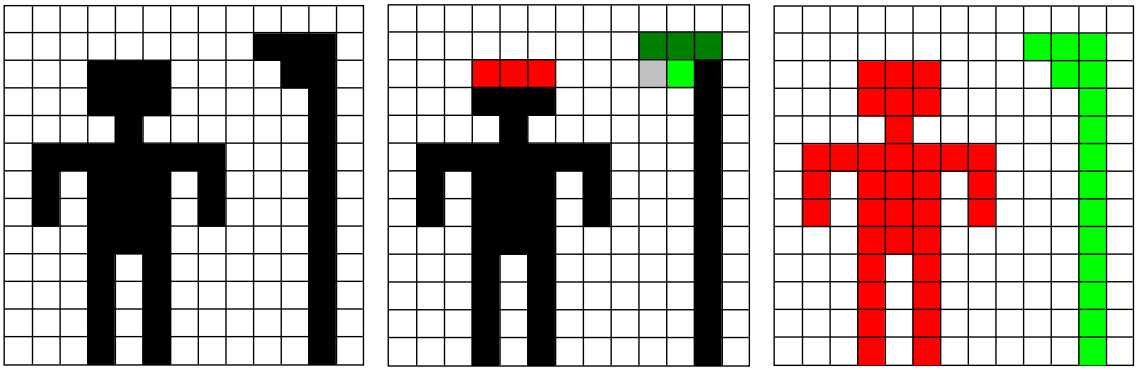

Figure 3.6: Process of connected-component labeling in 2D binary image (source: [75]).

3.2.2 Removal of thermoplastic mask from CT

CT images used for RT planning must be acquired with the patient in the treatment position. Consequently, all CT images contained the fixation and positioning devices such as thermoplastic masks or positioning boxes. Thermoplastic masks are not visible in MRI, and therefore, they need to be removed from the CT image to allow a one-to-one comparison against prospective pCT. Moreover, the presence of such background objects would pose a problem for the generation of the binary head mask.

The thermoplastic mask removal was accomplished via an appropriate combination of fundamental image processing operations. In a first step, the 3D median filtering was applied in the CT image in order to remove noise and decrease the intensity within small components, which belong to the thermoplastic mask, by taking the neighbourhood background air voxels into account. The initial binary head mask was generated by applying a relatively high threshold of $-250\,\mathrm{HU}$, separating the background air voxels from those with higher intensity. A relatively high threshold helped with a further elimination of small elements that were located outside of the head volume.

The conversion into binary image enabled the use of morphological image processing such as the erosion which was applied for further elimination of small islands having a high HU and for generation of disjoint sets that could be easily detected and removed by the connected component labelling. The final step was the application of dilatation with slightly larger structuring element to substitute losses caused by both, the use of high HU threshold (-250 HU), and by the morphological erosion. The final binary mask could be then easily used for the removal of the thermoplastic mask from the CT image as it shown in figure 3.7.

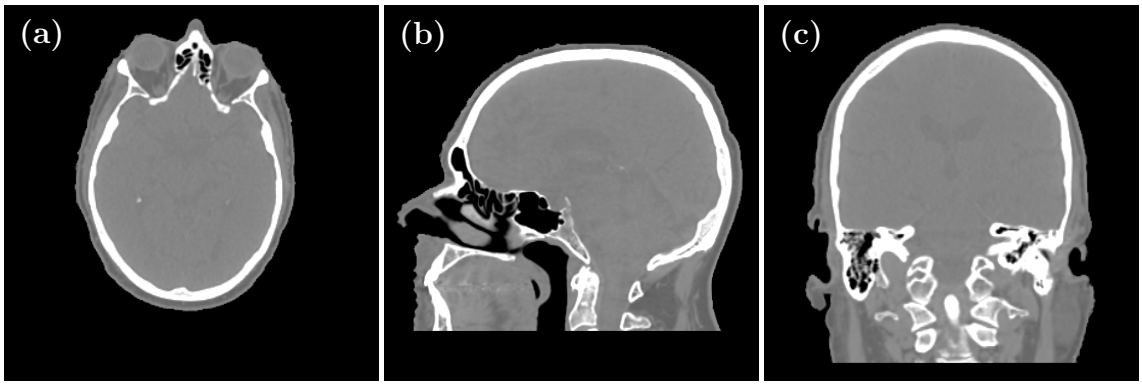

Figure 3.7: CT volume after the thermo-plastic mask has been removed. Axial (a), sagittal (b) and coronal view (c).

3.2.3 Filling of air cavities

The filling of the holes in 3D images comes with special conditions that must be taken into account. This in particular applies to holes that are not fully closed in the three-dimensional space. Good examples of such cases are nasal cavities or external auditory canals. Although these cavities are represented as holes in two-dimensional coronal and sagittal plane, these holes are open in the 3D space or the axial plane. Consequently, the 3D flood filling algorithm fails in the filling of such holes.

Active-contour model The aforementioned problem was solved by the use of an active contour model which is also known as a snake. The snake fulfilled a role of artificial plasters for closing all the opened holes in the axial plane such as mouth cavity, upper airways and external auditory canals.

The goal of active contour model is, in general, to integrate the measurements of local image changes such as edges and lines into the form of contours delineating the entire image objects. It is an energy minimising problem searching for the curve travelling across the image regions with small values of the energy function. The simple snake can be parametrically described as $v(s) = (x(s), y(s))$ and its energy can be then written as it is shown in equation (3.5), where E_{int} is the internal energy of the contour by cause of bending, E_{image} give rise to the image forces and E_{con} represents the external constraint forces. The constraint energy is the optional term that can be used for interactively guiding the snake away or towards to specific features [76].

$$E^*_{snake} = \int_0^1 E_{snake}(\mathbf{v}(s))ds = \int_0^1 E_{int}(\mathbf{v}(s)) + E_{img}(\mathbf{v}(s)) + E_{con}(\mathbf{v}(s))ds \quad (3.5)$$

The internal energy of the snake, which is expressed by equation (3.6) consists of a one first and one second order term. The first order term causes snake behave as a membrane and its weight $\alpha(s)$ controls the relative importance of this behaviour. The second order term, which is controlled by a weight $\beta(s)$, makes the spine act like a thin plate [76]. The role of these weights that are determined by user is to control the amount of stretch and curvature in the snake, and therefore, to rule the level of constraints on the shape of the contour.

$$E_{int} = (\alpha(s) \mid \mathbf{v}_s(s) \mid^2 + \beta(s) \mid \mathbf{v}_{ss}(s) \mid^2)/2 \quad (3.6)$$

Energy of the image shown by equation (3.7) is a weighted combination of three energy terms ($E_{line}, E_{edge}, E_{term}$) where each of them makes the snake attracted to different image features such as lines, edges and termination. Weights ($w_{line}, w_{edge}, w_{term}$) determine the impact of single energy terms on the final energy of the image. In the case of E_{line} the sign of the weight w_{line} makes snake to be attracted either to dark or light lines. The termination energy E_{term} takes advantage of principle that the curvature of level lines in a smoothed image can be used in detection of features like terminations and corners in the image [76].

$$E_{img} = w_{line}E_{line} + w_{edge}E_{edge} + w_{term}E_{term} \quad (3.7)$$

3.2.4 Generation of filled head mask

The only input into the filled head mask generation process was the binary volume without the components of the thermoplastic mask. In a first step, two active contour models were applied in axial slices of the input image by use of the Skimage Python library. These axial slices were slightly smoothed by the utilisation of the Gaussian kernel in order to emphasise gradients around edges.

The reason for the application of two snakes was a requirement on contour to behave like balloon or plaster that would close the nasal and mouth cavities. However, this effect would be not desirable for proper delineation of ear lobes. Consequently, the first snake was used for generation of the anterior mask with weights optimised in a way that made the contour finely delineate the shape of the nose while the balloon effect did not let it proceed to move further inside to cavities. This behaviour is shown in figure 3.8a, where the blue line represents the actual snake, and the red dashed line is the initial contour obtained from dilated version of the binary head mask. The second snake, which was used for generation of the posterior mask, is shown in the figure 3.8b. In this case, all weights were selected to reduce the amount of stretch and curvature in the snake to get rid of inheritance of earlobes from the initial contour. This contour was, in this case, obtained using the image closing operation applied on the binary head mask.

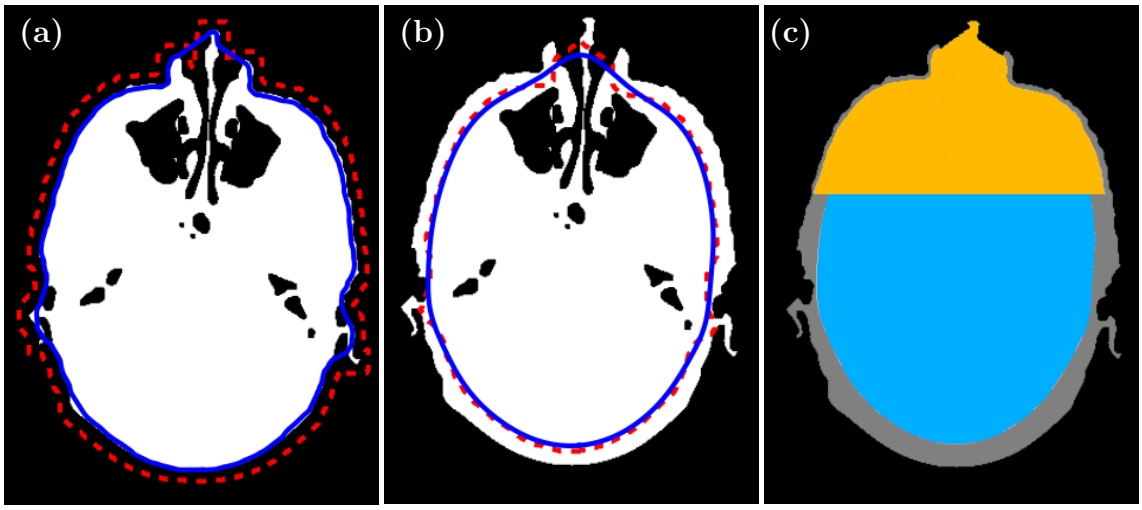

Figure 3.8: Generation of anterior and posterior masks for filling of open air cavities in binary mask obtained from the CT image by use of active contour model. Outer contour for generation of the anterior mask (a). Inner contour for generation of the posterior mask (b). Filling of open air cavities using the generated masks (c)

The iteration number was reduced to 50 in order to shorten the computation time needed for the generation of final contours. Since contours were optimised to delineate only structures that occur in specific locations, the application of snakes was, therefore, reduced into the defined range of axial slices. Moreover, this step further reduced the computation time and more importantly, it decreased the risk of faulty delineations of structures located in more superior and inferior regions.

The readily detectable tip of the nose with a margin of two slices in superior direction was used as the anatomical landmark for termination of anterior mask generation process. In the case of the posterior mask was used the relative range of axial slices that covered the entire ears in all the tested patient cases.

Subfigure 3.8c show the combination of generated masks covering all the open cavities. Since these masks did not cover all closed holes located within the head volume, the 2D flood fill algorithm was applied separately to all the axial slices in order to fill remaining cavities. This step followed by slight dilatation resulted in the final binary head mask.

3.3 Tissue stratification for MR-only RT

The CT tissue stratification was together with the bulk tissue HU estimation necessary steps in the generation of flattened CT (fCT) images. The segmentation was performed using two image modalities, CT and T1 weighted MR images. Hence, two different segmentation methods were selected based on properties of the source image and desired segmentation outputs. The K-means clustering was found suitable for the label generation in the case of tissues with high signal-to-noise ratio (SNR) in CT image. Brain tissue consisting of the cerebrospinal fluid (CSF), white matter (WM) and grey matter (GM) that have all low SNR in the CT were segmented using the

T1 MRI as the source image. The Markov Random Field with Iterated Conditional Modes optimisation (MRF-ICM) algorithm, taking the information from the voxel neighbourhood into account, was employed in this process.

3.3.1 CT image segmentation

All tissue classes with high SNR in CT images, and therefore, with significantly different HU values were segmented by use of the K-means clustering. These tissues were fat, water-rich tissue, bone marrow and compact bone. The label for air cavities was acquired from the intensity thresholding with a threshold of $-500\,\mathrm{HU}$. This threshold was carefully selected based on reports in literature [77] and partly from the testing upon the segmentation process. The main goal was to mitigate the impact of strong partial volume effects at the interface between the air and tissue classes on the estimation of bulk tissue HU values. The K-means CT segmentation, therefore, covered only voxels located within the head mask excluding all voxels belonging to air class.

K-means segmentation K-means clustering belongs to a group of partitioning clustering methods. The main goal of K-means clustering is to divide input data points $X = \{x_1, ..., x_N\}$ into K clusters by minimising the following objective function:

$$J_{KM} = \sum_{n=1}^{N} \sum_{k=1}^{K} \|x_n - c_k\|^2 , \tag{3.8}$$

where $\|x_n - c_k\|^2$ is a chosen distance measure between data point x_n and cluster centre c_k. The variable N_k denotes the number of data points in corresponding cluster C_k [78]. An overview of K-means clustering is shown in figure 3.9.

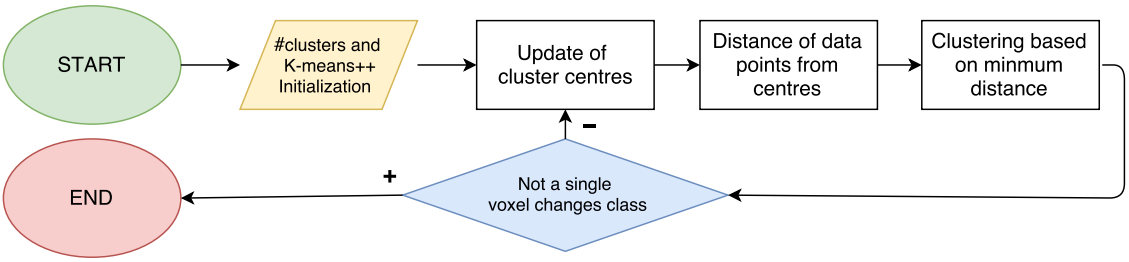

Figure 3.9: Diagram showing the principle of K-means clustering algorithm

Each voxel is in the K-means based image segmentation characterised by a feature vector. This vector consists of one or more components, where each of these components represents one feature employed in the clustering process. These feature vectors are formed into the input matrix X with a dimension of $M \times N$, where M denotes the number of features.

In the present study, feature vectors including two components were defined for the purpose of the CT segmentation. The first component was the original voxel

intensity in HU units. The second feature was median intensity obtained from the 3D kernel surrounding the voxel for taking the information from the voxel neighbourhood into account. The other reason for using this feature configuration was the existence of literature records showing that 2D K-means clustering using two features provided better bone segmentation outcomes than in comparison with other clustering methods such as Fuzzy C-Means and 1D K-means clustering with the one image intensity feature [79]. The kernel size used for the median image filtering varied based on slice thickness of the CT image. This kernel size was calculated based on the resolution of the CT image input. The kernel approximating the ball or ellipsoidal shape with a radius of 2 voxels in all three image planes was used in the case of CT images with the slice thickness of 1 mm. In the case of slice thickness of e.g. 2 mm, kernel radius of 1 voxel in the anterior-inferior direction was employed. The generation of the median filtered image was accomplished by use of the SimpleITK library in Python. An example of CT images that served as features is shown by figure 3.10.

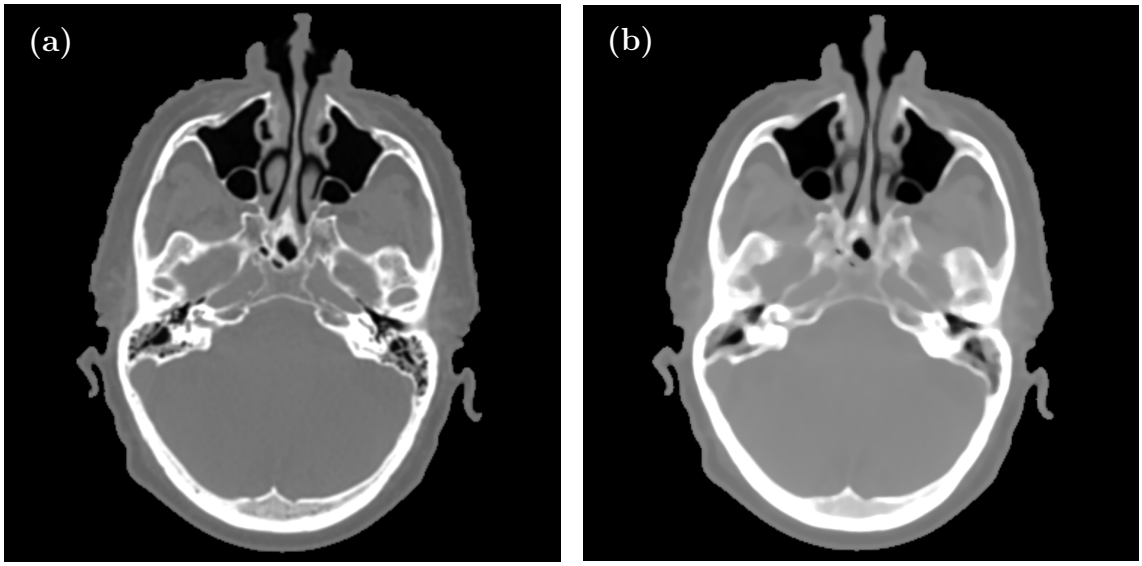

Figure 3.10: CT images used as features for two-dimensional K-means segmentation. The left image is the original CT (a) with cleaned background, and the right image is the median-filtered CT (b) using the kernel radius of 2 voxels.

The Scikit-learn Python clustering library was employed in the execution of the 2D K-means segmentation. The K-means++ method was used for the smart selection of the initial cluster centres. This method tries to initialise centroids in a way that they are far apart from each other using probability measures [80]. The final tissue class label numbering was determined based on increasing order of mean HU values within the clusters. The connected component labelling was employed in the separation of calcifications and foreign objects from the bone labels.

Number of clusters In total, six clusters were used for the clustering where water-rich tissue and fat were each represented by one cluster and spongy and compact bone classes were each covered by two clusters. In this thesis, the terms of spongy and

compact bone refer rather to bone compartments having a low and high density in CT than to the anatomical structure of bone tissue. The presented cluster configuration was selected based on intensity histogram of head CT image, where bones expressed high variance of HU values without visible distributions in comparison with water-rich tissue and fat classes where distribution peaks were clearly detectable. Moreover, the silhouette coefficient was calculated in order to verify that data points lie well in their clusters, where the silhouette coefficient is defined as

$$\bar{s} = \frac{1}{N}\sum_{i=1}^{N}\frac{b(i)-a(i))}{max\left\{a(i),b(i)\right\}}, \tag{3.9}$$

where variables $a(i)$ and $b(i)$ denote the intra-cluster distance and the mean nearest-cluster distance for each data point [81].

3.3.2 MR image segmentation

The precise soft tissue contrast in MRI images allows relatively easy, reliable and fast segmentation of soft tissue classes such as fat, CSF, the white, and grey matter, that might have some effects on the dose performance of the prospective pCT. However, noise and low, spatially non-consistent MR signal intensity within tissue classes are leading causes of the decrease of K-means classification accuracy. Thus, there was raised a need for more advanced segmentation algorithm taking the voxel neighbourhood information into account.

T1 MRI pre-processing T1 MRI images were selected as an input for the brain tissue stratification. This process required the execution of a skull stripping on the MR image. This process was accomplished by applying the image opening together with connected component labelling within the binary tissue label. This label was taken from the 2D K-means segmentation of the coregistered CT image. The result of skull stripping is shown in figure 3.11.

Figure 3.11: The process of skull stripping by applying the morphological opening and connected component labelling on binary tissue label taken from the CT image segmentation (a). The generated brain label overlaid on the T1 MRI (b) and 3D visualisation of the brain mask (c).

The potential signal inhomogeneity in T1 MR images was corrected by use *N4ITK Bias Field Correction* module implemented in 3D Slicer that performs image bias correction with the N4 algorithm [82]. The contrast inconsistencies among T1 images, introduced mostly by the use of contrast agents, were further resolved by thresholding out the intensity outliers. This step was followed by intensity normalisation applied within the brain tissue label.

MRF-ICM algorithm The use of Markov random field covers issues that are of particular importance in the MR image segmentation. Such issues are e.g. the neighbourhood correlations and spatial inhomogeneities in MR signal [83]. The base of ICM algorithm lies in minimising the following energy function:

$$f_{ij}(w) = \frac{1}{2}\left(\frac{x_{ij}-\mu_w}{\delta_w}\right)^2 - \beta u_{ij}(w) + ln\delta_w, \tag{3.10}$$

where the potential β is a weighting factor. This factor estimates how much is the final segmentation influenced by neighbourhood $u_{ij}(w)$ of the voxel x_{ij}. The number of neighbourhood voxels classified into same tissue class w is acquired from the Gaussian mixture model (GMM) simulated by convolution between tissue labels and 3D kernel. This kernel covers the selected voxel connected neighbourhood.

The energy value is computed point-wise, and new labels are generated to classify voxels into the class corresponding to the smaller energy value. Means μ, standard deviations δ and neighbours $u_{ij}(w)$ are updated at each iteration based on new classification obtained from minimising the energy function. The classification process is repeated. The initial image segmentation is usually generated by use of the K-means clustering, and the MRF-ICM process ends when no single voxel changes are detected or when the predefined number of iterations is reached. The process of MRF-ICM segmentation is depicted in the figure 3.12.

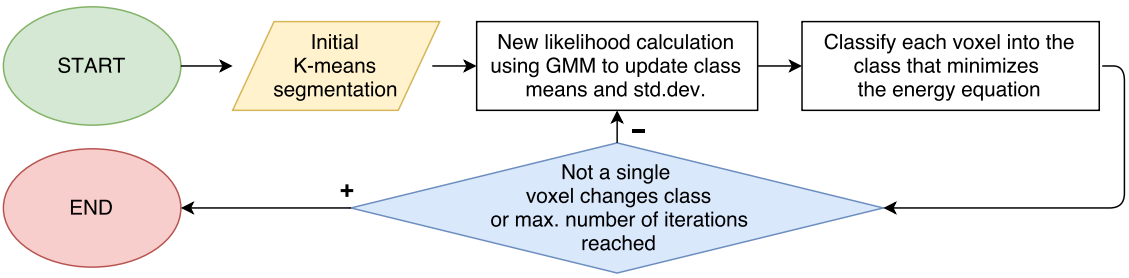

Figure 3.12: Diagram showing the principle of MRF-ICM segmentation algorithm.

In this study, the initial neighbourhood information was generated from 3D convolution between tissue labels extracted from the K-means segmentation within the brain mask and 3D kernel covering the 18 voxels connected neighbourhood. The ICM optimisation was terminated when single voxel did not change a tissue class between individual iterations or when five iterations have been completed. This limit for iteration count was used in order to further shorten the computation time and

to prevent the algorithm from exaggerative smoothing of brain tissue labels caused principally by the low contrast in some of the T1 images. The MRF-ICM algorithm used in this study was implemented through coding in Python.

3.3.3 Bulk tissue HU estimation

A determination of bulk HU values is the input needed for the pseudo-CT (pCT) generation using one of the voxel-based methods. The estimation of bulk HU values was, therefore, the essential step in the production of flattened CT (fCT) images.

Bulk HU values were estimated as averages from corresponding tissue binary labels within CT images. Mean HU values were initially calculated for each of 10 selected CT images separately. The final bulk CT number was determined as the average of these estimates. This strategy further guaranteed the equal contribution of each of selected CT images into the final results despite variation in the spatial resolution. Since the brain tissue labels were generated from the MR image, the registration error might have been responsible for uncertainties in the label positioning when labels were overlaid on the CT image. This positioning error would certainly cause discrepancies in bulk tissue HU estimation.

Furthermore, the fundamental property of CT image such low SNR in soft tissue regions and high partial volume effects might influence the bulk HU estimation as well. The impact of all these undesirable effects was, therefore, reduced by application of the morphological erosion on tissue labels. In the case of CSF was the erosion complemented with use of the connected component labelling. Hence, the average CT number for CSF was estimated only from eroded ventricles. Modified brain tissue labels are shown in figure 3.13. The HU value for air was calculated as the average of all the image voxels (including background) with the intensity lower than $-500\,\mathrm{HU}$.

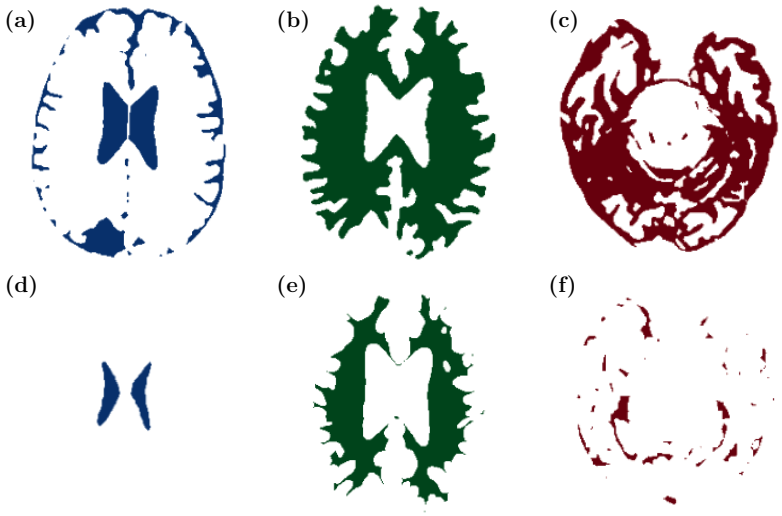

Figure 3.13: Original and eroded brain tissue labels issued for the bulk HU estimation. CSF label (a), WM label (b), GM label (c) and corresponding eroded labels (d-f).

3.3.4 Flattened CT images

The final head tissue stratification was generated through the fusion of the MRI-based MRF-ICM brain tissue segmentation with the 2D K-Means segmentation of the CT image. Such 3D array containing all the labels then served as the template for the generation of all versions of flattened CT (fCT). In total seven fCT configurations were generated by filling of the tissue labels with corresponding bulk HU values. The fCT naming convention was for simplicity determined as fCTx. The number x represents the count of tissue classes encompassed in the corresponding fCT configuration.

The simplest fCT2 version included only the bone and average tissue HU values assigned to the corresponding tissue labels. The bulk HU calculated from the soft tissue label was, therefore, in the case of fCT2 assigned to the air cavities as well. The most detailed configuration named fCT8 then encompassed eight bulk HU values for the inner air, fat, soft (water-rich) tissue, spongy bone, compact bone, CSF, WM and GM. The calcification label was filled with soft tissue HU value of the corresponding fCT version. The fCTw with HU value of water (0) assigned to entire head volume was generated as a reference image for dose comparisons. The following seven fCT configurations were generated: fCTw, fCT2, fCT3, fCT4, fCT5, fCT7 and fCT8.

The final step in fCT generation was the conversion of the 3D image arrays into the DICOM format. This action required the generation of artificial DICOM tags that are part of metadata attached to the medical image. This metadata is needed for making the generated fCT images readable by TPS or other clinical applications. Table 3.1 shows summary of generated fCT images.

Table 3.1: An overview of generated fCT images and the tissues included in each version

	fCTw	**fCT2**	**fCT3**	**fCT4**	**fCT5**	**fCT7**	**fCT8**
Water	✔	-	-	-	-	-	-
Air cavities	-	-	✔	✔	✔	✔	✔
Fat	-	-	-	✔	✔	✔	✔
Tissue	-	✔	✔	✔	✔	✔	✔
Bone	-	✔	✔	✔	-	✔	-
Spongy bone	-	-	-	-	✔	-	✔
Compact bone	-	-	-	-	✔	-	✔
CSF	-	-	-	-	-	✔	✔
White matter	-	-	-	-	-	✔	✔
Grey matter	-	-	-	-	-	✔	✔

3.4 Generation and processing of RT plans

All the RT plans included in this work were created in Pinnacle 16 (Philips, Netherlands) treatment planning system (TPS). Two groups of RT plans were generated. The first group comprises of a large number of simplified plans used for PTV position dose analysis. The second group encompassed so-called technical approximations of clinical plans generated in Pinnacle TPS based on real clinical data. These plans served as verification for whether the outcomes of the PTV position analysis are valid also for RT plans that are similar to those employed in clinical practice.

3.4.1 PTV position analysis

Brain tumours vary greatly in position, size, and shape. Especially the position may be of particular importance regarding dosimetric properties. The hypothesis was such that medially located PTV surrounded by water-rich tissue may have different requirements on the accuracy of fCT tissue stratification in comparison with PTV located more laterally in the proximity or directly covering the skull.

The use of multiple RT plans with PTV positions distributed in a manner that the entire brain volume is covered appears to be a good way of investigating dosimetric properties of all of the generated fCT versions. The PTV dose position analysis presented in this thesis was carried out on a cohort of 10 patients. In total six PTV positions and corresponding RT plans were generated for each of the patients. These CT-based plans were then simulated on all seven fCT configurations. This analysis, therefore, encompassed 480 RT plans.

PTV parameters and positions The first stage of the PTV position dose analysis was to determine the shape and size of the PTV, whereupon the spherical PTV with a diameter of 4 cm was selected. The primary reason for this selection was a good comparability and simple reproducibility of PTV contours. Moreover, a similar approach using spherical PTV with diameters ranging between 2 and 7 cm was reported in literature [1, 61, 64, 84, 85].

These spherical PTV contours were placed in six positions covering the entire cerebrum and cerebellum. The first PTV (annotated as SC) was placed superiorly in the brain centre between the two hemispheres. PTVs were further positioned anteriorly (A) within the frontal lobe, and posteriorly (P) partly including both parietal and occipital lobes. Next two PTVs were placed contralaterally towards the left (L) and right (R) roughly covering the temporal lobes. Since the head symmetry might be a potential cause of duplicates in results, the PTV R was moved more laterally to partially cover the skull. The last sixth PTV was positioned in the cerebellum (CR). Figure 3.14 shows all the PTV positions and the selected naming convention.

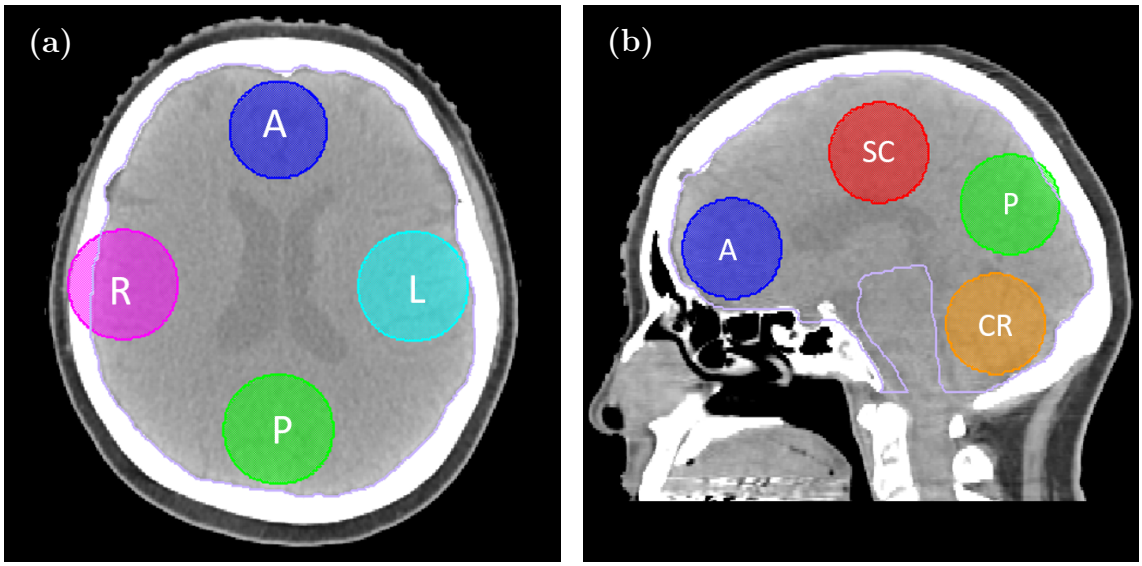

Figure 3.14: Distribution of six spherical PTV with diameter of 4 cm throughout the brain. Displayed are the superior-central (SC) - red , anterior (A) - blue, posterior (P) - green, left (L) - cyan, right (R) - magenta and cerebellar (CR) - orange PTVs.

RT planning process The RT planning process started with the selection of the primary CT image, which was used for dose calculations. For the purpose of the PTV position analysis, a modified version of the CT images was used. Here, calcifications were replaced by the average HU value of soft tissue, and all voxels that were exceeding HU value of 2000 were filled with mean compact bone value (see table 4.1). The thermoplastic mask (TM) was removed as well. This modification was carried out to ensure that only the tissue detectable by MR imaging and/or pCT generation algorithm had an impact on dose comparisons. The CT-density table was obtained from TYKS, and electron densities listed in this table were converted into the mass density required by the Pinnacle.

The LINAC parameters that correspond to the Novalis Tx (Varian Medical Systems, USA) machine equipped with the HD-MLC were selected for the RT planning process as the use of this LINAC was detected in the majority of TYKS RT plans. This LINAC is designated for delivery of highly focused SRT/SRS treatments. The HD-MLC is folded from 60 leaf-pairs where leaves located in the central part of MLC have a width of 2.5 mm while those located at the edges have a width of 5 mm.

Two VMAT arcs with isocenter located in the centre of the spherical PTV were used. The first coplanar arc had a full arc of 360° and was parallel to the axial plane. The second 180° arc was perpendicular to the axial plane, and the MLC field was, in this case, rotated over the 45° in order to further improve the MLC shaping around the PTV. The primary aim of employing the second arc was to enable very steep dose gradients surrounding the PTV.

A fine control point (gantry) spacing of 2° was selected in order to reduce small but conspicuous interpolation errors that can occur when a gantry spacing of e.g. 4° is applied [32]. The spatial resolution of the 3D dose grid, which is employed in

dose calculations was selected to be 2 mm in all three coordinates. A similar dose grid resolution has been previously reported in literature for brain and head&neck RT planning [32, 86]. Moreover, this resolution was observed in the majority of the IMRT plans and some of the VMAT plans that were obtained from TYKS.

Two additional RT contours were automatically generated for each of the PTV positions in order to better guide the dose optimiser to the desired dose gradients. These structures were generated by use of scripting in Pinnacle. The first structure covering the entire head volume excluding the PTV + 0.5 cm margin served as an avoidance structure (see 3.15a). The second contour was a RING or sphere covering 2 cm margin directly around the PTV (normal tissue), which was used as simplified OAR in subsequent DVH analysis (see 3.15b). Examples of these RT structures and arrangement of dynamic VMAT arcs are shown in figure 3.15.

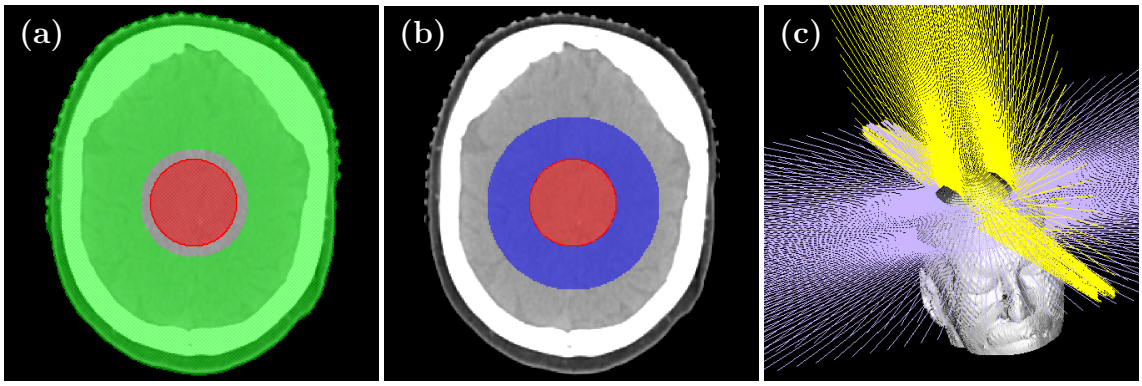

Figure 3.15: Avoidance structure - green and PTV (red) (a). RING/sphere (blue) that covers healthy tissue around PTV (red) (b). An arrangement of dynamic arcs in the simplified RT plan (c). Full arc (levender) and perpendicular half arc (yellow).

Optimisation objectives All generated plans were optimised using the auto-planning feature in Pinnacle [87]. The direct machine parameter optimisation (DMPO) algorithm [88] was employed in this auto-planning process. The PTV position analysis included a generation of six reference CT-based VMAT RT plans for each of the 10 patients (total 60 plans). Optimisation objectives, therefore, had to be selected carefully in order to obtain well-optimised plans from the single auto-planning trial. This condition was fulfilled through the selection of appropriate LINAC, arc arrangement and especially by estimation of objectives such as dose prescriptions and constraints.

The prescribed dose was selected to be 60 Gy divided into 30 fractions (2 Gy per fraction) delivered to the PTV. This prescription roughly corresponds to the one, which is clinically used in high-grade glioma RT treatment [41, 89]. The maximum dose constraint that was assigned to the avoidance structure was determined as 10% of the prescribed dose. Even though this objective was not fully achievable, this very strict dose constraint forced the optimiser to produce an RT plan with PTV conformally covered by the 95% dose isosurface while having very steep dose gradients adjoining the PTV.

3.4.2 Technical approximation of clinical RT plans

Since the original RT plans from TYKS were generated using Varian Eclipse TPS, and as Pinnacle does not allow the import of RT plans stored in DICOM format, the RT plans could not be transferred into the Pinnacle TPS. A generation of so-called technical approximations of the RT plans was therefore needed.

Clinical RT plans RT plan set including five IMRT (step-and-shoot) and five VMAT clinical plans were selected from TYKS data. IMRT plans included either single PTV or two PTVs. The simultaneous integrated boost (SIB) [90] with two dose prescriptions was used in the case IMRT plans with two PTVs. Table 3.2 shows an overview of selected cases and information relevant to the RT simulation process.

Table 3.2: An overview of the 10 patient cases selected for generation of technical approximations of RT plans.

Case#	Tumour	VMAT/SRT	IMRT	Surgery	SIB	fixation
01	secondary	✔	-	-	-	TM
02	secondary	✔	-	-	-	TM
03	secondary	✔	-	-	-	TM
04	primary	-	✔	✔	-	TM
17	primary	-	✔	✔	✔	TM
25	primary	-	✔	✔	✔	TM
28	primary	-	✔	✔	✔	TM
30	primary	✔	-	✔	-	SRT-TM
38	primary	-	✔	✔	-	TM
52	primary	✔	-	✔	-	SRT-TM

RT planning process CT images with removed TM were here used as primary images in the RT planning process. No further modifications were applied to these CT images. LINAC parameters, gantry spacing, and CT-density table were selected as identical to those employed in the PTV position dose analysis described above. The spatial resolution of isotropic dose grid voxels was selected to be 2 mm for IMRT and 1 mm in the case of VMAT plans. This selection was in agreement with original clinical RT plan parameters apart from few exceptions.

Clinical RT structures stored in DICOM format were imported into the RT plan in the TPS. In addition to PTV and OAR delineations, GTV, CTV, isodoses and other auxiliary structures were usually available in each of the RT structure sets. Figure 3.16, therefore, shows examples including only a tiny fraction of contours, which were involved in the RT simulation process. The presence of auxiliary structures (layers) within the PTV was unique to the VMAT plans. These structures were used for further dose escalation within the PTV in order to get as steep gradients around the PTV as possible according to discussion with the TYKS oncologist.

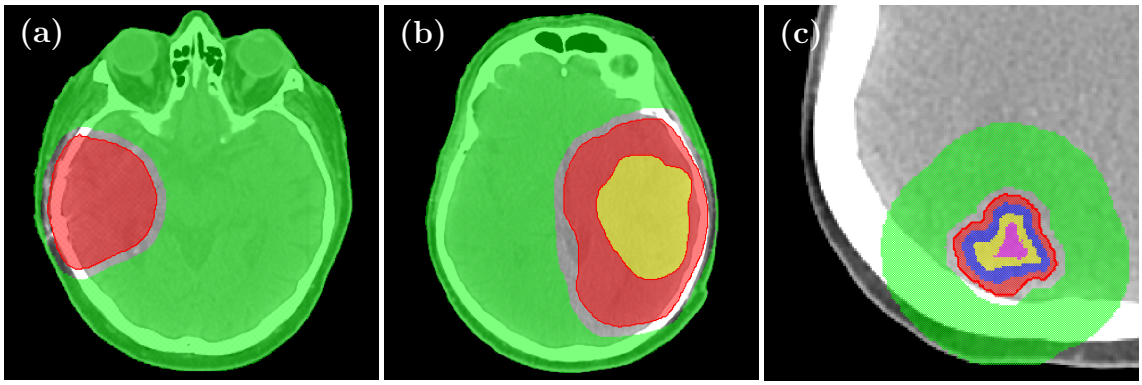

Figure 3.16: Examples of essential RT contours extracted from clinical data. RINGs and normal tissue usually used as avoidance regions are displayed as green areas. Contours for IMRT plan with single PTV (red) (a) and IMRT plan with simultaneous integrated boost (SIB) into the second PTV (yellow) (b). Contours for VMAT plan with one PTV (red) and auxiliary structures used for further dose escalation are displayed within the PTV (c).

The beam or arc geometry and isocentres were imported into the TPS using Pinnacle scripts. These scripts were generated by other script implemented in MATLAB (Mathworks, USA) that was developed and kindly provided by Gregory Bolard from Clinique de Genolier (Switzerland). The RT plan saved in DICOM format was the only input required. Since this script was originally compatible with VMAT RT plans only, a slight modification had to be applied in order to enable import of IMRT beams into RT plans in Pinnacle. Both, coplanar and non-coplanar arrangements of beams or arcs were used in selected RT plans.

Optimisation objectives The major challenge in the generation of clinical RT plan approximations was the optimisation process as information about original planning objectives was not included in the original datasets. These objectives, therefore, had to be estimated from the clinical dose distributions. This was accomplished through calculation of label statistics, in a similar manner as done previously in the case of bulk HU estimation as described in subsection 3.3.3. The main difference was that instead of using a CT image, the dose distribution volume was used where the voxel intensity was given in Gy. Labels were generated from delineations of target volumes, auxiliary structures and avoidance regions.

Dose calculation grid resolution defined the spatial resolution of the 3D dose distribution. The mean dose values from PTV labels in the case of IMRT plans and from labels of auxiliary structures in case of VMAT plans were then used as dose prescription objectives in the TPS. Dose constraints were estimated based on maximum and mean doses, which were calculated from avoidance regions and RING labels. Dose recommendations listed in table 2.1 were taken into account in the RT planning process as well. The auto-planning process using the DMPO algorithm [91] was employed in the RT plan optimisation process, similarly as done for the PTV position dose analysis. The auto-planning usually resulted in sufficiently optimised

VMAT RT plans on the first run, while several subsequent optimisation steps were typically needed in case of IMRT plans in order to approximate PTV coverage by 95% isodose surface.

3.4.3 RT plan simulation on fCT images

RT plan recalculation Both simplified RT plans with spherical PTV and technical approximation of clinical RT plans were simulated on all seven versions of the generated fCT volumes listed in table 3.1. The plan simulation was done by copying the optimised RT plan to the fCT image for dose calculation. Since the fCT image in this evaluation is merely a segmented version of the CT image, there is no need for image registration. All planning parameters and optimised objectives, therefore, remained identical when one compared them to those of the reference CT-based RT plan. Plan recalculation was accomplished using the Adaptive convolution superposition algorithm [91] and the recalculation resulted in a new dose distribution volume reflecting the intensity parameters of the fCT image.

Automated RT plan simulation The dose analysis presented in this thesis required 490 RT plan simulations on fCT images. The analysis of such an amount of plans was made viable only by implementing an automated RT plan recalculation workflow. This automated workflow was implemented by Unix shell scripting that is capable of running the Pinnacle TPS. The Pinnacle scripting was responsible for an execution of the RT plan recalculations and subsequent planning data export. Multiple DICOM server connections were established for the purpose of automated data export from the Pinnacle virtual machine running on Solaris OS and also for the subsequent data sorting in destination directories on the physical workstation running the Microsoft Windows 10 OS. Diagram 3.17 shows the core principle of the automated RT plan simulation workflow.

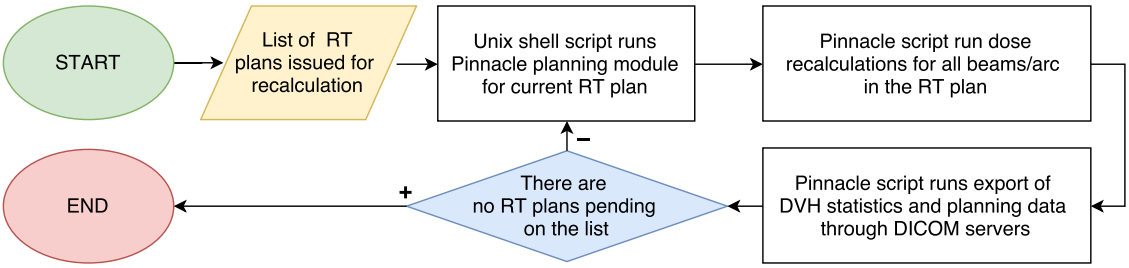

Figure 3.17: Diagram showing the principle of automated RT plan simulation on fCT images and planning data export for further analysis.

3.5 Data evaluation methods

The evaluation methods employed in this thesis can be divided into two groups. The first group consists of measures used for image quality assessment of the generated fCT images. The second method group is dedicated to the RT planning quality assurance and primarily to dose comparison methods.

3.5.1 Image quality evaluation

The error between CT and fCT images can be quantified through a voxelwise comparison and summarised as for example the mean error (ME) or mean absolute error (MAE) usually calculated within the entire FOV [48]. However, these metrics tend to be lowered with increasing number of voxels filled with HU values corresponding with those of water or air [43]. Abundant and from the analysis point of view uninteresting background air voxels would, therefore, have a large impact on estimation of mean errors. Consequently, all the mean errors were calculated only for those voxels located within the patient volume. The binary head volume mask (see subsection 3.2.4) was utilised in the calculation of average errors. Moreover, all the outlier voxels (e.g. clips, calcification) were excluded from the error calculations. Mathematical formulations for ME and MAE are

$$ME = \frac{1}{N}\sum_{i=1}^{n} fCT_i - CT_i, \tag{3.11}$$

$$MAE = \frac{1}{N}\sum_{i=1}^{n} |fCT_i - CT_i|, \tag{3.12}$$

where CT_i is i_{th} CT (reference) voxel and fCT_i is i_{th} fCT (comparison) voxel used for the error estimation. Number N defines a number of voxels allocated inside of the patient head volume with reduced FOV in order to exclude the neck region. ME and MAE were individually estimated for all the fCTx-CT pairs of 10 patient cases which were also used for purposes of bulk HU estimation and PTV position dose analysis. The final mean errors were calculated for all the fCT versions from the individual ME and MAE estimates. MAE and ME from the single tissue labels were estimated in the same manner.

3.5.2 Dose comparisons

All the methods and metrics used in dose comparisons were handling the CT-based dose calculation data as a reference, and the fCT-based dose recalculations were handled as a comparison datasets. Dose comparisons were carried out for all the fCTx-CT pairs using the outcomes from both PTV Position and technical approximation of clinical RT plans as input data.

DVH analysis DVH graphs and statistics were estimated from PTVs and selected OARs or RINGs covering the normal tissue in the case of PTV position analysis. The composition of OARs varied case by case depending on availability of RT contours and dose distribution coverage. The list of evaluated OARs corresponded with the one from table 2.1. DVH statistics from a single PTV were evaluated in case of the simplified VMAT RT plans (PTV position analysis) and basic IMRT RT plans. In the event of clinical approximations of VMAT and IMRT-SIB RT plans, there were always two PTV contours (PTV 1 and PTV 2) included in the DVH analysis. The

PTV 2 contour was already present in the original IMRT-SIB TYKS data. However, the PTV 2 was in the case of VMAT RT plans generated from the auxiliary structure which was in the clinical 3D dose distribution roughly covered by 95% isodose surface. The role of PTV 2 was to capture dose escalations within the entire PTV volume ($PTV1 + PTV2$). DVH statistics including D_{mean}, $D_{2\%}$, $D_{50\%}$, $D_{95\%}$, $D_{98\%}$ and $V_{95\%}$ were calculated from the PTV region. The ICRU conformity index (CI) was further estimated for the simplified VMAT plans, where the CI is defined as

$$CI = \frac{TV}{PTV}, \tag{3.13}$$

where the treated volume (TV) was estimated to be the 95% isodose volume $V_{95\%}$. The TV was calculated as the sum of V_{95} obtained from both, the PTV and the RING. Percentual differences of selected DVH statistics and CI between CT and fCT images were calculated for the purpose of dose comparisons.

Gamma analysis The 3D gamma analysis was performed in this study using a 1%/1 mm passing criterion. The implementation of the fast gamma analysis algorithm, earlier described by M. Wendling, et. al (2007), was employed in our analysis [92]. This implementation used the global normalisation to the maximum dose distribution point for the evaluation of ΔD criterion.

The dose distribution voxel percentage to pass the gamma criterion was determined to be 99%. The gamma statistics was calculated from the 75% isodose volume covering high dose regions including the PTV and surroundings. Hence, a decision whether the case passes the gamma criterion or not was made based on data from this isodose volume.

Gamma and dose 3D distributions were generated from the entire patient volume in order to get visual information from the less clinically relevant low dose regions as well. The gamma analysis was selected because it allows for an objective passing criteria which is convenient for evaluations. However, as there was no registration misalignment between CT and fCT images, the DTA criterion might, therefore, be of a lower significance. Hence, 3D dose difference maps (CT - fCT) were generated in addition to the gamma distributions.

4 Results

4.1 Head volume mask

The initial step in generating a binary mask of the head was the removal of the thermoplastic mask (TM). The TM removal was carried out using the combination of intensity thresholding (−250 HU), connected component labelling and morphological operations. The concept and an example of the result of this process are shown in figure 4.1.

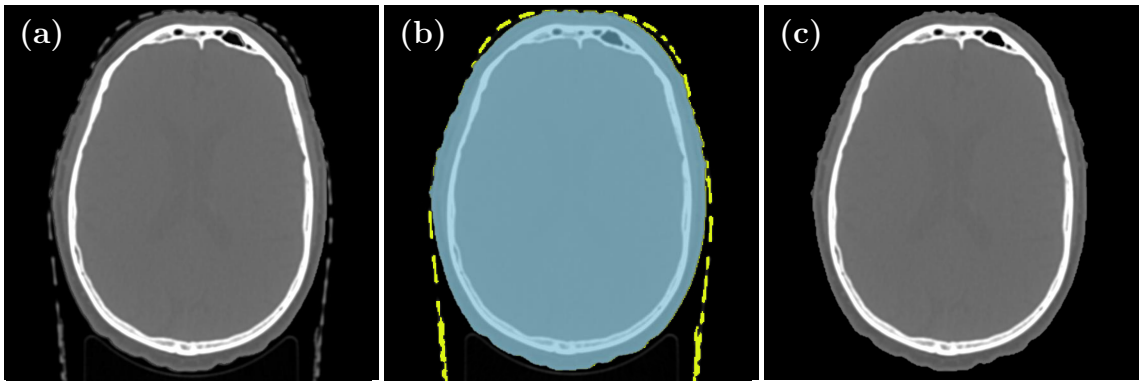

Figure 4.1: Removal of the thermoplastic mask (TM) from the CT image. Original CT (a), identification of the patient volume and the TM components (b). Modified CT after the TM component has been removed (c).

Holes inside of the binary mask were then filled using the anterior and posterior masks generated through the active contour model. Any remaining holes were filled using the 2D floodfill algorithm as described in subsection 3.2.4. An example of filled binary head mask is shown in figure 4.2.

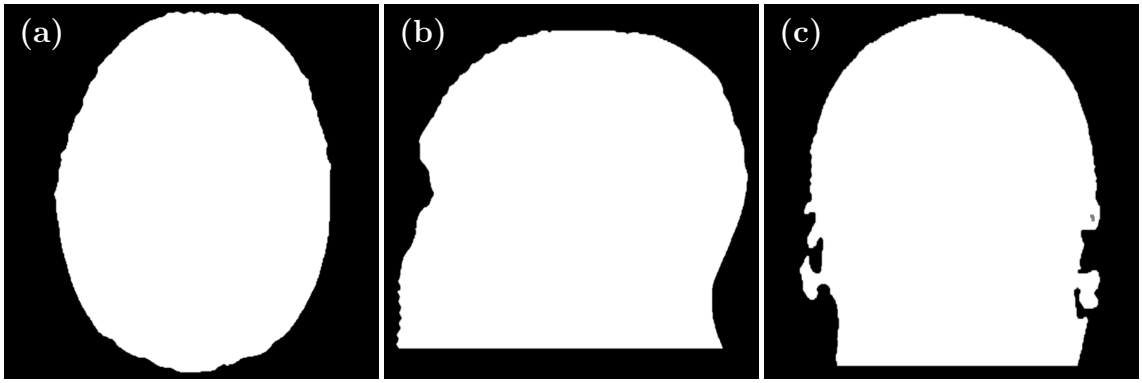

Figure 4.2: Binary volume mask of the head. Axial (a), sagittal (b) and coronal view (c).

4.2 Tissue stratification for MR-only RT

4.2.1 CT image segmentation

2D K-means clustering was employed in the tissue segmentation from CT images using all the voxels with intensity higher than −500 HU that were located within the head mask. This clustering method used six classes where the two soft tissue compartments (fat, water-rich tissue) were represented by one class each, and two bone compartments were each divided into two classes. The silhouette coefficient of 0.64 (see equation 3.9) for this classification setup indicated good allocation of classes among the voxel intensity distribution. The CT segmentation result displaying all segmented tissue labels is shown in figure 4.3. A calcification label can also be seen which was separated from the bone class by use of connected component labelling.

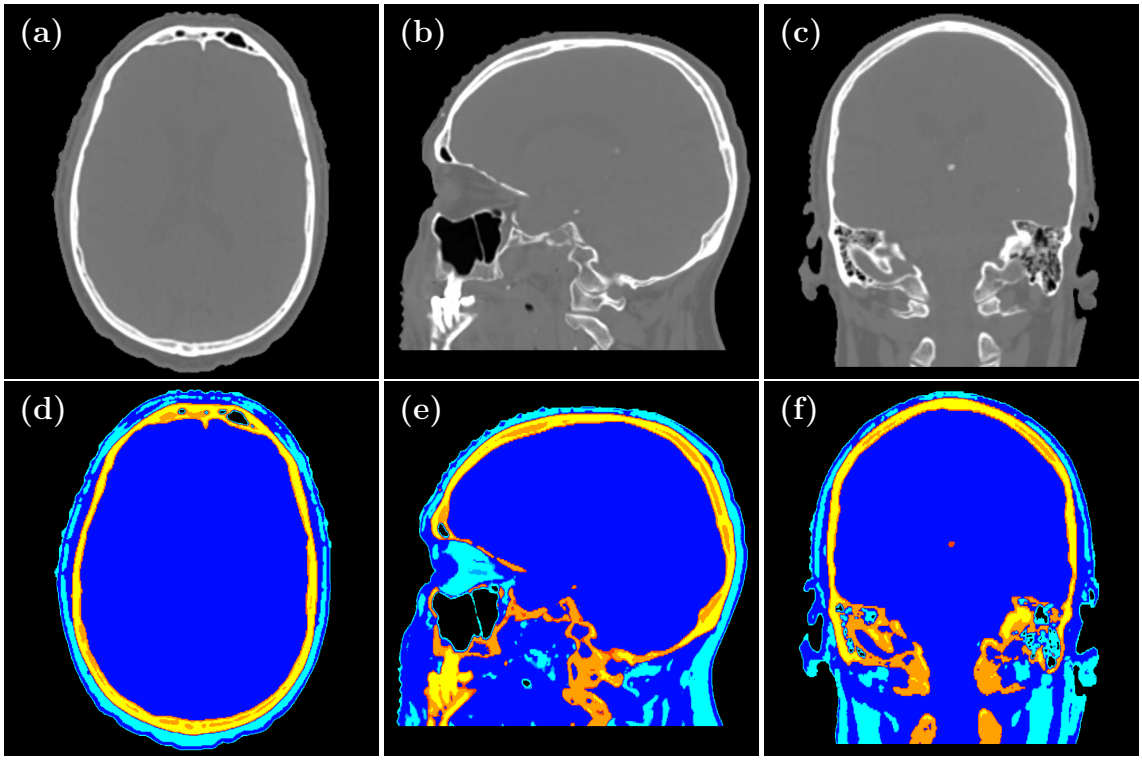

Figure 4.3: CT image (a-c) with K-means segmentation of the same CT image (4 labels) (d-e). There is shown an extra label for calcifications located in the central part of the brain (f). Axial (a, d), sagittal (b, e) and coronal view (c, f).

4.2.2 MR image segmentation

The brain tissue segmentation was carried out on T1 MR image for voxels located within the brain volume. This volume was obtained through skull stripping of the registered CT image as presented in subsection 3.3.2. Figure 4.4 shows images capturing the neighbourhood of tissue labels (CSF, WM, GM) that were acquired from the initial K-means brain tissue segmentation (see subsection 3.3.2). These images were the product of the 3D convolution between tissue labels and the 3D

kernel using the 18 neighbouring voxels. An example of original T1 MR image is compared to final MRI segmentation in figure 4.5. This segmentation expresses a superior spatial agreement with the MR source image. The use of neighbourhood information compensated the impact the relatively low and spatially inhomogeneous SNR in some MR image cases.

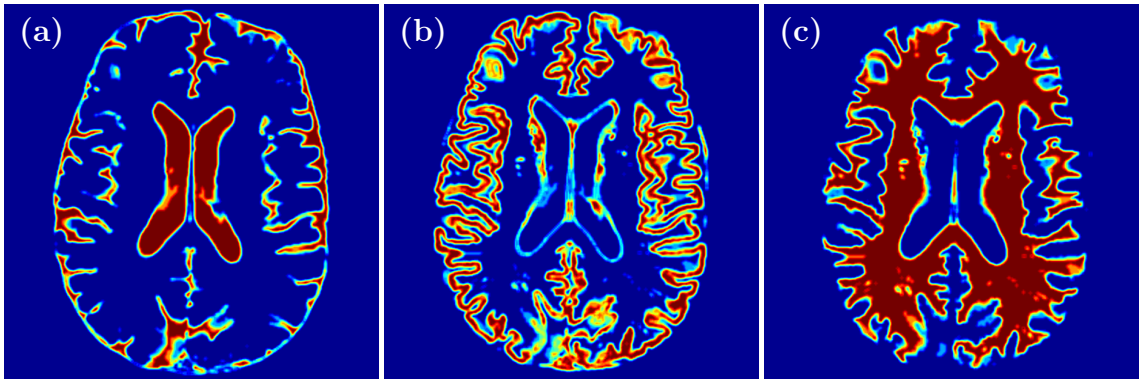

Figure 4.4: Neighbourhood probability maps obtained by convolution of the tissue labels with the 18 neighbourhood 3D kernel. These labels were derived from the K-means initialisation. The CSF (a), grey matter (b) and white matter (c) neighbourhood.

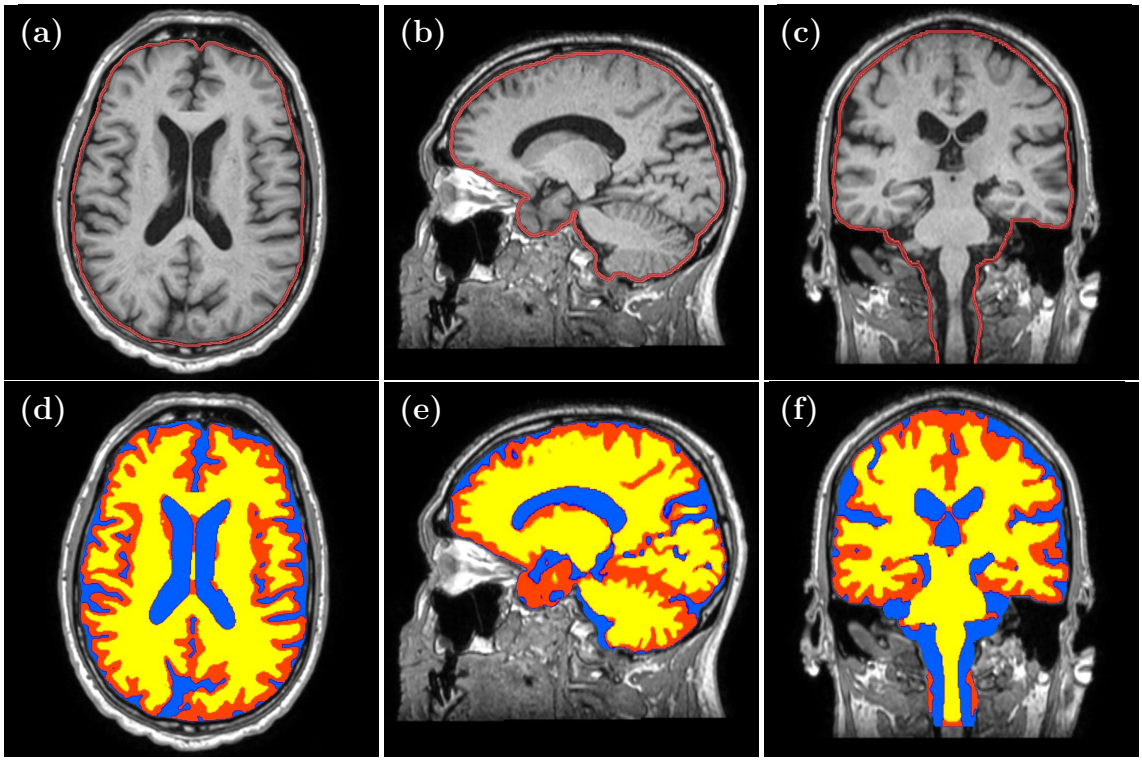

Figure 4.5: T1 weighted MR image (a-c) and corresponding MRF-ICM segmentation (d-f) of the voxels located inside of the brain mask. This mask is denoted by the red line in MR image (a-c). Axial (a, d), sagittal (b, e) and coronal view (c, f).

4.3 Flattened CT images

4.3.1 Bulk tissue HU values

The FOV was cut in the inferior direction (see figure 4.6) in order to reduce the impact of voxels not likely to be within the beam path on the bulk tissue HU estimation. Table 4.1 shows the average HU estimates across all 10 patient CT images for all the tissue compartments included in each fCT version. The average HU value for air cavities (−986 HU) was identical to the value estimated for the background air.

The only tissue class whose HU varies over the different fCT versions is the "tissue" class. However, this is simply because different voxels were included in this class for many of the fCT versions. Firstly, in the case of fCT2 and fCT3 both fat and water-rich tissue was included resulting in an HU value of 15. Secondly, fCT4 and fCT5 tissue HU value was estimated only from the water-rich tissue label resulting in a higher HU value of 47. And finally, in the case of fCT7 and fCT8, the mean tissue value of 44 HU was calculated from the water-rich tissue when excluding the brain tissue labels (CSF, GM and WM).

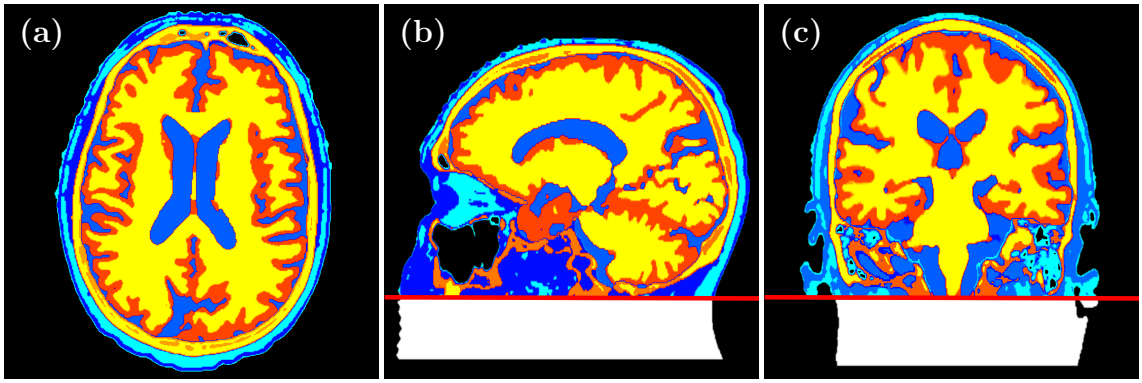

Figure 4.6: The final segmentation including both, CT and MRI-based labels, with reduced FOV in the inferior direction. The FOV reduction was undertaken for the purpose of the bulk tissue HU estimation process. Axial (a), sagittal (b) and coronal view (c).

Table 4.1: Mean HU values across all 10 patient CT images and corresponding standard deviations estimated for tissue classes encompassed in particular fCT configuration.

	fCT2	**fCT3**	**fCT4**	**fCT5**	**fCT7**	**fCT8**
Air cavities	-	−986 ± 1.22	−986 ± 1.22	−986 ± 1.22	−986 ± 1.22	−986 ± 1.22
Fat	-	-	−98 ± 11.87	−98 ± 11.87	−98 ± 11.87	−98 ± 11.87
Tissue	15 ± 9.69	15 ± 9.69	47 ± 5.04	47 ± 5.04	44 ± 6.91	44 ± 6.91
Bone	935 ± 113.98	935 ± 113.98	935 ± 113.98	-	935 ± 113.98	-
Spongy bone	-	-	-	575 ± 46.24	-	575 ± 46.24
Compact bone	-	-	-	1265 ± 86.95	-	1265 ± 86.95
CSF	-	-	-	-	16 ± 2.41	16 ± 2.41
White matter	-	-	-	-	41 ± 3.51	41 ± 3.51
Grey matter	-	-	-	-	53 ± 5.10	53 ± 5.10

4.3.2 Flattened CT visualisation

Figures 4.7 and 4.8 show a visual comparison of fCT8 with the CT image using a bone- and tissue-intensity windowing, respectively. Both comparisons show a very good visual agreement in bone and tissue spatial composition. Some differences can be observed though such as for the visualisation of calcification in the middle of the brain as well as in the visualisation of the less dense bones such as C1.

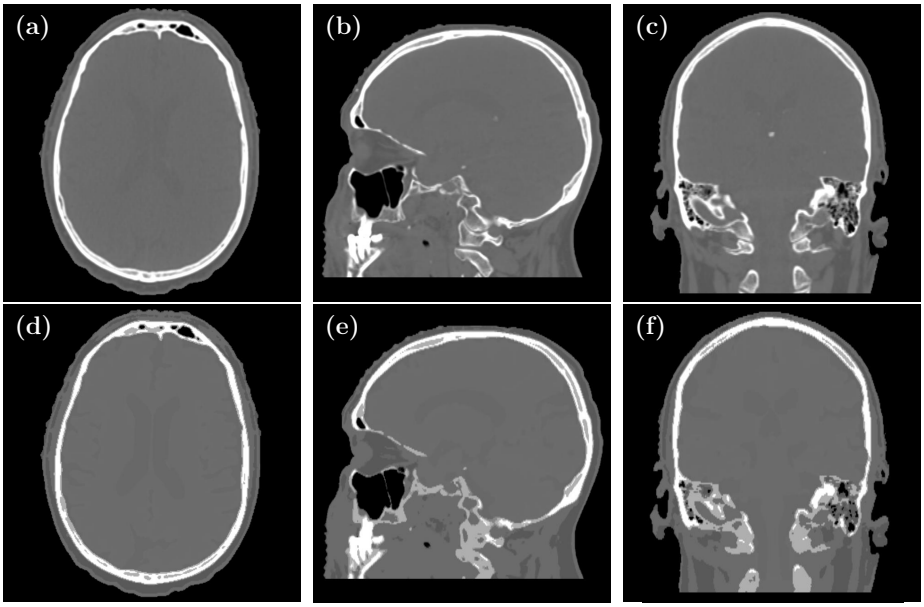

Figure 4.7: A comparison of the CT image (a-c) with the fCT8 (d-f) using the bone intensity window. Axial (a, d), sagittal (b, e) and coronal view (c, f).

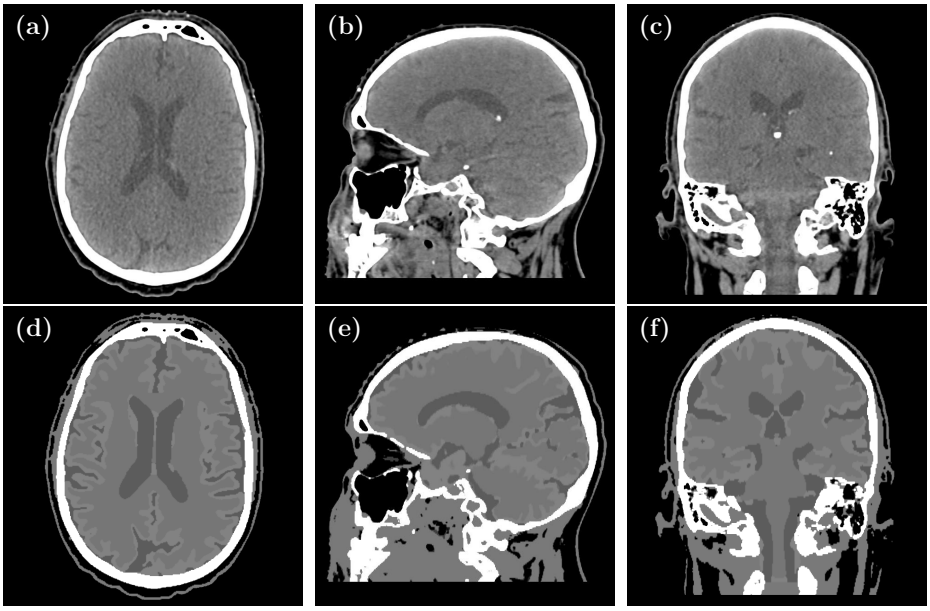

Figure 4.8: A comparison of the CT image (a-c) with the fCT8 (d-f) using the soft tissue intensity window. Axial (a, d), sagittal (b, e) and coronal view (c, f).

4.3.3 Image quality evaluation

Mean absolute (MAE) and mean errors (ME) were calculated for all voxels located within the binary mask with reduced brain FOV as presented in figure 4.6. The error values are shown in table 4.2. The errors were further calculated within the single tissue labels, and the results are shown in tables 4.3 and 4.4.

Table 4.2: Mean absolute errors (MAE) and mean errors (ME) in HU and standard deviations from patient volume between fCT and CT images across all 10 patients.

	fCT2	**fCT3**	**fCT4**	**fCT5**	**fCT7**	**fCT8**
MAE	134.79 ± 12.25	111.51 ± 11.39	90.41 ± 8.97	59.66 ± 3.91	90.37 ± 9.18	59.63 ± 4.15
ME	26.03 ± 28.45	-3.84 ± 24.36	-4.65 ± 25.24	-4.18 ± 14.76	-7.14 ± 25.17	-6.67 ± 14.64

Table 4.3: Mean absolute errors (MAE), and their standard deviations between fCT and CT images in HU estimated within the tissue labels across all 10 patients.

	fCT2	**fCT3**	**fCT4**	**fCT5**	**fCT7**	**fCT8**
Air cavities	-	112.44 ± 9.81	112.44 ± 9.81	112.44 ± 9.81	112.44 ± 9.81	112.44 ± 9.81
Fat	-	-	47.68 ± 8.55	47.68 ± 8.55	47.68 ± 8.55	47.68 ± 8.55
Tissue	84.35 ± 9.80	53.76 ± 6.51	21.46 ± 1.76	21.46 ± 1.76	39.00 ± 2.61	39.00 ± 2.61
Bone	360.13 ± 34.17	360.13 ± 34.17	360.13 ± 34.17	-	360.13 ± 34.17	-
Spongy bone	-	-	-	202.61 ± 21.39	-	202.61 ± 21.39
Compact bone	-	-	-	187.16 ± 19.62	-	187.16 ± 19.62
CSF	-	-	-	-	27.32 ± 8.88	27.32 ± 8.88
White matter	-	-	-	-	10.47 ± 2.91	10.47 ± 2.91
Grey matter	-	-	-	-	14.68 ± 2.21	14.68 ± 2.21

Table 4.4: Mean errors (ME) and their standard deviations between fCT and CT images in HU estimated within the tissue labels across all 10 patients.

	fCT2	**fCT3**	**fCT4**	**fCT5**	**fCT7**	**fCT8**
Air cavities	-	-110.39 ± 9.95	-110.39 ± 9.95	-110.39 ± 9.95	-110.39 ± 9.95	-110.39 ± 9.95
Fat	-	-	-0.20 ± 11.87	-0.20 ± 11.87	-0.20 ± 11.87	-0.20 ± 11.87
Tissue	32.85 ± 14.41	0.34 ± 9.69	-0.46 ± 5.04	-0.46 ± 5.04	0.13 ± 6.91	0.13 ± 6.91
Bone	-0.49 ± 113.98	-0.49 ± 113.98	-0.49 ± 113.98	-	-0.49 ± 108.14	-
Spongy bone	-	-	-	0.40 ± 46.24	-	0.40 ± 46.24
Compact bone	-	-	-	-0.16 ± 86.95	-	-0.16 ± 86.95
CSF	-	-	-	-	-24.96 ± 9.64	-24.96 ± 9.64
White matter	-	-	-	-	-4.70 ± 4.16	-4.70 ± 4.16
Grey matter	-	-	-	-	-1.92 ± 4.79	-1.92 ± 4.79

MAE from the head volume (see table 4.2) decrease with increasing number of tissue compartments up to fCT5 configuration (except the fCT7). MAE shows the significant impact ($\Delta MAE = -21.10\,\text{HU}$) of soft tissue stratification into the fat and water-rich tissue (fCT3 vs. fCT4). The bone stratification into two bone compartments (fCT4 vs. fCT5) resulted in the even higher difference of ($\Delta MAE = -30.75\,\text{HU}$). However, the brain stratification had very low impact on MAE results ($\Delta MAE = -0.03\,\text{HU}$).

ME values served for the verification of the correct bulk HU assignment to segmented labels. The low but non-zero ME values in tables 4.2 and 4.4 were the

result of the rounding of calculated HU values into integers as well as the result of using modified methods for the bulk HU estimation for the CSF, GM, WM, and air cavities (see subsection: 3.3.3). Table 4.4 with ME from single tissue labels shows very low errors for those tissues segmented directly from the CT image. An exception was the fCT2, where the air cavities were filled with the soft tissue bulk HU value (15,HU), and this is in turn resulted in larger ME of 32.85 HU.

For the visual evaluation of the fCT images were in addition to the MAE and ME generated fCT-CT HU difference maps (see figure 4.9). There can be observed the impact of adding the air cavities (fCT2 vs. fCT3), fat tissue class (fCT3 vs. fCT4) and bone classes (fCT4 vs. fCT5 and fCT7 vs. fCT8). The impact of the brain tissue stratification (fCT4 vs. fCT7 and fCT5 vs. fCT8) was visually negligible.

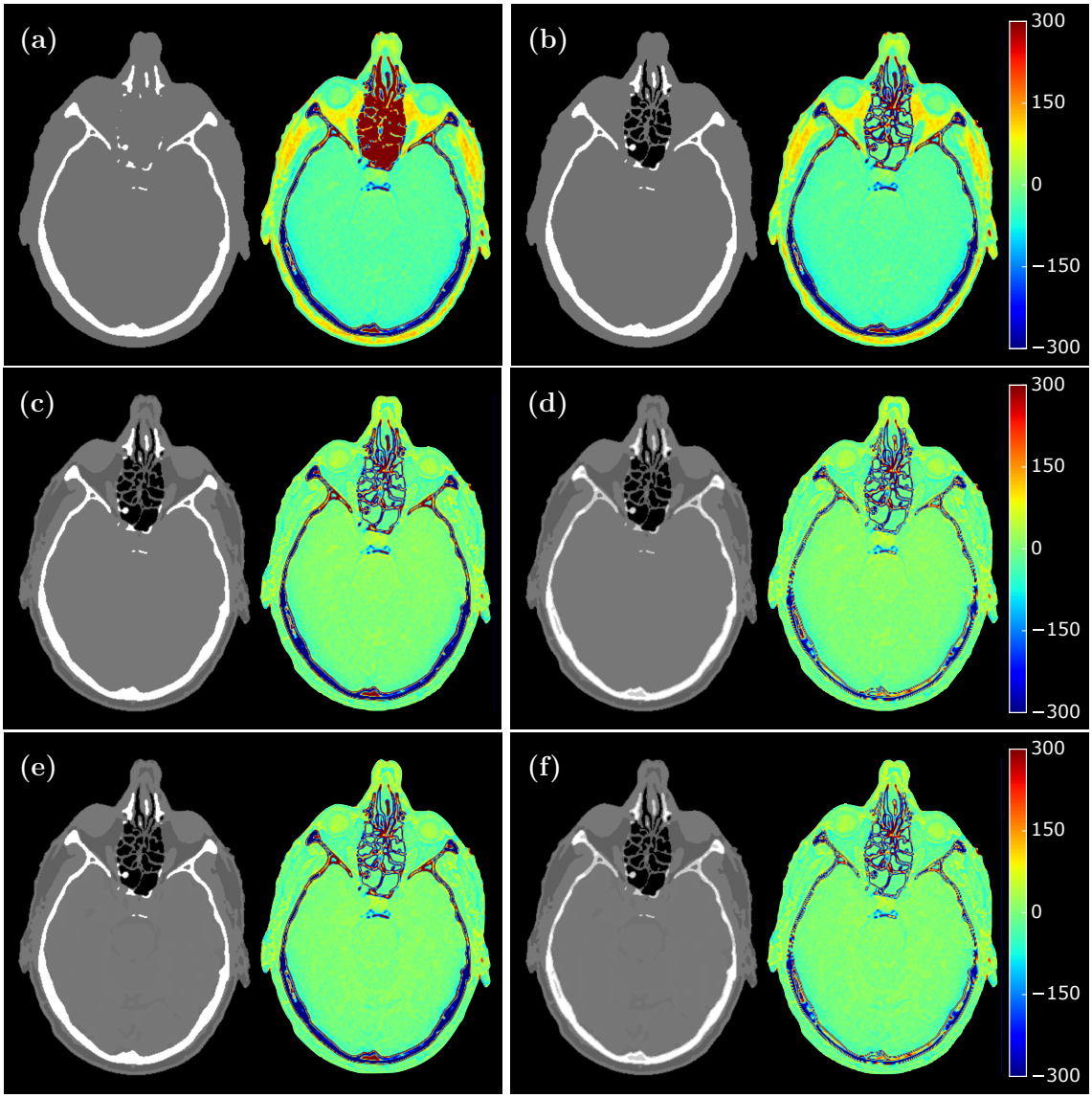

Figure 4.9: fCT versions and fCT-CT HU difference maps. Depicted are fCT2 (a), fCT3 (b), fCT4 (c), fCT5 (d), fCT7 (e) and fCT8 (f). Colorbars show difference scale in HU.

4.4 PTV position analysis

4.4.1 Simplified radiotherapy plans

Simplified RT plans with spherical PTVs in six locations for each patient were created for the purpose of PTV position dose analysis. The primary aim of the RT plan optimisation was to achieve a PTV coverage by the 95% isodose volume while maintaining steep gradients around the PTV. An example of such a simplified plan is shown in figure 4.10.

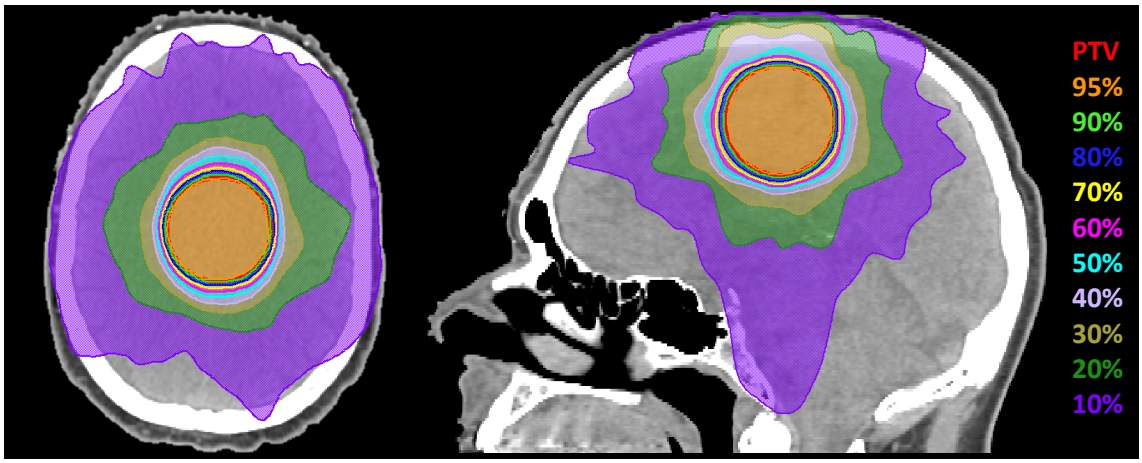

Figure 4.10: An example of an optimised simplified RT plan with the PTV (seen as a faint red line barely outside the orange 95% isodose volume) in superior-central (SC) location. Isodose volumes normalised to the maximum dose point are colour-washed (e.g. 95% isodose volume - orange).

4.4.2 DVH analysis

DVH statistics and graphs were calculated for PTVs and RINGs overlaid on dose distributions that were obtained from the optimised CT and fCT-based RT plans. An example of the cumulative DVH for the PTV in the SC position is shown in figure 4.11. This graph shows the reference CT in comparison with fCT8 and fCTw. While the fCT8 shows a very small difference in both PTV and RINGs (less than 0.5%), the fCTw shows a difference in the range between 2% and 3% in comparison with the CT. Dose differences of such ranges were observed in multiple DVH points as it is shown in tables 4.5 and 4.6 presenting the percentage differences in selected DVH point statistics.

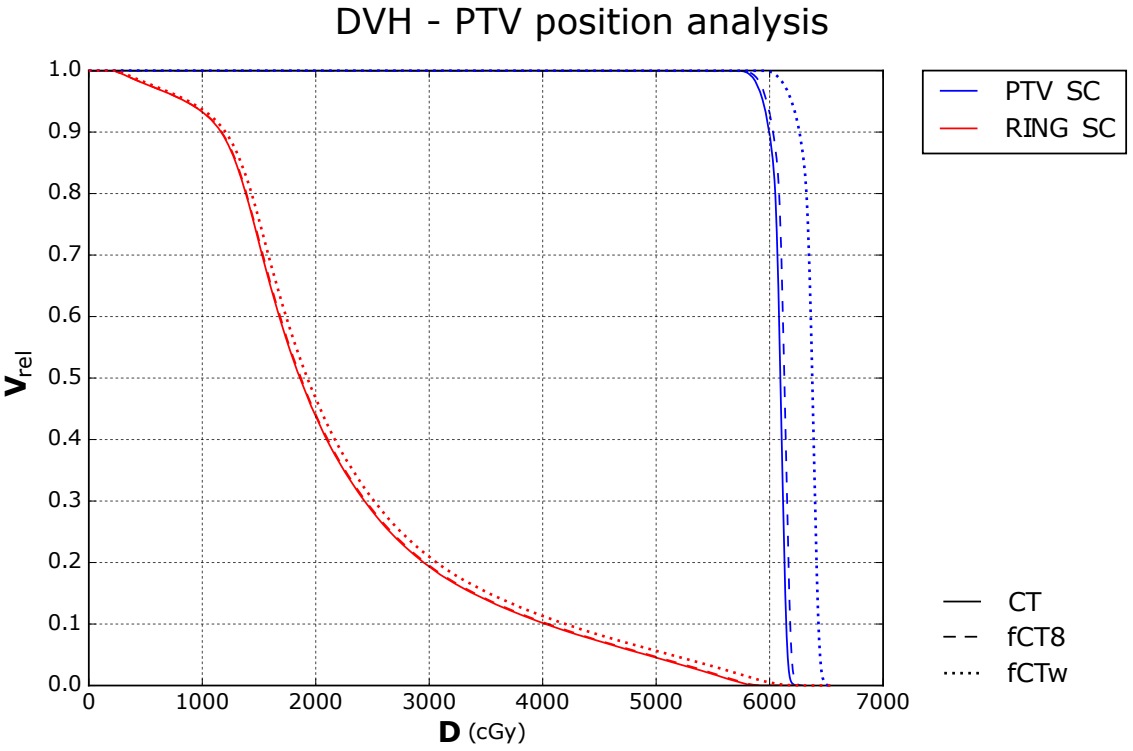

Figure 4.11: An example of DVH from the PTV position dose analysis for the PTV SC position. The difference between CT, and fCT8 (dashed) and fCTw (dotted).

Table 4.5: Mean percentual difference (fCT-CT) of DVH statistics in the PTV for single fCT versions in all the PTV position. Statistics are estimated from 60 fCT-CT RT plan pairs for each fCT version (420 RT dose comparisons in total).

	fCTw	**fCT2**	**fCT3**	**fCT4**	**fCT5**	**fCT7**	**fCT8**
ΔD_{mean}	2.70 ± 0.65	0.35 ± 0.43	0.47 ± 0.37	0.18 ± 0.38	0.05 ± 0.21	0.25 ± 0.38	0.12 ± 0.21
$\Delta D_{2\%}$	2.82 ± 0.67	0.41 ± 0.42	0.49 ± 0.37	0.20 ± 0.37	0.06 ± 0.21	0.26 ± 0.38	0.12 ± 0.21
$\Delta D_{50\%}$	2.72 ± 0.66	0.36 ± 0.43	0.49 ± 0.38	0.18 ± 0.37	0.05 ± 0.21	0.25 ± 0.38	0.12 ± 0.21
$\Delta D_{95\%}$	2.50 ± 0.64	0.23 ± 0.42	0.38 ± 0.37	0.19 ± 0.37	0.06 ± 0.21	0.25 ± 0.38	0.12 ± 0.21
$\Delta D_{98\%}$	2.37 ± 0.62	0.21 ± 0.41	0.37 ± 0.38	0.19 ± 0.37	0.06 ± 0.21	0.25 ± 0.38	0.12 ± 0.21
$\Delta V_{95\%}$	-0.19 ± 0.37	-0.28 ± 0.29	-0.34 ± 0.13	0.06 ± 0.13	0.04 ± 0.11	0.04 ± 0.12	0.02 ± 0.12

Table 4.6: Mean percentual difference (fCT-CT) of DVH statistics for RINGs covering the normal tissue for single fCT versions in all the PTV positions. Statistics from 60 fCT-CT RT plan pairs for each fCT version (420 RT plan comparisons in total).

	fCTw	**fCT2**	**fCT3**	**fCT4**	**fCT5**	**fCT7**	**fCT8**
ΔD_{mean}	2.38 ± 0.65	0.37 ± 0.37	0.47 ± 0.33	0.17 ± 0.34	0.00 ± 0.28	0.24 ± 0.34	0.06 ± 0.28
ΔD_{max}	3.18 ± 0.77	0.41 ± 0.56	0.37 ± 0.34	0.19 ± 0.34	0.06 ± 0.18	0.23 ± 0.34	0.10 ± 0.17
$\Delta D_{50\%}$	2.19 ± 0.62	0.38 ± 0.37	0.49 ± 0.30	0.15 ± 0.31	-0.01 ± 0.26	0.22 ± 0.31	0.06 ± 0.26
$\Delta D_{90\%}$	2.17 ± 1.10	0.47 ± 0.35	0.58 ± 0.35	0.27 ± 0.48	-0.12 ± 0.86	0.35 ± 0.48	-0.05 ± 0.86

Mean differences of statistics in selected DVH points were evaluated based on both fCT version and the PTV position. In general, there were some low, but nevertheless substantial trends. Figure 4.12 shows results for D_{mean} and $D_{95\%}$ DVH points.

An impact of the PTV position is evident only in the case of cerebellar position (CR) where can be observed the clear effect of adding the air cavities (fCT2 vs. fCT3). The superior fCT2 performance can be explained in the way that both, missing air cavities (filled by soft tissue bulk HU) and fat classes cancelled each other out, while this was not the case of the fCT3 which already includes the air cavity compartment. All the other trends are related rather to the fCT configuration (HU assignment). There is a clear impact of the tissue stratification into the water-rich tissue and fat (fCT3 vs. fCT4). The noticeable effect of splitting the bones into two compartments is visible as well. There was not detected a significant impact of the brain tissue stratification (fCT4 vs. fCT7 and fCT5 vs. fCT8).

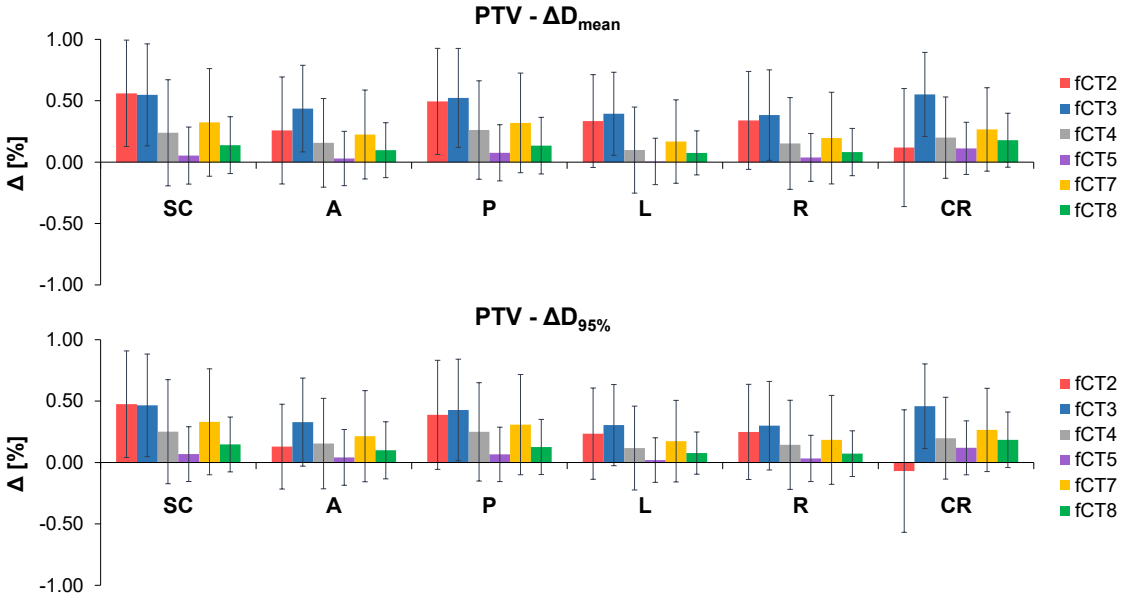

Figure 4.12: Selected DVH statistics for all the CT versions based on the PTV location. The mean differences and standard deviations between fCT and CT-based RT plans were obtained using all 10 patient cases.

The PTV conformity index (CI) which is described in subsection 3.5.2 was evaluated in the same manner, and the result can be observed in figure 4.13. The

dose conformity was regarding the PTV position affected only in the case of anterior (A) location. Here, adding of air cavities (fCT2 vs. fCT3) resulted in a decrease of the standard deviation. There can be seen a clear impact of the soft tissue and bone stratification that are more pronounced in comparison with figure 4.12.

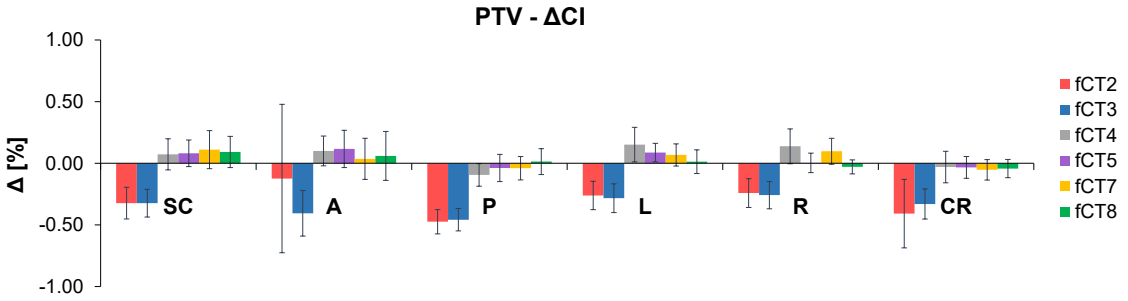

Figure 4.13: Mean differences and standard deviations of conformity index (CI) for all the CT versions across the PTV locations.

In the high and median dose ($D_{50\%}$) regions, the behaviour of the dose in the RINGs (see 4.14) showed similar trends as for the PTVs. The low dose regions $D_{90\%}$ show high standard deviations which combined with the low absolute dose values indicate the dose differences to be at the noise level.

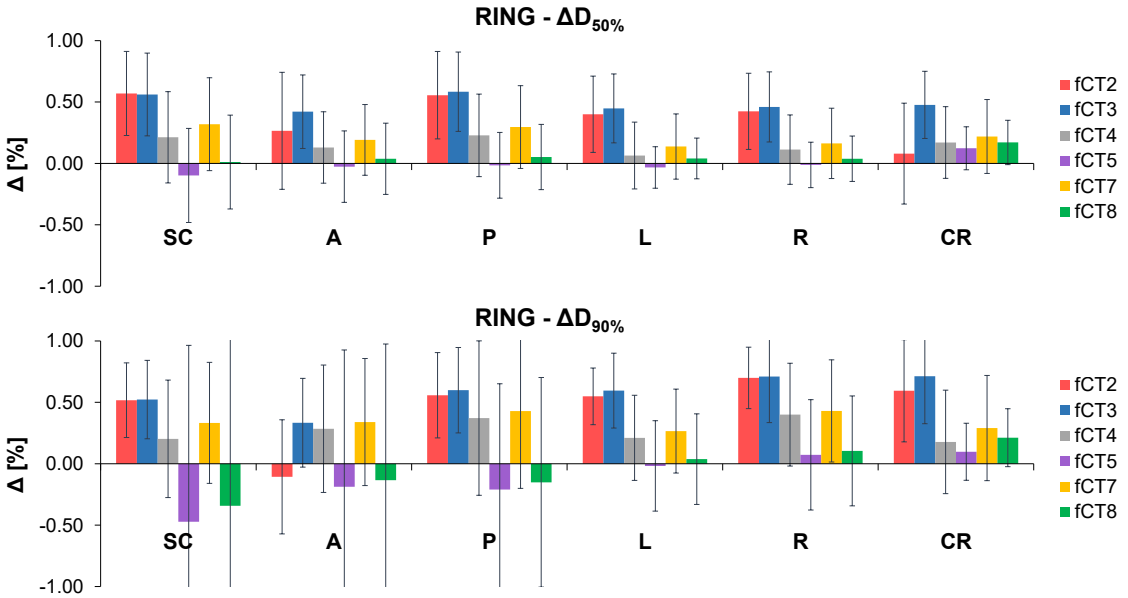

Figure 4.14: Selected DVH statistics for RINGs covering the normal tissue divided by PTV location.

4.4.3 Gamma analysis and dose difference distributions

The 1%/1 mm 3D gamma statistics (see subsections 2.4.2 and and 3.5.2) calculated from the 75% isodose volume are presented in table 4.7. 59 from 60 fCTw cases failed the criterion of 1%/1 mm using the 99% passing fraction, whereas all fCT5 and fCT8 cases passed this criterion. The passing rate increased by adding the inner air class (fCT2 vs. fCT3), tissue (fCT3 vs. fCT4) and bone stratification (fCT5 vs. fCT8). The brain tissue stratification (fCT5 vs. fCT8) did not significantly influence the gamma passing rate and overall gamma statistics.

Table 4.7: Gamma statistics from 75% isodose volume for single fCT versions from all the PTV positions.

	fCTw	**fCT2**	**fCT3**	**fCT4**	**fCT5**	**fCT7**	**fCT8**
# failures	59/60	12/60	9/60	3/60	0/60	4/60	0/60
pass. vol. [%]	52.71	96.70	96.88	99.51	100.00	99.15	100.00
median γ	1.12	0.22	0.23	0.17	0.10	0.19	0.11
max. γ	3.00	0.80	0.74	0.59	0.36	0.62	0.38

Figures 4.15, 4.16, 4.17 and 4.18 show examples of absolute gamma (1%/1mm) index and dose difference distributions for cases where the inner air, tissue, bone and brain stratifications had the largest local impact on the gamma passing rate.

Identified gamma analysis failures were caused by absence of air cavities (figure 4.15), insufficient soft tissue stratification (4.16), and bone stratification (4.17). The standalone brain tissue stratification (fCT5 vs. fCT8) did not cause any gamma failures among all the 420 dose comparisons.

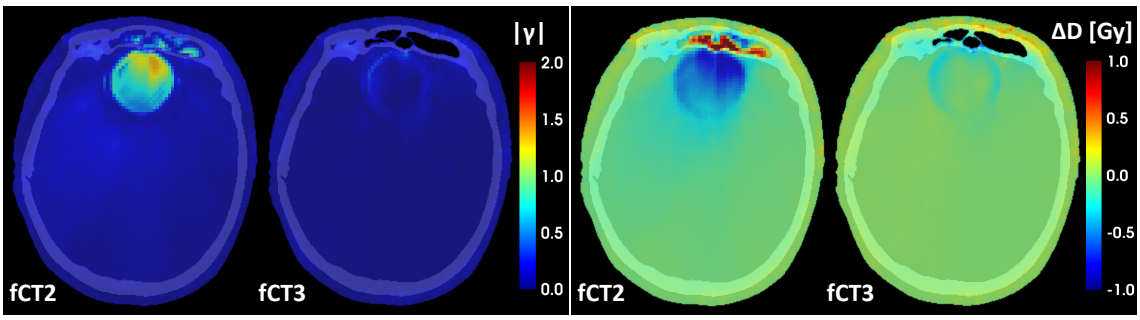

Figure 4.15: An example of the local impact of air cavities (fCT2 vs. fCT3). Gamma distributions (left) and dose difference maps (right).

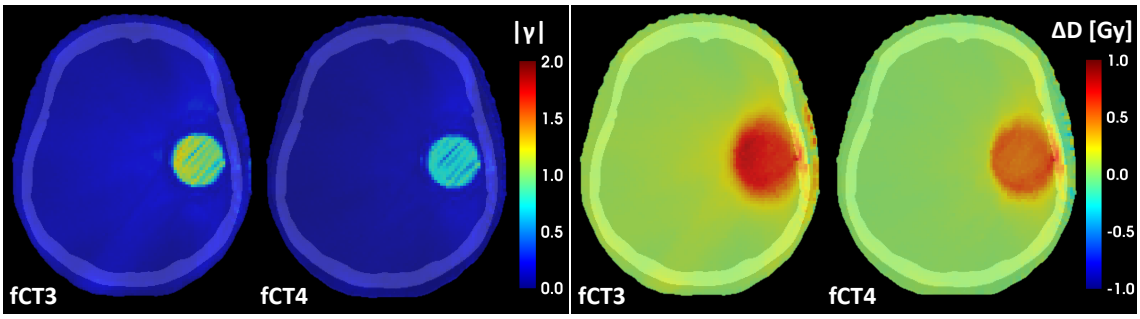

Figure 4.16: An example of the impact of the soft tissue stratification (fat, water-rich tissue) (fCT3 vs. fCT4). Gamma distributions (left) and dose difference maps (right).

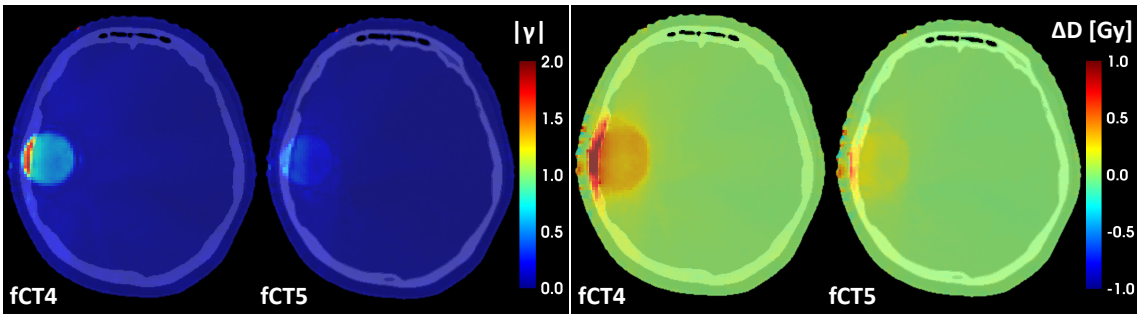

Figure 4.17: An example of the local impact of the bone stratifications (spongy bone, compact bone) (fCT4 vs. fCT5). Gamma distributions (left) and dose difference maps (right).

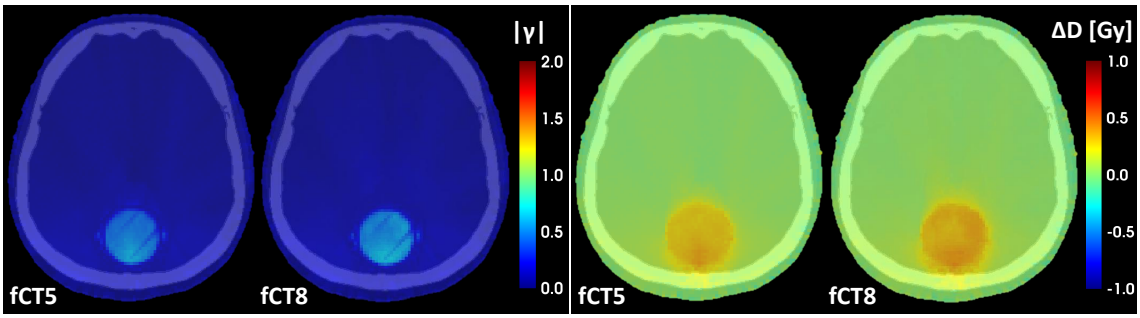

Figure 4.18: An example of a very low impact of the brain tissue stratifications (CSF, grey matter and white matter) (fCT5 vs. fCT8). Gamma distributions (left) and dose difference maps (right).

4.5 Technical approximations of clinical RT plans

4.5.1 Radiotherapy plans

Five IMRT and five VMAT technical approximations of RT plans were generated using clinical PTV and OAR delineations. The purpose of this step was to verify the outcomes of the PTV position dose analysis using clinical-like RT plans. The primary aim of the RT plan optimisation was to achieve PTV coverage by the 95% isodose volume while maintaining steep gradients around PTV. Figures 4.19 and 4.20 show examples of optimised IMRT and VMAT RT plans.

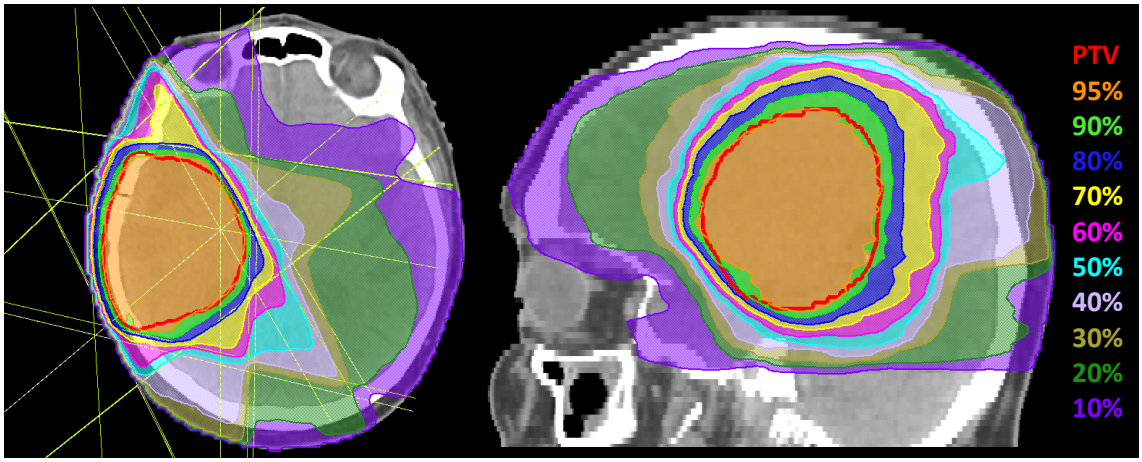

Figure 4.19: An example of optimised technical approximation of the IMRT RT plan with single PTV (red outline). Isodose volumes normalised to the maximum dose point are colour washed (e.g. 95% isodose volume - orange).

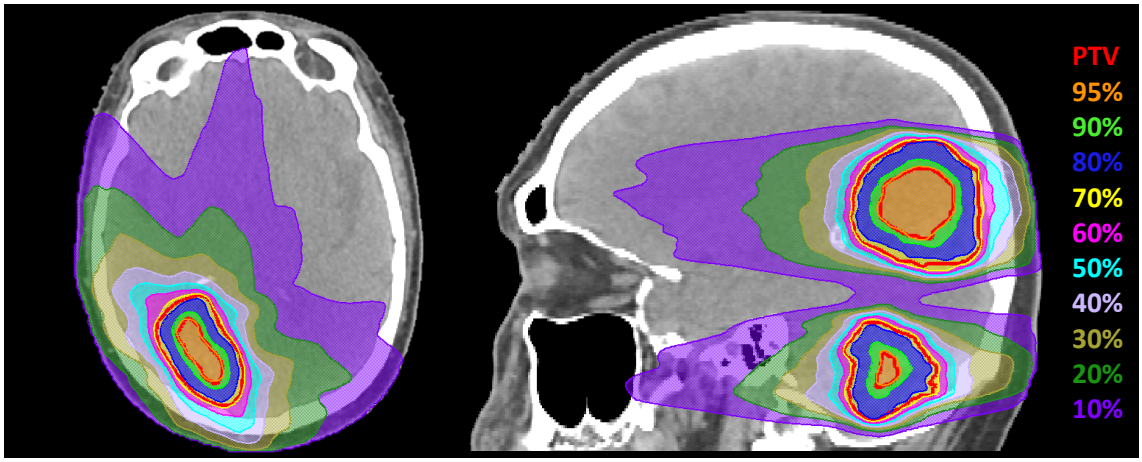

Figure 4.20: An example of optimised technical approximation of the VMAT RT plan with complex PTV shape displayed as two separate units in the sagittal plane (superior and inferior delineations). PTV 1 is in each of these PTV units represented by the outer red layers. The PTV 2 (generated from the auxiliary structure), that is roughly covered by 95% isosurface (orange), is highlighted by the inner red layers.

4.5.2 DVH analysis

Figure 4.21 shows an example of the cumulative DVH for the VMAT RT plan from figure 4.20. This graph displays the reference CT in comparison with fCT8 and fCTw. While the fCT8 shows a very low difference in both PTVs (less than 0.5%), the fCTw shows a difference in the range between 2% and 3% that is very similar to that seen for the simplified RT plans with spherical PTVs in Fig. 4.11. This level of dose difference is seen to be typical when looking at tables in 4.8 and 4.9 where the percentage differences in the selected DVH point statistics for PTV 1 and PTV 2 are given. The significant change was in comparison with PTV position analysis observed in $\Delta V_{95\%}$ for the PTV 1 where the tissue stratification (fat, water-rich) caused a 4.14% decrease.

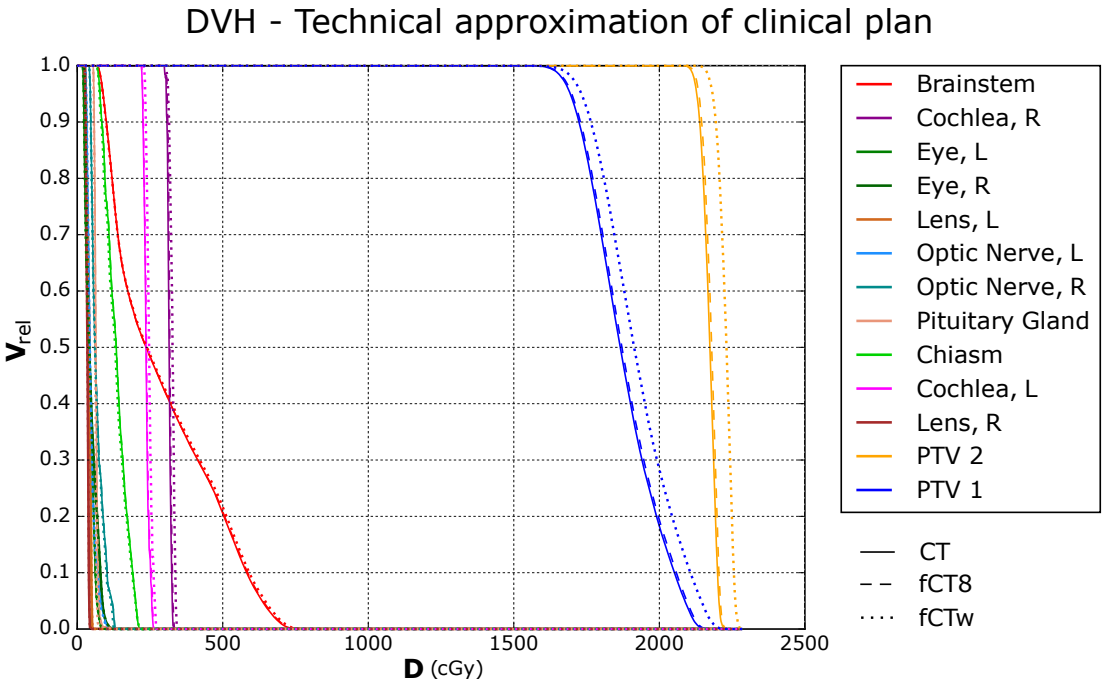

Figure 4.21: An example of DVH from the technical approximation of the clinical VMAT RT plan. The difference between CT, and fCT8 (dashed) and fCTw (dotted).

Table 4.8: Mean percentual difference (fCT-CT) of DVH statistics for clinical PTV 1 in all the fCT versions

	fCTw	fCT2	fCT3	fCT4	fCT5	fCT7	fCT8
ΔD_{mean}	2.61 ± 1.10	0.27 ± 0.58	0.36 ± 0.53	0.29 ± 0.42	0.15 ± 0.18	0.34 ± 0.43	0.19 ± 0.19
$\Delta D_{2\%}$	3.20 ± 1.07	0.49 ± 0.59	0.57 ± 0.51	0.45 ± 0.48	0.27 ± 0.32	0.42 ± 0.48	0.32 ± 0.31
$\Delta D_{50\%}$	2.67 ± 1.09	0.25 ± 0.59	0.35 ± 0.53	0.29 ± 0.42	0.15 ± 0.19	0.34 ± 0.43	0.19 ± 0.20
$\Delta D_{95\%}$	2.01 ± 1.23	0.06 ± 0.82	0.13 ± 0.81	0.05 ± 0.77	-0.08 ± 0.67	0.09 ± 0.77	-0.03 ± 0.68
$\Delta D_{98\%}$	1.71 ± 1.42	-0.08 ± 1.05	-0.02 ± 1.01	-0.05 ± 1.02	-0.16 ± 0.89	-0.01 ± 1.02	-0.11 ± 0.90
$\Delta V_{95\%}$	-6.52 ± 10.96	-6.28 ± 5.03	-5.15 ± 6.30	-1.01 ± 4.68	0.74 ± 4.65	-2.24 ± 3.96	0.44 ± 3.95

Table 4.9: Mean percentual difference (fCT-CT) of DVH statistics for clinical PTV 2 in all the fCT versions

	fCTw	fCT2	fCT3	fCT4	fCT5	fCT7	fCT8
ΔD_{mean}	2.70 ± 1.02	0.26 ± 0.54	0.33 ± 0.52	0.24 ± 0.42	0.14 ± 0.18	0.29 ± 0.42	0.19 ± 0.18
$\Delta D_{2\%}$	3.20 ± 1.03	0.37 ± 0.51	0.40 ± 0.51	0.29 ± 0.42	0.18 ± 0.20	0.34 ± 0.41	0.23 ± 0.18
$\Delta D_{50\%}$	2.69 ± 1.05	0.28 ± 0.54	0.34 ± 0.52	0.26 ± 0.42	0.15 ± 0.18	0.30 ± 0.42	0.20 ± 0.18
$\Delta D_{95\%}$	2.40 ± 1.08	0.13 ± 0.58	0.21 ± 0.57	0.17 ± 0.46	0.11 ± 0.22	0.22 ± 0.47	0.15 ± 0.23
$\Delta D_{98\%}$	2.24 ± 1.21	0.09 ± 0.59	0.17 ± 0.60	0.16 ± 0.47	0.09 ± 0.24	0.19 ± 0.48	0.13 ± 0.25
$\Delta V_{95\%}$	-0.17 ± 0.29	-0.04 ± 0.11	0.16 ± 0.68	-0.01 ± 0.05	-0.01 ± 0.03	-0.01 ± 0.04	0.00 ± 0.02

Figure 4.22 shows how is the ΔD_{max} for OARs in relation to the fCT versions. A substantial decrease in both ΔD_{max} and standard deviation values can be observed with an increasing number of tissue compartments. However, the absolute dose values were very low especially in the case of VMAT plans, and therefore even the small change in dose may indicate a relatively large, however, clinically not relevant impact.

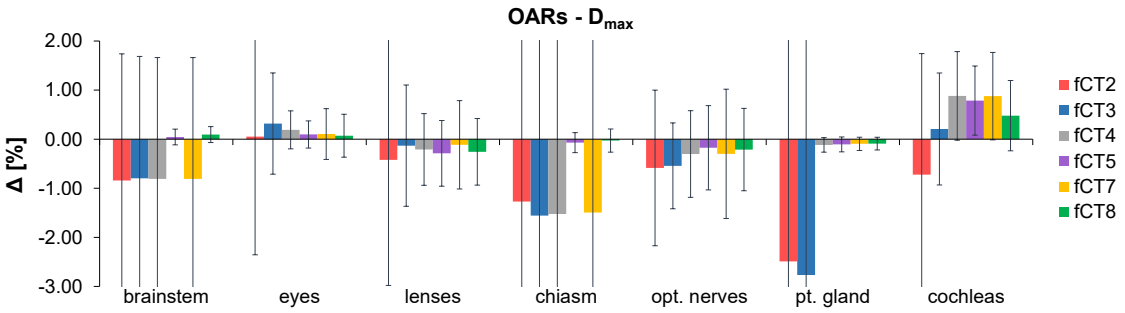

Figure 4.22: Changes in maximum dose in OARs with different fCT versions.

4.5.3 Gamma analysis and dose difference distributions

The gamma statistics calculated from the 75% isodose volume is presented in table 4.10. All 10 fCTw cases failed the criterion of 1%/1 mm with 99% gamma passing fraction, whereas all fCT5 and fCT8 images passed the analysis. The passing rate increased by adding the inner air cavity class (fCT2 vs. fCT3) and bone stratification (fCT5 vs. fCT8). The brain tissue stratification (fCT5 vs. fCT8) did not significantly influence the passing rate or other gamma statistics.

Table 4.10: Gamma statistics from 75% isodose volume for single fCT versions.

	fCTw	fCT2	fCT3	fCT4	fCT5	fCT7	fCT8
# failures	10/10	3/10	2/10	2/10	0/10	2/10	0/10
pass. vol. [%]	55.81	98.76	99.01	99.51	99.93	99.50	99.93
median γ	0.96	0.18	0.19	0.15	0.10	0.16	0.11
max. γ	6.29	3.44	2.10	2.06	1.78	2.09	1.77

Figure 4.23 shows examples of absolute gamma (1%/1 mm) index and dose difference distributions from the IMRT plan for fCTw and fCT8 of the same patient. There is a noticeable impact of the metallic skull clip which has a high intensity (> 2000 HU) in the original CT image. Figure 4.24 shows an example of the bone stratification impact (fCT4 vs. fCT5) on the gamma passing rate. Two axial slices of the same patient are displayed.

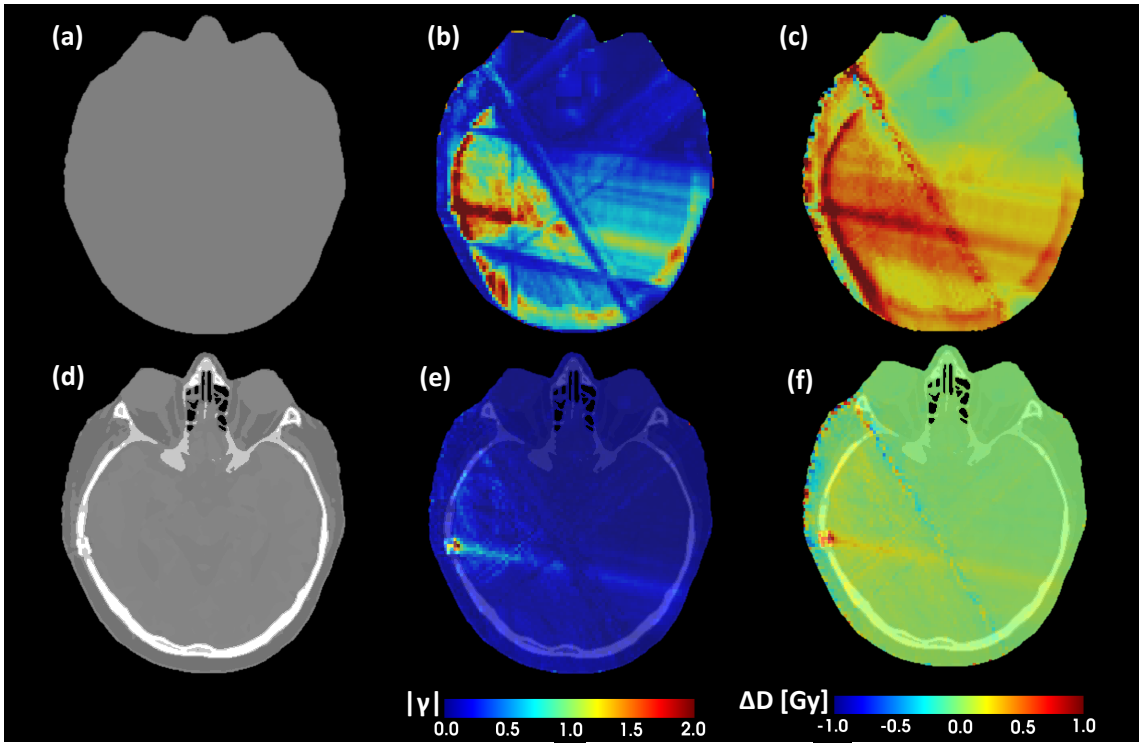

Figure 4.23: A comparison of gamma distributions (b, c) and dose difference maps (a, e) for fCTw (a) and fCT8 (d) with respect to the reference CT image. Gamma and dose distributions for fCTw (b, e) and fCT8 (c, f). A metallic skull clip with high HU value in the original CT (not shown) can be seen to impact the dose and gamma distributions.

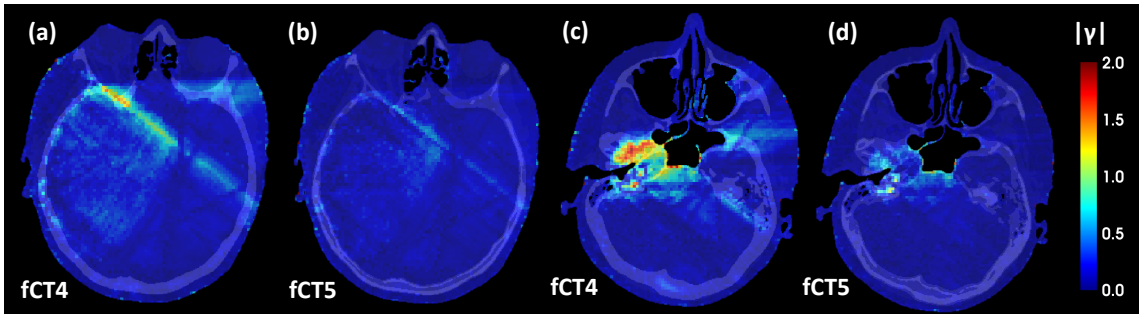

Figure 4.24: An example of bone stratification impact (fCT4 vs. fCT5) on gamma distribution. Displayed are two slices (a, b) and (c, d) from the same patient.

5 Discussion

The primary aim of this study was to figure out what tissues need to be classified/segmented and assigned separate HUs for the dose accuracy to be sufficient in the MR-only workflow for brain tumour treatment. Understanding which tissues need to be clearly visible is important when choosing the MR scan sequence to be used as input for pCT generation, because the MR image quality will directly impact the reliability of the tissue classification. To avoid confounding effects such as CT-MR fusion error, flattened CT images were used for comparison against the original CT images, thereby ensuring that only the tissue stratification affects the RT planning accuracy.

The presented analysis was divided into two broad categories, both essential for meeting the goals of this study. The first category includes steps that were needed for the flattened CT generation. These steps comprised the head mask generation, 3D image segmentation and the bulk tissue HU estimation. The second and most detailed part of this study included the generation of both simplified and clinical-like RT plans followed by the execution of comprehensive dose comparisons between RT plans calculated on CT and fCT images.

5.1 Flattened CT images

5.1.1 Head volume mask

The binary head mask was an essential component for several aspects of this study. In a first step, the thermoplastic mask (TM) was removed from the image by a combination of morphological operation with the connected component labelling. The presented algorithm was, however, not satisfactory for eliminating the positioning box and specific TM that are used in the frameless SRT. Nonetheless, only two patients with the frameless SRT fixation devices were included in this study, and hence, the use of manual image post processing was acceptable. No literature references could be found with regards to TM removal, however, it was found to be an essential step to e.g. enable correct functionality of the hole filling algorithms that were employed in the head mask generation process. Moreover, the removal of the TM or other objects in CT image background guaranteed that only the patient volume influenced dose calculations.

The process of head mask generation was accomplished by the filling of the air cavities. Nevertheless, conventional algorithms for the binary hole filling failed as air cavities, and auditory canals were represented as open holes in the 3D space. An alternative solution could have been the use of the 2D floodfill algorithm, separately in all three anatomical planes, by handling single slices as 2D images. Another alternative could be morphological image closing. These solutions would likely have been adequate for filling the nasal cavities, nevertheless, both alternatives would suffer from e.g. incorrect overfilling within and behind the ear lobes. Literature reports describing comprehensive algorithms dedicated to the 3D hole filling were also found [93]. However, an implementation of advanced 3D pattern recognition algorithm would be beyond the scope of this thesis with no clear benefits. Consequently, a

different and more pragmatic solution to this problem was pursued. The fundamental idea was to use an active contour model for the generation of artificial plasters by taking advantage from the balloon-like behaviour of active contours (snakes) [94]. These contours were then used to close the 3D holes, allowing the flooodfill algorithm to fill the air voxels. Active contour models have previously been used for the segmentation of e.g. brain tumours [95] from MR images and brain tissues [96] or nasal cavities [97] from CT images, but has seemingly not been previously used for 3D hole filling.

5.1.2 Tissue stratification for MR-only RT

Tissue stratification was the second step in the fCT generation process. Tissue labels were segmented from both CT and MR images. The segmented tissues were determined either based on the CT density or MRI contrast allowing for fairly simple segmentation techniques to be used that can hopefully be at least partially reused for pCT generation from MR images only. The classification methods were selected based on their convenience for 3D image segmentation that can be a computationally demanding process.

Conventional K-means clustering was, therefore, used for CT image segmentation as it provided excellent classification outcomes even with relatively short computational times that were further reduced by clustering only voxels within the head mask. Moreover, the use of K-means clustering has been previously reported for segmentation of e.g. brain tumours from CT images [98]. The 2D K-means clustering with original and median intensity features used in this thesis was previously reported to have superior bone segmentation results for CT-liver images in comparison with other classification methods such as 1D Fuzzy C-means and 1D K-means [78, 79]. Accurate skull segmentation in pCT generation is crucial because bones and other dense structures have a larger impact on IMRT planning outcome than accurate soft tissue classification [53].

The final CT segmentation was visually compared with the original CT image in all three anatomical planes (see figure 4.3). The result shows very good spatial agreement in the segmentation of large and connected structures. The median feature was sometimes responsible for lower sensitivity in detecting small clusters such as calcifications, fat drops and thin skin regions. However, the median image helped deal with partial volume effects and noise which resulted in smoother and more anatomical CT image simulation. The alternative method for the CT segmentation could be, for example, image intensity thresholding. The literature investigating the threshold values for extracting bones [99] and air [77, 100] was studied and findings were applied for e.g. extracting the air cavities by intensity thresholding (-500 HU). However, a pure threshold based estimation for fat, water-rich tissue and bone compartments would be problematic as each CT scanner has its own CT-density calibration tables. Moreover, direct thresholding cannot be utilised for pCT generation from MR images.

Brain tissue labelling (CSF, WM and GM) was performed using the MRF-ICM classification algorithm taking the T1 MR image as the input. This segmentation method was selected as the Markov random field (MRF) takes the voxel neighbour-

hood to the account when estimating the voxel tissue probability [64, 101]. The information from surrounding voxels was helpful due to the relatively low and spatially not consistent SNR in MR images [83]. Although, the MRF-ICM is a computationally demanding method, the reduction of both the iteration count and the segmentation VOI, by applying the skull stripping, enabled efficient implementation even for the 3D brain volume segmentation.

The classification directly from the CT image was considered as the alternative solution for the brain tissue segmentation. However, this approach provided labels reflecting the voxel intensity distribution in CT image, which is highly influenced by noise and partial volume effects, rather than the real anatomical information as seen in the MR image. Anatomically more correct labels segmented from the MR image might, however, be responsible for potentially higher differences in both image quality measures and dose comparisons where the CT image is usually the reference or even the gold standard. This was taken into account for the bulk HU tissue estimations that are discussed in the following subsection of this chapter.

5.1.3 Bulk tissue HU values

The pCT generation with bulk CT number assignment has been previously reported in literature. However, these methods mostly used dual (bone and water/tissue) or triple bulk (bone, water/tissue and air) HU assignment [5, 54, 64, 102]. This finding further encouraged the use of fCT images with up to eight tissue compartments for dose comparisons presented by this study.

In the present study, bulk HU values were estimated as averages from the segmented tissue labels applied to the CT image. Resulting bulk HU values (see table 4.1) were calculated from the cohort of 10 patients. The final bulk HU values estimated from all 10 patients were −98, 935, 575 and 1265 HU for fat, average bone, spongy and compact bone respectively. Varying values between 15 and 47 HU were estimated for the soft tissue as its tissue label coverage differed from one fCT version to the other.

Factors including partial volume effects and noise within the brain tissue in the CT image required the methods used for bulk HU estimation to be slightly different (see subsection 3.3.3). Brain tissue (CSF, WM, GM) HU values were thus calculated from eroded MR-image-based tissue labels applied to the CT image. The HU value for air cavities was calculated from all image voxels (including background) with intensity below −500 HU. These methods resulted in the CT number of −986 HU for air cavities and of 16, 41 and 53 for CSF, WM and GM, respectively.

The ROI-based approach introduced by J. Korhonen et. al (2014), who picked small circular ROIs for the bulk tissue HU estimation in the pelvic CT image [103], was considered as the alternative method for brain tissue bulk HU estimation. Nevertheless, this approach was not selected as the correct ROI allocation would be a challenging task providing biased outcomes in the case of grey and white matter HU estimation.

Electron density values, that can be found in ICRU report 46 (1992), are for adipose tissue, brain and whole adult cranium reported to be 0.92, 1.04 and 1.61 g/cm^3

[104]. Converting these values using our CT-density calibration table yielded HU values of −75, 36, and 971 HU for fat, brain and whole cranium, respectively. These values can be roughly compared with our bulk HU estimates (see table 4.1). The CT number for fat (−98 HU) is in our case lower as the possible result of partial volume effects from the air that resulted in the local faulty voxel classification into the fat class. The CT number for the brain (36 HU) is not far from our estimation of 42 ± 2 HU, which was here calculated as a weighted average of the CSF, WM, and GM class using the voxel counts as weights. The CT number for entire cranium (971 HU) is in excellent agreement with our bulk HU estimation for average cranial bone (935 HU).

These comparisons give validity to our bulk tissue HU estimates that are, considering the standard deviation values, in very good agreement with CT numbers that were converted from the tissue electron densities obtained the ICRU report 46 (1992).

5.1.4 Flattened CT quality assurance

Visual comparison of the fCT images to the original CT image (viz figures 4.7 and 4.8) showed some differences such as calcifications not being represented and less dense bone is differently visualised in the fCT images.

The more objective MAE analysis showed the real (absolute) difference in the voxel HU values, whereas the ME analysis demonstrated the average HU difference within the entire patient volume. The ME should, thus, ideally be approximately zero as the result of the relative compensation between positive and negative HU differences in single voxels. This was also the case for fat, water-rich and bone tissue classes. The exception was the fCT2 version with an ME of 32.85 HU for the water-rich tissue caused by high HU differences within the air cavities that were filled by bulk HU of tissue. The different methods employed in the voxels choice for the HU estimation resulted in higher ME values in the case of air (−110.39 HU), CSF (−24.96 HU), WM (−4.70 HU) and GM (−1.92 HU). The smallest MAE and ME of 59.63 and −3.97 HU from entire patient volume were estimated for the fCT8 and fCT3.

The particularly high CSF ME is likely simply a result of a larger ratio of CSF voxels compared to all CSF voxels being on the border of the CSF class. The larger relative mismatch of voxels between HU determination and ME calculation, the larger the ME will be. For air, the HU difference to the partial volume voxels is huge. Even though the total amount of partial volume voxels compared to total air voxels may not be large, the fact that the jump is from −986 HU to −95 HU for fat or ~ 40 HU for tissue will cause a comparatively large ME. The principle applies for bone, but there the voxels used for HU estimation and ME calculation are the same which is why the ME is small.

The comparison of the here obtained ME and MAE with values reported in literature is challenging due to varying approaches used for the error calculation [43]. Furthermore, our fCT images do not suffer from spatial distortions inherent to the MRI and CT-MR image registration errors as is the case for real pCT images.

Our fCT images further captured all bore holes and resections in the skull. The accurate prediction of surgical incisions can not be achieved in e.g. the pCT images predicted by conventional atlas-based methods without the use of dedicated post-processing steps. However, robust and reliable reconstruction of such pathologies may be challenging even for voxel-based methods. The impact of the skull resections on dose calculations should be, therefore, the subject of the further research.

5.2 Dose analysis

5.2.1 Radiotherapy planning

In total, 70 CT-based RT plans including 60 simplified plans with spherical PTV and 10 technical approximations of clinical RT plans were optimised in the Pinnacle 16 TPS. These RT plans were then simulated on all seven fCT configurations (fCTw - fCT8). The dose analysis thus stands on solid base counting 560 RT plans generated for 17 CT images (70 RT plans) and simulated on from them derived fCT images (490 RT plans). Overall, 136 DICOM series were employed in presented dose analysis.

Simplified RT plans were calculated on modified CT images without TM, where calcifications were replaced by water HU and voxels with unnaturally high HU values (artefacts) were replaced by compact bone HU. This was done to guarantee that only tissues and structures considered for the prospective pCT image had an impact on dose comparisons.

Technical approximations of clinical plans were, however, calculated on the original CT images, but without the TM, positioning boxes and patient couches. No further changes were in this case applied to the CT images as the main goal for the technical approximations of the clinical plans was to mimic the real clinical plans as closely as possible.

In both RT plan categories, the primary optimisation objective was set to obtain a PTV coverage of the 95% isodose surface with steep dose gradients around the PTV.

5.2.2 Dose comparisons

The PTV position dose analysis provided the majority of the data in this study, whereas the technical approximation of clinical RT plans was used to verify and supplement the outcomes of the dose comparisons. The fCT performance was assessed by DVH and the gamma analysis which are both standard methods commonly employed in dose comparisons and pCT quality assurance in general.

The convenience of the DVH analysis lies in simple interpretation of the results through 2D histograms that are ideal for comparing multiple dose distributions. Additionally, the DVH statistics is beneficial for making conclusions from large datasets. Nevertheless, DVH analysis does not capture the spatial information and due to the averaging effects may overlook local, though possibly important differences in dose distributions. Gamma analysis was therefore used to compliment the DVH analysis as the generation of 3D gamma index distributions provides spatial information of clinically relevant dose differences. Visual inspection of the gamma

index distributions was facilitated by showing corresponding 3D dose difference maps side by side.

Both DVH graphs and statistics such as D_{mean}, $D_{2\%}$, $D_{50\%}$, $D_{95\%}$, $D_{98\%}$ and $V_{95\%}$ showed mean percentage differences in the range of 2 - 3% in the case of fCTw serving as the reference. Hence, the fCTw was excluded from any further evaluation. Substantial differences, though not exceeding 1% were observed for both PTVs and RINGs in all the remaining fCT configurations. The DVH point statistics did not, with a few exceptions, show substantial dependency on PTV position (see subsection 4.4.2). However, there was a substantial difference in the DVH statistics among the fCT configurations. Dose differences in the range of up to 0.5% were observed in the case of the fCT2 and fCT3 for both PTVs and RINGs. The fCT2 and fCT3 were the only cases where the dose difference varied slightly based on the PTV positioning. This is likely due to the absence of fat and air cavities compartments as well as the particular soft tissue HU assignment applied in fCT2. The fat compartment inclusion (fCT3 vs. fCT4) resulted in a dose accuracy improvement of up to 0.20%. The bone stratification (fCT4. vs. fCT5 and fCT7 vs. fCT8) further introduced a substantial 0.15% decrease in the overall percentual DVH statistics difference. DVH analysis, however, did not prove any benefits from the brain tissue stratification (fCT5 vs. fCT8 and fCT4 vs. fCT7). The technical approximations of the clinical RT plans showed mostly similar trends as observed in the PTV position dose analysis. Here, the fCT configurations were shown to not have a clinically very significant impact on maximum dose in OARs (see figure 4.22).

Simulation of multiple PTV positions in connection with a large number of dose comparisons helped to identify rare, but important local gamma analysis failures caused by insufficient tissue stratification. More importantly, all the observed failures were eliminated by upgrading the number of stratified tissue compartments. This claim was numerically confirmed by gamma failure counts (see tables 4.7 and 4.10) where both, fCT5 and fCT8 passed the 1%/1 mm gamma analysis criterion in all 70 dose comparisons. There were identified gamma failures arising from the absence of air cavities, fat and bone stratifications, and gamma and dose difference distribution examples were shown in subsection 4.4.3. The brain tissue segmentation (fCT5 vs. fCT8) did not improve the dose comparison results in any significant manner.

Technical approximations of the clinical RT plans unveiled the local gamma failures arising from high HU difference skull clip that was in fCT5 and fCT8 filled with the compact bone HU value. This observation might be an obstacle for the MR-only RT workflow, as MR imaging by its very nature does no allow visualisation of metallic objects. Moreover, such objects are the common cause of severe artefacts and distortions in MR images. We can also speculate that the absence of surgical incision in, e.g., the atlas-based pCT images might result in local gamma failures in a similar manner as was shown in our skull clip example. Furthermore, the craniotomy seems to be, according to the TYKS data nature (see figure 3.2, and table 3.2) as well as the literature reports [14], commonly used in brain tumour treatment. Consequently, the impact of skull resections should be subject to further research.

Both DVH and gamma analyses results indicated an improved RT planning accuracy when increasing the number of the stratified tissue compartments in the

fCT images (up to the fCT5). When neglecting the evident change of fCTw vs. fCT2, the largest improvements were observed in the case of soft tissue (fCT3 vs. fCT4) and of the bone stratification (fCT4 and fCT5). The brain tissue stratification (fCT7 and fCT8), however, did not show any significant impact on the RT planning accuracy for the here studied cohort of 10 patients, and therefore, its only benefit might be restricted to the inclusion of the anatomical information about the brain structure. Both, DVH and gamma analysis results, therefore, identified the fCT5 including five tissue compartments (air cavities, fat, water-rich tissue, spongy and compact bone) together with fCT8 with the brain tissue also stratified as the most appropriate tissue segmentations for the MR-only RT workflow for the brain tumour treatment.

The overall results are in agreement with those reported in literature where differences in DVH points (PTV) were between 0.3 and 2% [5, 6, 10, 64]. Moreover 100% gamma (1%/1 mm) passing rate was reported for the PTV in the MR-only workflow for brain [6]. DVH analysis results for adding the air cavities and fat label further confirmed (fCT2. vs fCT3 and fCT3 vs. fCT4) the theory presented by Edmund et. al (2014) that assigning the correct average amount of tissue to the pCT may have larger impact on the dose accuracy than the precise geometrical representation of the original CT and MR source images [64]. The observed effect of the bone stratification (fCT4 vs. fCT5 and fCT7 vs. fCT8) further indicates the possible need either for the use of the pCT having two bone compartments or the continuous density assigned to the bone label. Statistical regression with continuous HU assignment has been previously identified as a promising method for such voxel-based pCT generation [64].

6 Conclusions

The presented work fulfilled the desired objectives. Flattened CT images serving as the substitution for MR-based pCT were generated by employing 3D image processing and segmentation methods. These images together with original CT volumes served as the base for the extensive RT planning, and dose comparisons here reported. The RT planning accuracy was assessed using two complementary standard methods for dose comparison: DVH and gamma analysis. The most relevant results were presented and further discussed in corresponding sections of this thesis.

The flattened CT version fCT5 with five tissue compartments excluding the background air showed the best results for the employed patient cohort when viewed in terms of dose accuracy alone. The fCT8 produced similar results as the fCT5 but with brain tissue also classified. This might be preferred by some clinical sites due to the slightly better visual appearance. Both fCT5 and fCT8 were, therefore, identified as the most appropriate tissue stratifications for the MR-only RT workflow for brain tumour treatment.

All fCT versions showed a high dose calculation accuracy in the DVH analysis, where even the difference of 3% for fCTw could in some cases be claimed as sufficient for the safe use in radiotherapy. The gamma analysis, however, unveiled failures caused by locally high HU differences between fCT and CT images resulting from insufficient tissue stratification. These observations have confirmed the need, earlier identified by Edmund et. al (2014), for a measure putting together the correct position and the right amount of a given tissue in pCT images [64]. The possible candidate for such a measure was presented by Demol et. al (2016) who used the modified gamma analysis replacing the dose difference criterion by the HU intensity difference in the image voxel [50].

Even though the presented dose differences between CT ad the fCT versions are relatively small and the used gamma passing criterion is rather strict, we can reasonably speculate that the importance of the correct tissue stratification may possibly be larger when inaccuracies in the pCT due to MR-inherent distortions, registration, positioning, and other errors are introduced by the real MR-only workflow. Every single improvement in dose accuracy might thus play a fundamental role in the development of a reliable and by all means safe MR-only RT solution for brain tumour treatment.

A criterion for the safe use of MRI-only RT for brain tumour treatment was suggested by Korsholm et al. (2014) as the PTV dose difference less than 2% for 95% of the patients compared to the CT-based dose calculation [5]. Although the number of patients included in this study was not large enough for such considerations, small differences in the RT planning on CT and fCT images indicated that MR-only RT planning for the brain is feasible with the pCT generated by bulk HU assignment to MRI-derived tissue classification. This feasibility has been previously reported in literature as well [5, 102]. Nevertheless, the entire MR-only workflow for brain consists of many aspects that should be further investigated. These aspects are the impact of surgery and, therefore, the presence of clips and incisions in the skull. The other very important consideration is the patient positioning and the MR compatibility of

the positioning devices and their impact on the RT planning accuracy. These aspects require further research.

References

[1] D. Andreasen, K. Van Leemput, R. H. Hansen, J. A. Andersen, and J. M. Edmund, "Patch-based generation of a pseudo ct from conventional mri sequences for mri-only radiotherapy of the bsrain," *Medical Physics*, vol. 42, no. 4, pp. 1596–1605, 2015.

[2] J. Uh, T. E. Merchant, Y. Li, X. Li, and C. Hua, "Mri-based treatment planning with pseudo ct generated through atlas registration," *Medical Physics*, vol. 41, no. 5, 2014, 051711.

[3] M. Hofmann, F. Steinke, V. Scheel, G. Charpiat, J. Farquhar, P. Aschoff, M. Brady, B. Schölkopf, and B. J. Pichler, "Mri-based attenuation correction for pet/mri: a novel approach combining pattern recognition and atlas registration," *Journal of Nuclear Medicine*, vol. 49, no. 11, pp. 1875–1883, 2008.

[4] C. Siversson, F. Nordström, T. Nilsson, T. Nyholm, J. Jonsson, A. Gunnlaugsson, and L. E. Olsson, "Technical note: Mri only prostate radiotherapy planning using the statistical decomposition algorithm," *Medical Physics*, vol. 42, no. 10, pp. 6090–6097, 2015.

[5] M. E. Korsholm, L. W. Waring, and J. M. Edmund, "A criterion for the reliable use of mri-only radiotherapy," *Radiation Oncology*, vol. 9, no. 1, p. 16, 2014.

[6] J. H. Jonsson, M. M. Akhtari, M. G. Karlsson, A. Johansson, T. Asklund, and T. Nyholm, "Accuracy of inverse treatment planning on substitute ct images derived from mr data for brain lesions," *Radiation Oncology*, vol. 10, no. 1, p. 13, 2015.

[7] "Philips introduces first commercial mr-only solution for prostate cancer treatment planning in the u.s. - news center | philips," http://www.philips.com/a-w/about/news/archive/standard/news/press/2016/20160331-philips-introduces-first-commercial-mr-only-solution-for-prostate-cancer-treatment-planning-in-the-us.html, (Accessed 2017-05-29).

[8] M. Köhler, T. Vaara, M. V. Grootel, R. Hoogeveen, R. Kemppainen, and S. Renisch, "MR-only simulation for radiotherapy planning treatment planning," *White Paper: Philips MRCAT for prostate dose calculations using only MRI data*, pp. 1–16, 2015. [Online]. Available: http://www.philips.co.uk/healthcare-solutions/magnetic-resonance/therapy-systems (Accessed 2017-05-12).

[9] B. H. Kristensen, F. J. Laursen, V. Løgager, P. F. Geertsen, and A. Krarup-Hansen, "Dosimetric and geometric evaluation of an open low-field magnetic resonance simulator for radiotherapy treatment planning of brain tumours," *Radiotherapy and Oncology*, vol. 87, no. 1, pp. 100–109, 2008.

[10] T. Stanescu, H.-S. Jans, N. Pervez, P. Stavrev, and B. G. Fallone, "A study on the magnetic resonance imaging (MRI)-based radiation treatment planning of intracranial lesions," *Physics in Medicine and Biology*, vol. 53, no. 13, pp. 3579–3593, Jul. 2008.

[11] "WHO | Cancer Key Facts." [Online]. Available: http://www.who.int/cancer/media/news/cancer-key-facts/en/ (Accessed 2017-05-12).

[12] J. Ferlay, E. Steliarova-Foucher, J. Lortet-Tieulent, S. Rosso, J. Coebergh, H. Comber, D. Forman, and F. Bray, "Cancer incidence and mortality patterns in europe: estimates for 40 countries in 2012," *European Journal of Cancer*, vol. 49, no. 6, pp. 1374–1403, 2013.

[13] D. N. Louis, A. Perry, G. Reifenberger, A. von Deimling, D. Figarella-Branger, W. K. Cavenee, H. Ohgaki, O. D. Wiestler, P. Kleihues, and D. W. Ellison, "The 2016 world health organization classification of tumors of the central nervous system: a summary," *Acta Neuropathologica*, vol. 131, no. 6, pp. 803–820, 2016.

[14] A. Barret, J. Dobbs, S. Morris, and T. Roques, "Practical radiotherapy planning," 2009.

[15] H. Nazemi-Gelyan, H. Hasanzadeh, Y. Makhdumi, S. Abdollahi, F. Akbari, F. Varshoee-Tabrizi, H. Almasrou, A. Nikoofar, and M. Rezaei-Tavirani, "Evaluation of organs at risk's dose in external radiotherapy of brain tumors," *Iranian Journal of Cancer Prevention*, vol. 8, no. 1, pp. 47–52, 2015.

[16] J. H. Lee, *Meningiomas: diagnosis, treatment, and outcome*. Springer Science & Business Media, 2008.

[17] S. Rahmani and L. S. Wong, "Central nerve system malignant tumors," *IOSR Journal of Dental and Medical Sciences (IOSR-JDMS)*, vol. 1, no. 13, pp. 52–63, 2015.

[18] M. L. Bondy, M. E. Scheurer, B. Malmer, J. S. Barnholtz-Sloan, F. G. Davis, D. Il'Yasova, C. Kruchko, B. J. McCarthy, P. Rajaraman, J. A. Schwartzbaum *et al.*, "Brain tumor epidemiology: consensus from the brain tumor epidemiology consortium," *Cancer*, vol. 113, no. S7, pp. 1953–1968, 2008.

[19] M. R. Gilbert, T. S. Armstrong, W. B. Pope, M. J. van den Bent, and P. Y. Wen, "Facing the future of brain tumor clinical research," *Clinical Cancer Research*, vol. 20, no. 22, pp. 5591–5600, 2014. [Online]. Available: https://doi.org/10.1158%2F1078-0432.ccr-14-0835 (Accessed 2017-05-12).

[20] V. Agrahari, "The exciting potential of nanotherapy in brain-tumor targeted drug delivery approaches," *Neural Regeneration Research*, vol. 12, no. 2, pp. 197–200, Feb. 2017.

[21] N. G. Burnet, S. J. Thomas, K. E. Burton, and S. J. Jefferies, "Defining the tumour and target volumes for radiotherapy," *Cancer Imaging*, vol. 4, no. 2, pp. 153–161, 2004.

[22] S.-H. Lu, J. C.-H. Cheng, S.-H. Kuo, J. J.-S. Lee, L.-H. Chen, J.-K. Wu, Y.-H. Chen, W.-Y. Chen, S.-Y. Wen, F.-C. Chong *et al.*, "Volumetric modulated arc therapy for nasopharyngeal carcinoma: a dosimetric comparison with tomotherapy and step-and-shoot imrt," *Radiotherapy and Oncology*, vol. 104, no. 3, pp. 324–330, 2012.

[23] I. Rosenberg, "Radiation oncology physics: a handbook for teachers and students," *British Journal of Cancer*, vol. 98, no. 5, p. 1020, 2008.

[24] M. Kocher, A. Wittig, M. D. Piroth, H. Treuer, H. Seegenschmiedt, M. Ruge, A.-L. Grosu, and M. Guckenberger, "Stereotactic radiosurgery for treatment of brain metastases," *Strahlentherapie und Onkologie*, vol. 190, no. 6, pp. 521–532, 2014.

[25] F. M. Khan and J. P. Gibbons, *Khan's the physics of radiation therapy*. Lippincott Williams & Wilkins, 2014.

[26] P. Mayles and J.-C. Rosenwald, "Radiation protection in radiotherapy," in *Handbook of Radiotherapy Physics: Theory and Practice*. Taylor & Francis, 2007, pp. 1229–1232.

[27] S. Scoccianti, B. Detti, D. Gadda, D. Greto, I. Furfaro, F. Meacci, G. Simontacchi, L. Di Brina, P. Bonomo, I. Giacomelli *et al.*, "Organs at risk in the brain and their dose-constraints in adults and in children: a radiation oncologist's guide for delineation in everyday practice," *Radiotherapy and Oncology*, vol. 114, no. 2, pp. 230–238, 2015.

[28] A. Isambert, F. Dhermain, F. Bidault, O. Commowick, P.-Y. Bondiau, G. Malandain, and D. Lefkopoulos, "Evaluation of an atlas-based automatic segmentation software for the delineation of brain organs at risk in a radiation therapy clinical context," *Radiotherapy and Oncology*, vol. 87, no. 1, pp. 93–99, 2008.

[29] X. Sun, S. Su, C. Chen, F. Han, C. Zhao, W. Xiao, X. Deng, S. Huang, C. Lin, and T. Lu, "Long-term outcomes of intensity-modulated radiotherapy for 868 patients with nasopharyngeal carcinoma: an analysis of survival and treatment toxicities," *Radiotherapy and Oncology*, vol. 110, no. 3, pp. 398–403, 2014.

[30] A. Dunlop, L. Welsh, D. McQuaid, J. Dean, S. Gulliford, V. Hansen, S. Bhide, C. Nutting, K. Harrington, and K. Newbold, "Brain-sparing methods for imrt of head and neck cancer," *PLoS ONE*, vol. 10, no. 3, 2015, e0120141.

[31] "Image Gallery | Varian Medical Systems." [Online]. Available: http://newsroom.varian.com/Edge (Accessed 2017-05-12).

[32] V. Feygelman, D. Hunt, L. Walker, R. Mueller, M. L. Demarco, T. Dilling, C. Stevens, and G. Zhang, "Validation of pinnacle treatment planning system for use with novalis delivery unit," *Journal of Applied Clinical Medical Physics*, vol. 11, no. 3, pp. 135–153, 2010.

[33] E. H. Lin, M. Von Korff, D. Peterson, E. J. Ludman, P. Ciechanowski, and W. Katon, "Population targeting and durability of multimorbidity collaborative care management," *The American Journal of Managed Care*, vol. 20, no. 11, pp. 887–895, 2014.

[34] A. Pugachev, J. G. Li, A. L. Boyer, S. L. Hancock, Q.-T. Le, S. S. Donaldson, and L. Xing, "Role of beam orientation optimization in intensity-modulated radiation therapy," *International Journal of Radiation Oncology* Biology* Physics*, vol. 50, no. 2, pp. 551–560, 2001.

[35] J. Staffurth *et al.*, "A review of the clinical evidence for intensity-modulated radiotherapy," *Clinical Oncology*, vol. 22, no. 8, pp. 643–657, 2010.

[36] M. Teoh, C. H. Clark, K. Wood, S. Whitaker, and A. Nisbet, "Volumetric modulated arc therapy: a review of current literature and clinical use in practice," *The British Journal of Radiology*, vol. 84, no. 1007, pp. 967–996, 2011, pMID: 22011829.

[37] G. Smyth, J. C. Bamber, P. M. Evans, and J. L. Bedford, "Trajectory optimization for dynamic couch rotation during volumetric modulated arc radiotherapy," *Physics in Medicine and Biology*, vol. 58, no. 22, pp. 8163–8177, 2013.

[38] Y. Jeong, S.-w. Lee, J. Kwak, I. Cho, S. M. Yoon, J. H. Kim, J.-h. Park, E. K. Choi, S. Y. Song, Y. S. Kim, S. S. Kim, J. H. Joo, and S. D. Ahn, "A dosimetric comparison of volumetric modulated arc therapy (vmat) and non-coplanar intensity modulated radiotherapy (imrt) for nasal cavity and paranasal sinus cancer," *Radiation Oncology*, vol. 9, no. 1, p. 193, 2014.

[39] V. Panet-Raymond, W. Ansbacher, S. Zavgorodni, B. Bendorffe, A. Nichol, P. T. Truong, W. Beckham, and M. Vlachaki, "Coplanar versus noncoplanar intensity-modulated radiation therapy (imrt) and volumetric-modulated arc therapy (vmat) treatment planning for fronto-temporal high-grade glioma," *Journal of Applied Clinical Medical Physics*, vol. 13, no. 4, 2012, s832.

[40] D. Nguyen, J.-C. M. Rwigema, V. Y. Yu, T. Kaprealian, P. Kupelian, M. Selch, P. Lee, D. A. Low, and K. Sheng, "Feasibility of extreme dose escalation for glioblastoma multiforme using 4π radiotherapy," *Radiation Oncology*, vol. 9, no. 1, p. 239, 2014.

[41] R. Shaffer, A. M. Nichol, E. Vollans, M. Fong, S. Nakano, V. Moiseenko, M. Schmuland, R. Ma, M. McKenzie, and K. Otto, "A comparison of volumetric modulated arc therapy and conventional intensity-modulated radiotherapy for

frontal and temporal high-grade gliomas," *International Journal of Radiation Oncology* Biology* Physics*, vol. 76, no. 4, pp. 1177–1184, 2010.

[42] G. Smyth, P. M. Evans, J. C. Bamber, H. C. Mandeville, L. C. Welsh, F. H. Saran, and J. L. Bedford, "Non-coplanar trajectories to improve organ at risk sparing in volumetric modulated arc therapy for primary brain tumors," *Radiotherapy and Oncology*, vol. 121, no. 1, pp. 124–131, 2016.

[43] J. M. Edmund and T. Nyholm, "A review of substitute ct generation for mri-only radiation therapy," *Radiation Oncology*, vol. 12, no. 1, p. 28, 2017.

[44] M. C. Mesias, J. Boda-Heggemann, J. Thoelking, F. Lohr, F. Wenz, and H. Wertz, "Quantification and assessment of interfraction setup errors based on cone beam ct and determination of safety margins for radiotherapy," *PLoS ONE*, vol. 11, no. 3, 2016, e0150326.

[45] S. G. Soltys, J. P. Kirkpatrick, N. N. Laack, B. D. Kavanagh, J. C. Breneman, and H. A. Shih, "Is less, more? the evolving role of radiation therapy for brain metastases," *International Journal of Radiation Oncology• Biology• Physics*, vol. 92, no. 5, pp. 963–966, 2015.

[46] T. Nyholm, M. Nyberg, M. G. Karlsson, and M. Karlsson, "Systematisation of spatial uncertainties for comparison between a mr and a ct-based radiotherapy workflow for prostate treatments," *Radiation Oncology*, vol. 4, no. 1, p. 54, 2009.

[47] S.-H. Hsu, Y. Cao, K. Huang, M. Feng, and J. M. Balter, "Investigation of a method for generating synthetic CT models from MRI scans of the head and neck for radiation therapy," *Physics in Medicine and Biology*, vol. 58, no. 23, pp. 8419–8435, 2013.

[48] J. Sjölund, D. Forsberg, M. Andersson, and H. Knutsson, "Generating patient specific pseudo-CT of the head from MR using atlas-based regression," *Physics in Medicine and Biology*, vol. 60, no. 2, pp. 825–839, 2015.

[49] B. K. Navalpakkam, H. Braun, T. Kuwert, and H. H. Quick, "Magnetic resonance–based attenuation correction for pet/mr hybrid imaging using continuous valued attenuation maps," *Investigative Radiology*, vol. 48, no. 5, pp. 323–332, 2013.

[50] B. Demol, C. Boydev, J. Korhonen, and N. Reynaert, "Dosimetric characterization of mri-only treatment planning for brain tumors in atlas-based pseudo-ct images generated from standard t1-weighted mr images," *Medical Physics*, vol. 43, no. 12, pp. 6557–6568, 2016.

[51] M. S. R. Gudur, W. Hara, Q.-T. Le, L. Wang, L. Xing, and R. Li, "A unifying probabilistic Bayesian approach to derive electron density from MRI for radiation therapy treatment planning," *Physics in Medicine and Biology*, vol. 59, no. 21, pp. 6595–6606, 2014.

[52] J. Rahmer, U. Blume, and P. Börnert, "Selective 3d ultrashort te imaging: comparison of "dual-echo" acquisition and magnetization preparation for improving short-t 2 contrast," *Magnetic Resonance Materials in Physics, Biology and Medicine*, vol. 20, no. 2, pp. 83–92, 2007.

[53] F. Wiesinger, L. I. Sacolick, A. Menini, S. S. Kaushik, S. Ahn, P. Veit-Haibach, G. Delso, and D. D. Shanbhag, "Zero te mr bone imaging in the head," *Magnetic Resonance in Medicine*, vol. 75, no. 1, pp. 107–114, 2016.

[54] V. Keereman, Y. Fierens, T. Broux, Y. De Deene, M. Lonneux, and S. Vandenberghe, "Mri-based attenuation correction for pet/mri using ultrashort echo time sequences," *Journal of Nuclear Medicine*, vol. 51, no. 5, pp. 812–818, 2010.

[55] C. M. Rank, C. Tremmel, N. Hünemohr, A. M. Nagel, O. Jäkel, and S. Greilich, "Mri-based treatment plan simulation and adaptation for ion radiotherapy using a classification-based approach," *Radiation Oncology*, vol. 8, no. 1, p. 51, 2013.

[56] R. Acosta, M. Ehrgott, A. Holder, D. Nevin, J. Reese, and B. Salter, *The influence of dose grid resolution on beam selection strategies in radiotherapy treatment design.* New York, NY: Springer New York, 2008, pp. 1–23.

[57] D. A. Low, W. B. Harms, S. Mutic, and J. A. Purdy, "A technique for the quantitative evaluation of dose distributions," *Medical Physics*, vol. 25, no. 5, pp. 656–661, 1998.

[58] J. Winiecki, T. Morgaś, K. Majewska, and B. Drzewiecka, "The gamma evaluation method as a routine qa procedure of imrt," *Reports of Practical Oncology & Radiotherapy*, vol. 14, no. 5, pp. 162–168, 2009.

[59] J.-H. Song, M.-J. Kim, S.-H. Park, S.-R. Lee, M.-Y. Lee, D. S. Lee, and T. S. Suh, "Gamma analysis dependence on specified low-dose thresholds for vmat qa," *Journal of Applied Clinical Medical Physics*, vol. 16, no. 6, pp. 263–272, 2015.

[60] K. Ulin, M. M. Urie, and J. M. Cherlow, "Results of a multi-institutional benchmark test for cranial ct/mr image registration," *International Journal of Radiation Oncology* Biology* Physics*, vol. 77, no. 5, pp. 1584–1589, 2010.

[61] G. M. Cattaneo, M. Reni, G. Rizzo, P. Castellone, G. L. Ceresoli, C. Cozzarini, A. J. M. Ferreri, P. Passoni, and R. Calandrino, "Target delineation in post-operative radiotherapy of brain gliomas: interobserver variability and impact of image registration of mr (pre-operative) images on treatment planning ct scans," *Radiotherapy and Oncology*, vol. 75, no. 2, pp. 217–223, 2005.

[62] G. Minniti, E. Clarke, G. Lanzetta, M. F. Osti, G. Trasimeni, A. Bozzao, A. Romano, and R. M. Enrici, "Stereotactic radiosurgery for brain metastases: analysis of outcome and risk of brain radionecrosis," *Radiation Oncology*, vol. 6, no. 1, p. 48, 2011.

[63] J.-F. Daisne, M. Sibomana, A. Bol, T. Doumont, M. Lonneux, and V. Grégoire, "Tri-dimensional automatic segmentation of pet volumes based on measured source-to-background ratios: influence of reconstruction algorithms," *Radiotherapy and Oncology*, vol. 69, no. 3, pp. 247–250, 2003.

[64] J. M. Edmund, H. M. Kjer, K. Van Leemput, R. H. Hansen, J. A. Andersen, and D. Andreasen, "A voxel-based investigation for MRI-only radiotherapy of the brain using ultra short echo times," *Physics in Medicine and Biology*, vol. 59, no. 23, pp. 7501–7519, Dec. 2014.

[65] E. Paradis, Y. Cao, T. S. Lawrence, C. Tsien, M. Feng, K. Vineberg, and J. M. Balter, "Assessing the dosimetric accuracy of magnetic resonance-generated synthetic ct images for focal brain vmat radiation therapy," *International Journal of Radiation Oncology* Biology* Physics*, vol. 93, no. 5, pp. 1154–1161, 2015.

[66] T. Layer, M. Blaickner, B. Knäusl, D. Georg, J. Neuwirth, R. P. Baum, C. Schuchardt, S. Wiessalla, and G. Matz, "Pet image segmentation using a gaussian mixture model and markov random fields," *EJNMMI Physics*, vol. 2, no. 1, p. 9, 2015.

[67] M. Van Herk, "Errors and margins in radiotherapy," in *Seminars in Radiation Oncology*, vol. 14, no. 1. Elsevier, 2004, pp. 52–64.

[68] F. Dhermain, "Radiotherapy of high-grade gliomas: current standards and new concepts, innovations in imaging and radiotherapy, and new therapeutic approaches," *Chinese Journal of Cancer*, vol. 33, no. 1, pp. 16–24, jan 2014.

[69] J. F. Barrett and N. Keat, "Artifacts in ct: Recognition and avoidance," *RadioGraphics*, vol. 24, no. 6, pp. 1679–1691, 2004, pMID: 15537976.

[70] A. Fedorov, R. Beichel, J. Kalpathy-Cramer, J. Finet, J.-C. Fillion-Robin, S. Pujol, C. Bauer, D. Jennings, F. Fennessy, M. Sonka, J. Buatti, S. Aylward, J. V. Miller, S. Pieper, and R. Kikinis, "3D Slicer as an Image Computing Platform for the Quantitative Imaging Network," *Magnetic Resonance Imaging*, vol. 30, no. 9, pp. 1323–1341, nov 2012.

[71] E. R. Dougherty and R. A. Lotufo, *Hands-on morphological image processing*. SPIE press, 2003, vol. 59.

[72] M. N. Favorskaya, L. C. Jain *et al.*, *Computer Vision in Control Systems-1*. Springer, 2015.

[73] "File:Dylatacja przyklad.png - Wikimedia Commons." [Online]. Available: https://commons.wikimedia.org/wiki/File:Dylatacja_przyklad.png (Accessed 2017-05-12).

[74] "File:Erozja przyklad.png - Wikimedia Commons." [Online]. Available: https://commons.wikimedia.org/wiki/File:Erozja_przyklad2.png (Accessed 2017-05-12).

[75] "File:Two-pass connected component labeling.png - Wikimedia Commons." [Online]. Available: https://commons.wikimedia.org/wiki/File:Two-pass_connected_component_labeling.png (Accessed 2017-05-12).

[76] M. Kass, A. Witkin, and D. Terzopoulos, "Snakes: Active contour models," *International Journal of Computer Vision*, vol. 1, no. 4, pp. 321–331, 1988.

[77] H. Nakano, K. Mishima, Y. Ueda, A. Matsushita, H. Suga, Y. Miyawaki, T. Mano, Y. Mori, and Y. Ueyama, "A new method for determining the optimal ct threshold for extracting the upper airway," *Dentomaxillofacial Radiology*, vol. 42, no. 3, pp. 2639–7438, 2013, pMID: 22842640.

[78] W. Narkbuakaew, H. Nagahashi, K. Aoki, and Y. Kubota, "Bone segmentation in ct-liver images using k-means clustering for 3d rib cage surface-modeling," *WSEAS Transactions on Biology and Biomedicine*, vol. 11, pp. 183–193, 2014.

[79] M. Y. Mashor, "Improving the performance of k-means clustering algorithm to position the centers of rbf network," *International Journal of the Computer, The Internet and Management*, vol. 6, no. 2, pp. 121–124, 1998.

[80] D. Arthur and S. Vassilvitskii, "k-means++: The advantages of careful seeding," in *Proceedings of the eighteenth annual ACM-SIAM symposium on Discrete algorithms*. Society for Industrial and Applied Mathematics, 2007, pp. 1027–1035.

[81] P. J. Rousseeuw, "Silhouettes: a graphical aid to the interpretation and validation of cluster analysis," *Journal of Computational and Applied Mathematics*, vol. 20, pp. 53–65, 1987.

[82] N. J. Tustison and J. Gee, "N4itk: Nick's n3 itk implementation for mri bias field correction," *Insight Journal*, Dec. 2010.

[83] K. Held, E. R. Kops, B. J. Krause, W. M. Wells, R. Kikinis, and H.-W. Muller-Gartner, "Markov random field segmentation of brain mr images," *IEEE Transactions on Medical Imaging*, vol. 16, no. 6, pp. 878–886, 1997.

[84] K. Ohtakara, S. Hayashi, H. Tanaka, and H. Hoshi, "Consideration of optimal isodose surface selection for target coverage in micro-multileaf collimator-based stereotactic radiotherapy for large cystic brain metastases: comparison of 90%, 80% and 70% isodose surface-based planning," *The British Journal of Radiology*, vol. 85, no. 1017, pp. e640–e646, 2012, pMID: 22422384.

[85] J. L. Robar and C. Thomas, "Hybridarc: a novel radiation therapy technique combining optimized dynamic arcs and intensity modulation," *Medical Dosimetry*, vol. 37, no. 4, pp. 358–368, 2013.

[86] M. Rao, W. Yang, F. Chen, K. Sheng, J. Ye, V. Mehta, D. Shepard, and D. Cao, "Comparison of elekta vmat with helical tomotherapy and fixed field imrt: plan quality, delivery efficiency and accuracy," *Medical Physics*, vol. 37, no. 3, pp. 1350–1359, 2010.

[87] "Accelerated IMRT and VMAT planning," *Philips White Paper*, pp. 1–4, 2014. [Online]. Available: http://incenter.medical.philips.com/doclib/enc/fetch/2000/4504/577242/577243/577244/582095/582189/Pinnacle3_AutoPlanning_Overview.pdf%3fnodeid%3d10689140%26vernum%3d-2 (Accessed 2017-05-12).

[88] K. Bzdusek, H. Friberger, K. Eriksson, B. Hårdemark, D. Robinson, and M. Kaus, "Development and evaluation of an efficient approach to volumetric arc therapy planning," *Medical Physics*, vol. 36, no. 6, pp. 2328–2339, 2009.

[89] J. C. Marsh, G. E. Ziel, A. Z. Diaz, J. A. Wendt, R. Gobole, and J. V. Turian, "Integral dose delivered to normal brain with conventional intensity-modulated radiotherapy (imrt) and helical tomotherapy imrt during partial brain radiotherapy for high-grade gliomas with and without selective sparing of the hippocampus, limbic circuit and neural stem cell compartment," *Journal of Medical Imaging and Radiation Oncology*, vol. 57, no. 3, pp. 378–383, 2013.

[90] M. Farzin, M. Molls, S. Astner, I.-C. Rondak, and M. Oechsner, "Simultaneous integrated vs. sequential boost in vmat radiotherapy of high-grade gliomas," *Strahlentherapie und Onkologie*, vol. 191, no. 12, pp. 945–952, 2015.

[91] T. McNutt, "Dose calculations: collapsed cone convolution superposition and delta pixel beam," *Philips White Paper*, no. 4535, p. 983, 2002.

[92] M. Wendling, L. J. Zijp, L. N. McDermott, E. J. Smit, J.-J. Sonke, B. J. Mijnheer, and M. van Herk, "A fast algorithm for gamma evaluation in 3d," *Medical Physics*, vol. 34, no. 5, pp. 1647–1654, 2007.

[93] M. Janaszewski, M. Couprie, and L. Babout, "Hole filling in 3d volumetric objects," *Pattern Recognition*, vol. 43, no. 10, pp. 3548–3559, 2010.

[94] L. D. Cohen, "On active contour models and balloons," *CVGIP: Image Understanding*, vol. 53, no. 2, pp. 211–218, 1991.

[95] J. Sachdeva, V. Kumar, I. Gupta, N. Khandelwal, and C. K. Ahuja, "A novel content-based active contour model for brain tumor segmentation," *Magnetic Resonance Imaging*, vol. 30, no. 5, pp. 694–715, 2012.

[96] X. Qian, J. Wang, S. Guo, and Q. Li, "An active contour model for medical image segmentation with application to brain ct image," *Medical Physics*, vol. 40, no. 2, 2013, 021911.

[97] N. L. Bui, S. H. Ong, and K. W. C. Foong, "Automatic segmentation of the nasal cavity and paranasal sinuses from cone-beam ct images," *International Journal of Computer Assisted Radiology and Surgery*, vol. 10, no. 8, pp. 1269–1277, 2015.

[98] R. Widita and O. Ivansyah, "Image Segmentation Of CT Head Image To Define Tumour Using K-Means Clustering Algorithm," *IOSR Journal of Applied Physics*, vol. 8, no. 2, pp. 29–31, 2016. [Online]. Available: http://www.iosrjournals.org/iosr-jap/papers/Vol8-issue2/Version-1/F0802012931.pdf (Accessed 2017-05-26).

[99] M. van Eijnatten, J. Koivisto, K. Karhu, T. Forouzanfar, and J. Wolff, "The impact of manual threshold selection in medical additive manufacturing," *International Journal of Computer Assisted Radiology and Surgery*, pp. 1–9, 2016.

[100] A. Nejati, N. Kabaliuk, M. C. Jermy, and J. E. Cater, "A deformable template method for describing and averaging the anatomical variation of the human nasal cavity," *BMC Medical Imaging*, vol. 16, no. 1, p. 55, 2016.

[101] Z. Kato and T.-C. Pong, *A Markov Random Field Image Segmentation Model Using Combined Color and Texture Features*. Berlin, Heidelberg: Springer Berlin Heidelberg, 2001, pp. 547–554.

[102] J. H. Jonsson, M. G. Karlsson, M. Karlsson, and T. Nyholm, "Treatment planning using mri data: an analysis of the dose calculation accuracy for different treatment regions," *Radiation Oncology*, vol. 5, no. 1, p. 62, 2010.

[103] J. Korhonen, M. Kapanen, J. Keyriläinen, T. Seppälä, and M. Tenhunen, "A dual model hu conversion from mri intensity values within and outside of bone segment for mri-based radiotherapy treatment planning of prostate cancer," *Medical Physics*, vol. 41, no. 1, 2014, 011704.

[104] I. C. on Radiation Units and Measurements, *Photon, Electron, Proton, and Neutron Interaction Data for Body Tissues*, ser. American Fisheries Society Symposium. International Commission on Radiation Units and Measurements, 1992.